Atlas of Formability

Nickelvac K-500

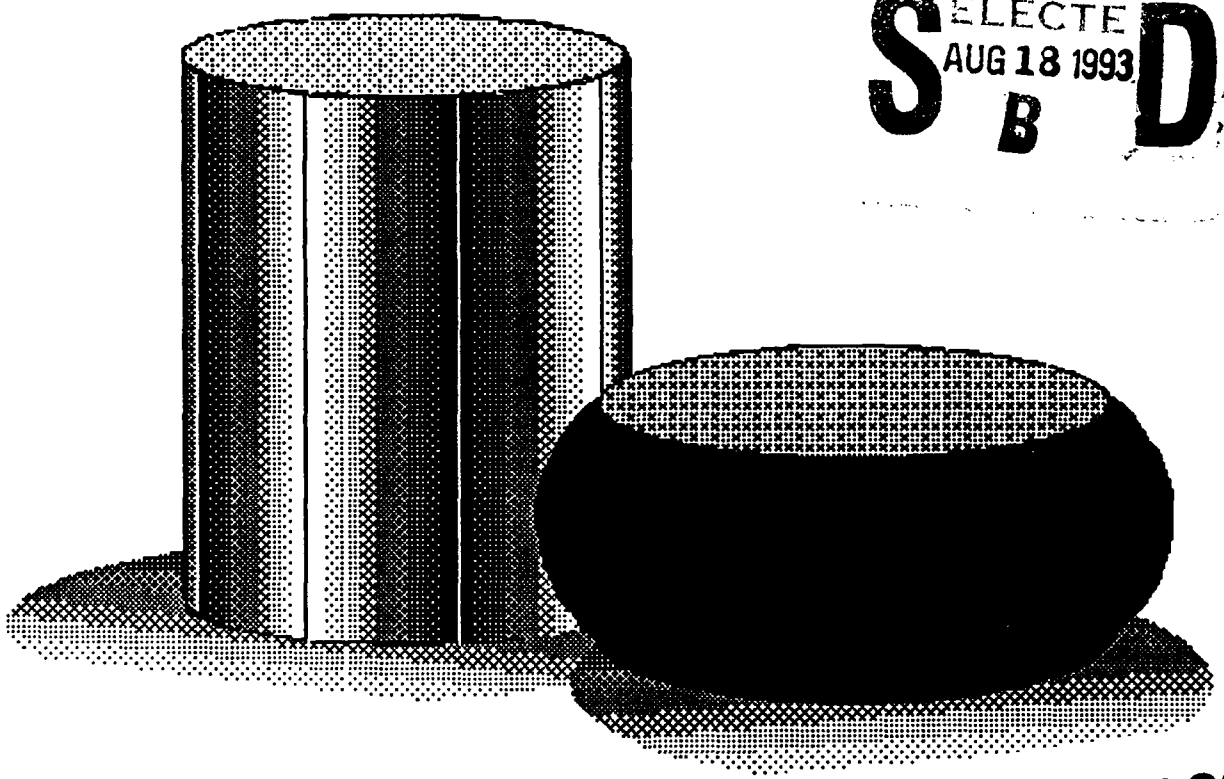

NCEMT

DISCLAIMER NOTICE

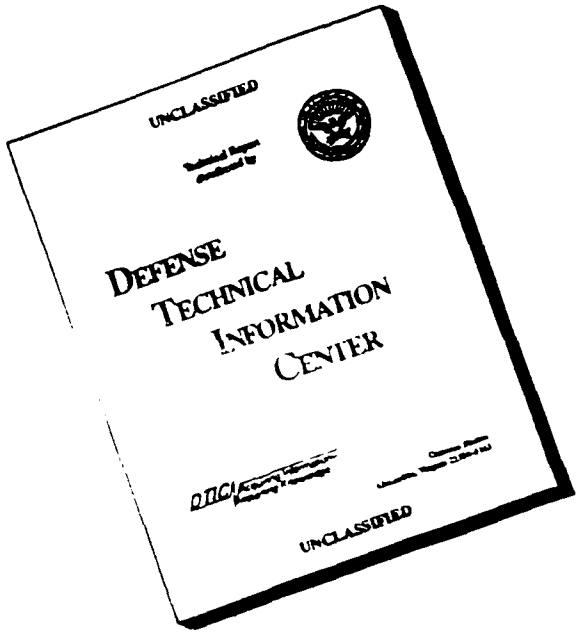

THIS DOCUMENT IS BEST QUALITY AVAILABLE. THE COPY FURNISHED TO DTIC CONTAINED A SIGNIFICANT NUMBER OF PAGES WHICH DO NOT REPRODUCE LEGIBLY.

REPORT DOCUMENTATION PAGE

Form Approved
OMB No. 0704-0188

1. AGENCY USE ONLY (Leave blank)	2. REPORT DATE	3. REPORT TYPE AND DATES COVERED
	October 31, 1992	Final, July 31, 1992-October 31, 1992

4. TITLE AND SUBTITLE

Atlas of Formability
Nickelvac K-500

5. FUNDING NUMBERS

C-N00140-88-C-RC21

6. AUTHOR(S)

Prabir Chaudhury
Dan Zhao

7. PERFORMING ORGANIZATION NAME(S) AND ADDRESS(ES)

National Center for Excellence in Metalworking Technology (NCEMT)
1450 Scalp Avenue
Johnstown, PA 15904

8. PERFORMING ORGANIZATION REPORT NUMBER

9. SPONSORING/MONITORING AGENCY NAME(S) AND ADDRESS(ES)

Naval Industrial Resources Support Activity
Building 75-2, Naval Base
Philadelphia, PA 19112-5078

10. SPONSORING/MONITORING AGENCY REPORT NUMBER

11. SUPPLEMENTARY NOTES

12a. DISTRIBUTION/AVAILABILITY STATEMENT

12b. DISTRIBUTION CODE

13. ABSTRACT *(Maximum 200 words)*

In this investigation, flow behavior of Nickelvac K-500 alloy was studied by conducting compression tests over a wide range of temperatures and strain rates. Constitutive relations were determined from the flow behavior, and dynamic material modeling was conducted on this alloy. Thus, the optimum processing condition in terms of temperature and strain rate was identified. Microstructural changes during high temperature deformation were also characterized.

14. SUBJECT TERMS

Nickelvac K-500, Deformation Processing, High Temperature Deformation, Procssing Map, Metalworking

15. NUMBER OF PAGES

78

16. PRICE CODE

17. SECURITY CLASSIFICATION OF REPORT	18. SECURITY CLASSIFICATION OF THIS PAGE	19. SECURITY CLASSIFICATION OF ABSTRACT	20. LIMITATION OF ABSTRACT
Unclassified	Unclassified	Unclassified	

ATLAS OF FORMABILITY

NICKELVAC K-500

by

Prabir K. Chaudhury and Dan Zhao

National Center for Excellence in Metalworking Technology
1450 Scalp Avenue
Johnstown, PA 15904

for

Naval Industrial Resource Support Activity
Building 75-2, Naval Base
Philadelphia, PA 19112-5078

October 31, 1992

TABLE OF CONTENTS

LIST OF TABLE

Nickelvac K-500

Introduction

K-500 alloy has an excellent combination of high strength, ductility and corrosion resistance. The alloy exceeds nickel in resistance to sulfuric and hydrofluoric acids, and brine. Handling of waters, including sea water and brackish water, is a major area of application. The understanding of mechanical and microstructural behavior during high temperature deformation is very important for the forming processes of this alloy. In this investigation, flow behavior of Nickelvac K-500 was studied by conducting compression tests at various temperatures and strain rates. Constitutive relations were determined from the flow behavior and then, a dynamic material modeling for this alloy was performed. Thus, the optimum processing conditions in terms of temperature and strain rate were determined. Microstructural changes during high temperature deformation were also characterized to aid process design engineers to select processing conditions in terms of resulting microstructure.

Experimental Procedure

The material used in this investigation was commercially available Nickelvac K-500 heat treated and aged wrought bars. The typical microstructure of the as-received materials had equiaxed grains with a uniform grain size of approximately 11 μm (10ASTM). The microstructure presented extensive twinning and, intragranular precipitates. which are presumably titanium carbides and complex carbonitrides. Figure 1 shows the typical microstructure of the as received material. The chemical composition is as follows:

C	S	Mn	Si	Co	Ti	Al	Fe	Cu	Ni	P
0.142	0.0002	0.76	0.11	0.01	0.54	3.05	0.82	30.27	64.76	0.011

Cylindrical compression test specimens with a diameter of 12.7 mm and a height of 15.9 mm were machined from the bars. Isothermal compression testing was conducted on an MTS testing machine. The test matrix was as follows:

Temperature, C (F): 800 (1472), 900 (1652), 950 (1742), 1000 (1832), 1050 (1922), 1100 (2012), 1150 (2102), and 1200 (2192);
Strain rate, s^{-1}: 0.001, 0.01, 0.05, 0.1, 0.5, 1, 5 and 20.

The tests were conducted in vacuum. Load and stroke data from the tests were acquired by a computer and later converted to true stress-true strain curves. Immediately after the compression test, the specimens were quenched with forced helium gas in order to retain the deformed microstructure. Longitudinal and transverse sections of the specimens were examined by optical microscopy. The photomicrographs presented were taken from the center of the longitudinal section of the specimens.

Results

Table 1 shows a list of the figures, test conditions and the observed microstructures. The true stress-true strain flow curves with selective corresponding deformed microstructure are shown in Figure 2 to Figure 65. True stress versus strain rate was plotted in log-log scale in Figure 66 at a true strain of 0.3. The slope of the plot gives the strain rate sensitivity m, which is not constant over the range of strain rate tested. Log stress vs. 1/T at the same true strain is shown in Figure 67. A processing map at this strain was developed and is shown in Figure 68. The optimum processing condition from the map is 1125 C and 10^{-3} s^{-1} for this material.

Table 1. List of figures, testing conditions and microstructural observations for Nickelvac K-500

Figure No	Temperature C (F)	Strain Rate s^{-1}	Microstructure Optical Microscopy	Page No
1	As received		Equiaxed grains with a uniform grain size of approximately 11.0 μm (10ASTM). The structure presents extensive twinning and, there are intragranular precipitates.	4
2	800 (1472)	0.001	Recrystallized equiaxed grains (100%) with a uniform size (4.8μm). Some twinning and fine intragranular precipitation.	5
3	800 (1472)	0.01		6
4	800 (1472)	0.05	Equiaxed recrystallized grains (100%) with a uniform size (~5 μm) some twinning and fine intragranular precipitates.	7
5	800 (1472)	0.1	Same as above	8
6	800 (1472)	0.5		9
7	800 (1472)	1	Same as above, but there is an extensive twinning	10
8	800 (1472)	5		11
9	800 (1472)	20	100 % recrystallized grains with a uniform size of approximately 5μm, extensive twinning and fine intragranular precipitation.	12
10	900 (1652)	0.001		13
11	900 (1652)	0.01	100% recrystallized structure, the equiaxed grains have a duplex size. The grain size is 9.3μm and 27.2μm for the small and the large grains respectively. There is also an intragranular precipitation	14
12	900 (1652)	0.05		15
13	900 (1652)	0.1	Recrystallized equiaxed grains with a duplex size. ~40% of large grains (~17.2μm). Intragranular precipitation is also present.	16
14	900 (1652)	0.5		17
15	900 (1652)	1	Same as above, but the proportion of larger grains (<17μm) is bellow 30%.	18
16	900	5		19
17	900 (1652)	20	Equiaxed recrystallized grains with small grain size (~5.2μm) and ~5% of larger grains (~15.7μm) .	20
18	950 (1742)	0.001	Equiaxed grains with a duplex size. The large and small grains have a size of 32.5 μm and 9.1 μm respectively. The larger grains show the presence of a substructure. There is twinning and intragranular precipitation.	21
19	950 (1742)	0.01		22
20	950 (1742)	0.05	Twinned equiaxed recrystallized grains. ~5% of the grains are larger than average. The intragranular precipitation is still present.	23
21	950 (1742)	0.1		24
22	950 (1742)	0.5		25

23	950 (1742)	1	Recrystallized equiaxed grains with a duplex size. The large and small grains have a size of 19 and 6.9 μm respectively. These show twins and intragranular precipitation.	26
24	950 (1742)	5		27
25	950 (1742)	20	Recrystallized equiaxed grains with very large proportion of small grains (95%) with an average size of 8.6μm, fewer grains are large (~21.7μm). Twinning and intragranular precipitation are present.	28
26	1000 (1882)	0.001		29
27	1000 (1882)	0.01	Large equiaxed grains with a uniform size, (57μm). Extensive twinning and the intragranular precipitation is decreasing, but the particulates are coarsening.	30
28	1000 (1882)	0.05		31
29	1000 (1882)	0.1	Large equiaxed grains with a relatively uniform grain size, extensive twinning and some intragranular corse precipitates.	32
30	1000 (1882)	0.5		33
31	1000 (1882)	1	Same as above, but smaller grain size (25.5μm).	34
32	1000 (1882)	5		35
33	1000 (1882)	20	Same as above, but the grain size is decreasing, (16.3μm).	36
34	1050 (1922)	0.001	Equiaxed grains with an extensive irregular grain growth . the average grain size is ~65.4μm. The larger grains present a substructure and the intragranular precipitates have suffered coarsening.	37
35	1050 (1922)	0.01		38
36	1050 (1922)	0.05	Large equiaxed grains with twins. They are irregular in size with approximately 10% of larger grains than average.	39
37	1050 (1922)	0.1	100% recrystallized equiaxed grains with a uniform size (~42.6μm). An intragranular precipitation is observed.	40
38	1050 (1922)	0.5		41
39	1050 (1922)	1	Equiaxed recrystallized grains with a uniform size. some twinning and intragranular precipitates are present.	42
40	1050 (1922)	5		43
41	1050 (1922)	20	100% recrystallized equiaxed grains with a uniform size (~21.6μm). A coarse intragranular precipitation is observed.	44
42	1100 (1212)	0.001		45
43	1100 (1212)	0.01	Equiaxed recrystallized grains with an extensive grain growth (>55μm). The larger grains show the presence of a substructure. There is an extensive twining and coarsening of the intragranular precipitates.	46
44	1100 (1212)	0.05		47

45	1100 (1212)	0.1	Equiaxed 100% recrystallized grains with an extensive twinning. A small proportion (<5%) of larger than average grains is present, and a small fraction of coarsen precipitates is also present.	48
46	1100 (1212)	0.5		49
47	1100 (1212)	1	100% recrystallized equiaxed grains (27μm). The fraction of grains larger than the average is greatly reduced (<1%).	50
48	1100 (1212)	5		51
49	1100 (1212)	20	100% recrystallized grains with a uniform size (23μm), extensive twinning and, still the presence of intragranular precipitation.	52
50	1150 (2102)	0.001	Extensive grain growth, equiaxed grains with an average size of 181.4μm. The larger than average grains show a substructure and the intragranular precipitates are becoming finer (dissolution).	53
51	1150 (2102)	0.01		54
52	1150 (2102)	0.05	100% of large equiaxed grains with a uniform size. Twinning is present and fine intragranular precipitation	55
53	1150 (2102)	0.1	100% of large equiaxed grains with a uniform size (~61.2μm) Twinning is present and fine intragranular precipitation	56
54	1150 (2102)	0.5	Same as above, but a smaller grain size	57
55	1150 (2102)	1	Same as above, but a smaller grain size and extensive twinning.	58
56	1150 (2102)	5		59
57	1150 (2102)	20	100% equiaxed grain with a uniform size (~52.5μm). Twinning and a small proportion of fine precipitates is present.	60
58	1200 (2192)	0.001		61
59	1200 (2192)	0.01	Excessively grown equiaxed grains with an average size >150μm. Twinning is present and the precipitates are practically dissolved.	62
60	1200 (2192)	0.05		63
61	1200 (2192)	0.1	Large equiaxed grains showing twins and a very small proportion of fine intragranular precipitates.	64
62	1200 (2192)	0.5		65
63	1200 (2192)	1	Recrystallized equiaxed grains with a size of ~61μm . Twinning and a very small fraction of fine intragranular precipitates are present.	66
64	1200 (2192)	5		67
65	1200 (2192)	20	100% recrystallized equiaxed grain with a uniform size of ~47μm, there a few twins and the intragranular precipitation is practically absent.	68

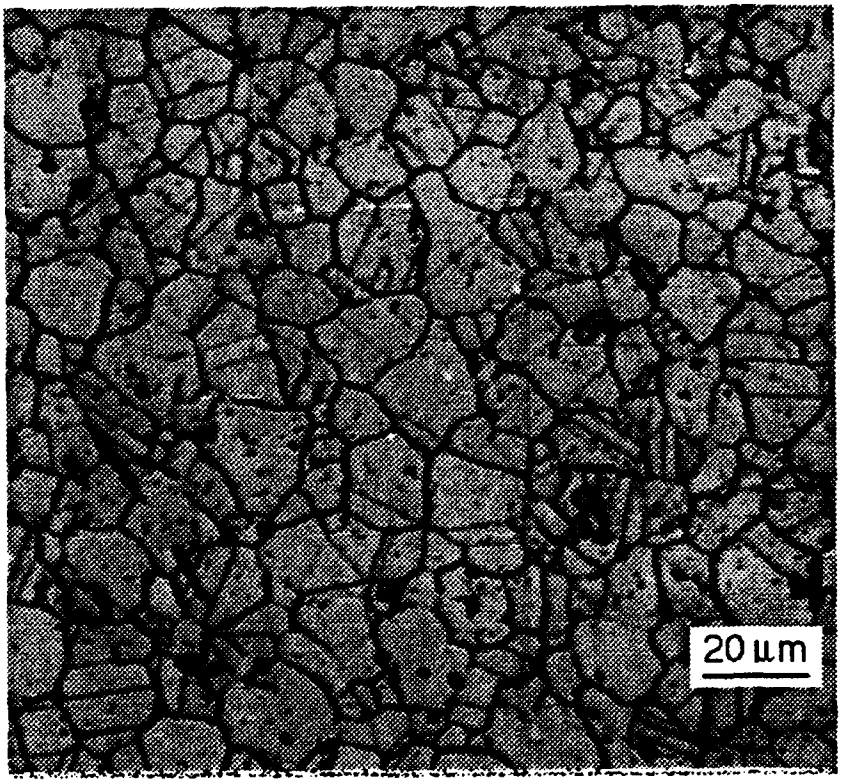

Figure 1. As-received microstructure of Nickelvac K-500.

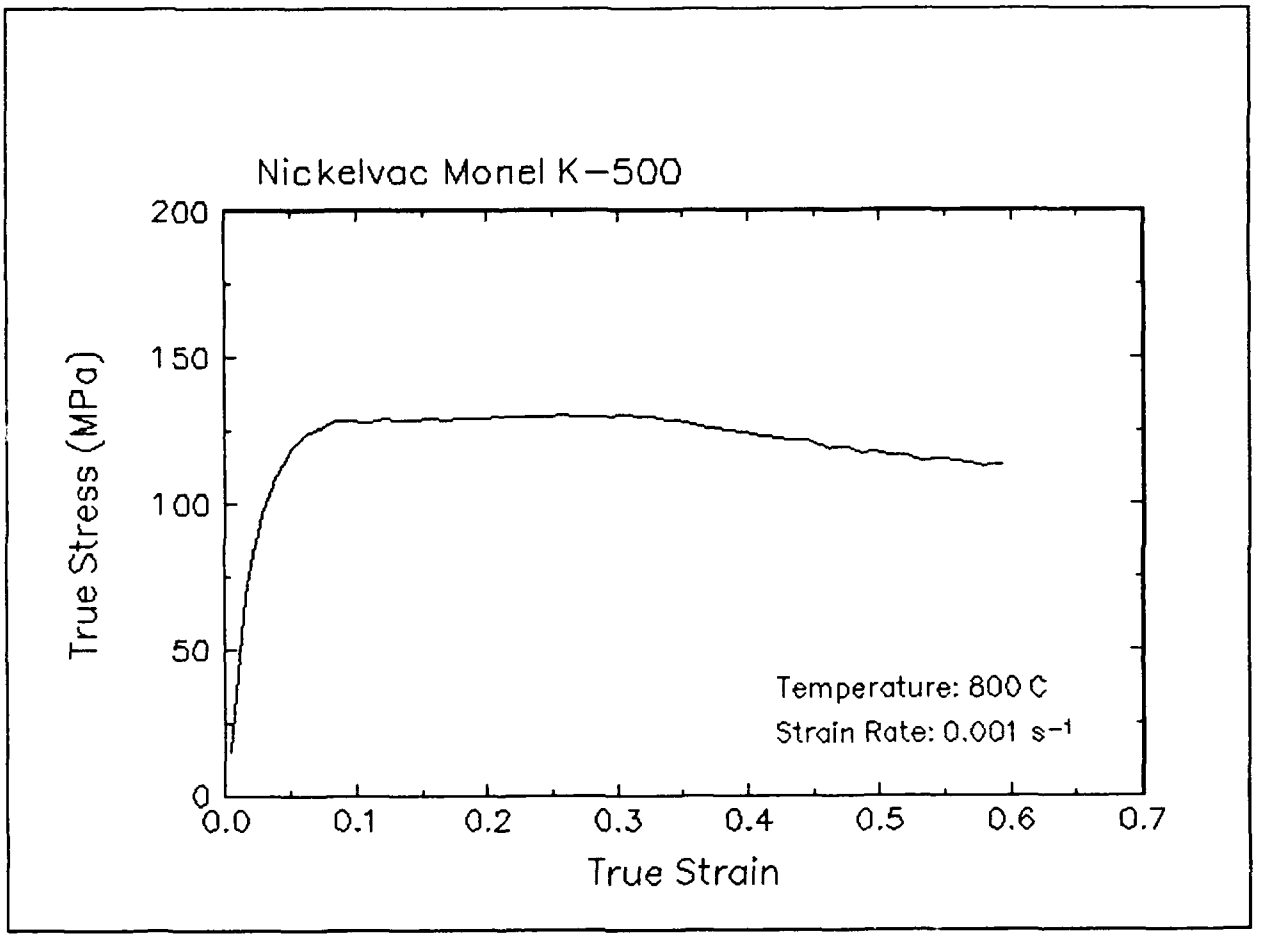

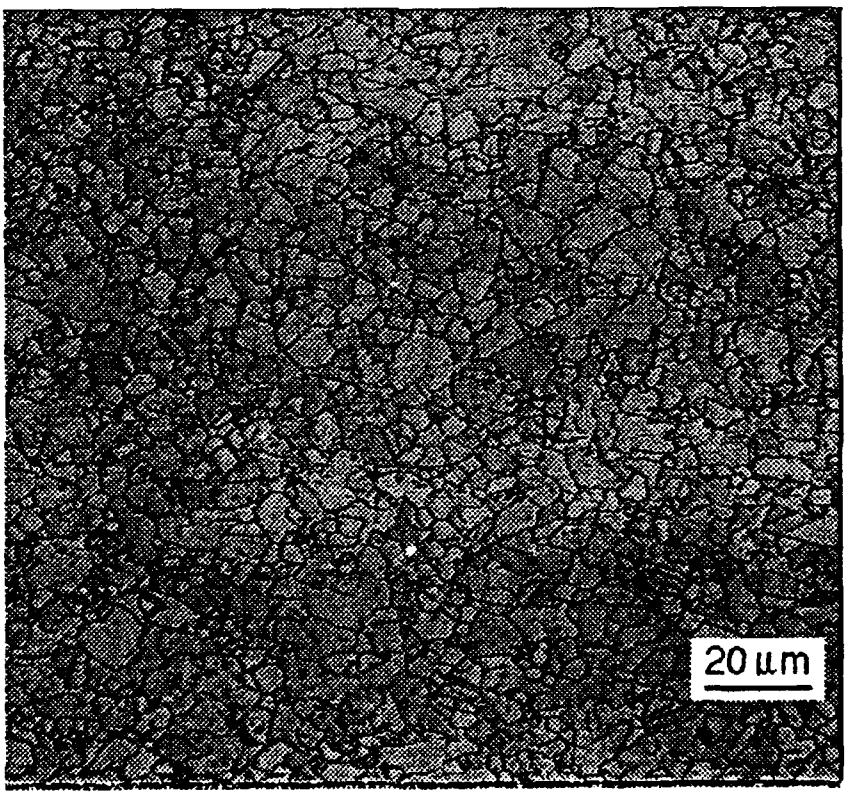

Figure 2. True stress-true strain curve and an optical micrograph from the center of the compressed sample cut through the compression axis, 800 C and 0.001 s^{-1}.

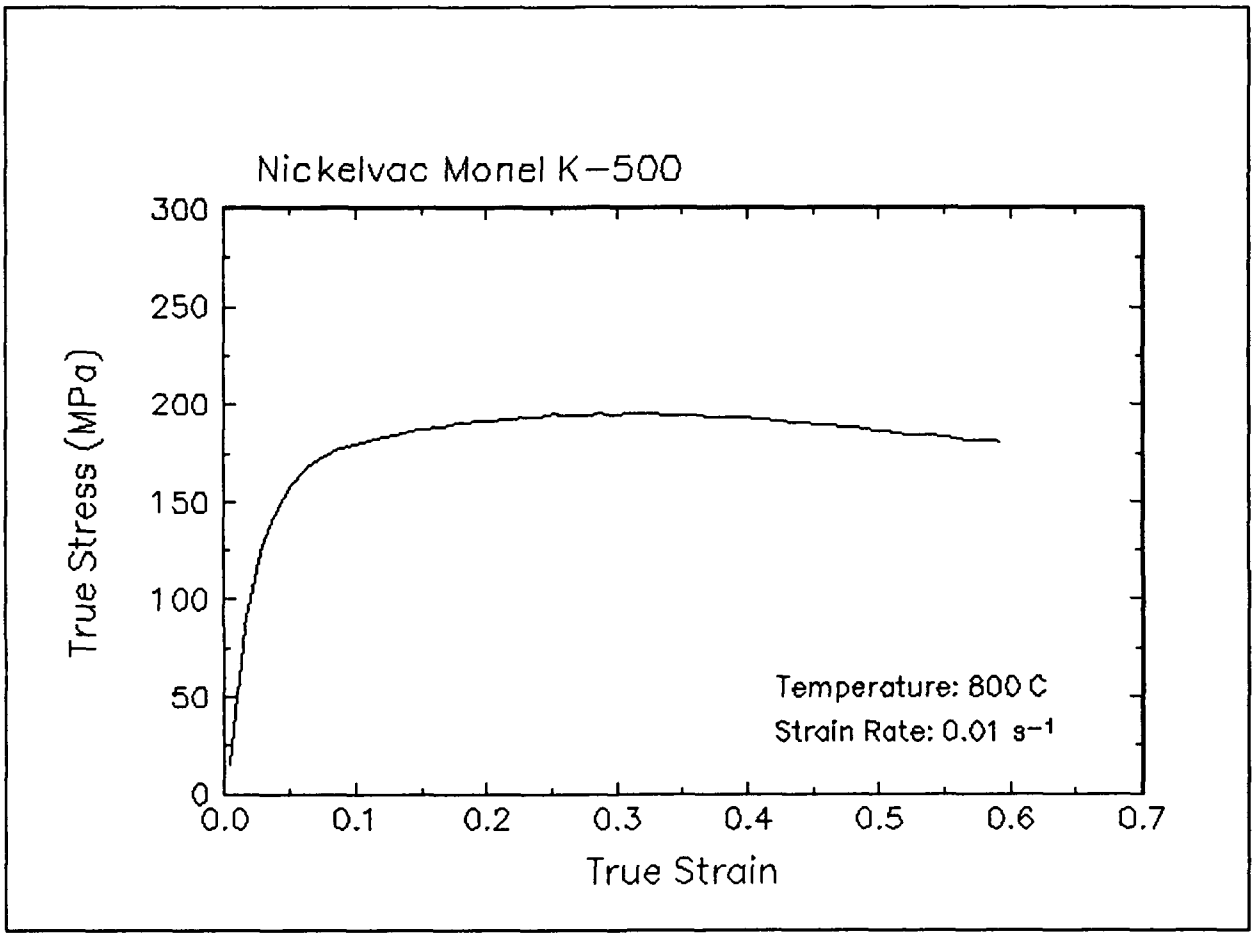

Figure 3. True stress-true strain curve, 800 C and 0.01 s^{-1}.

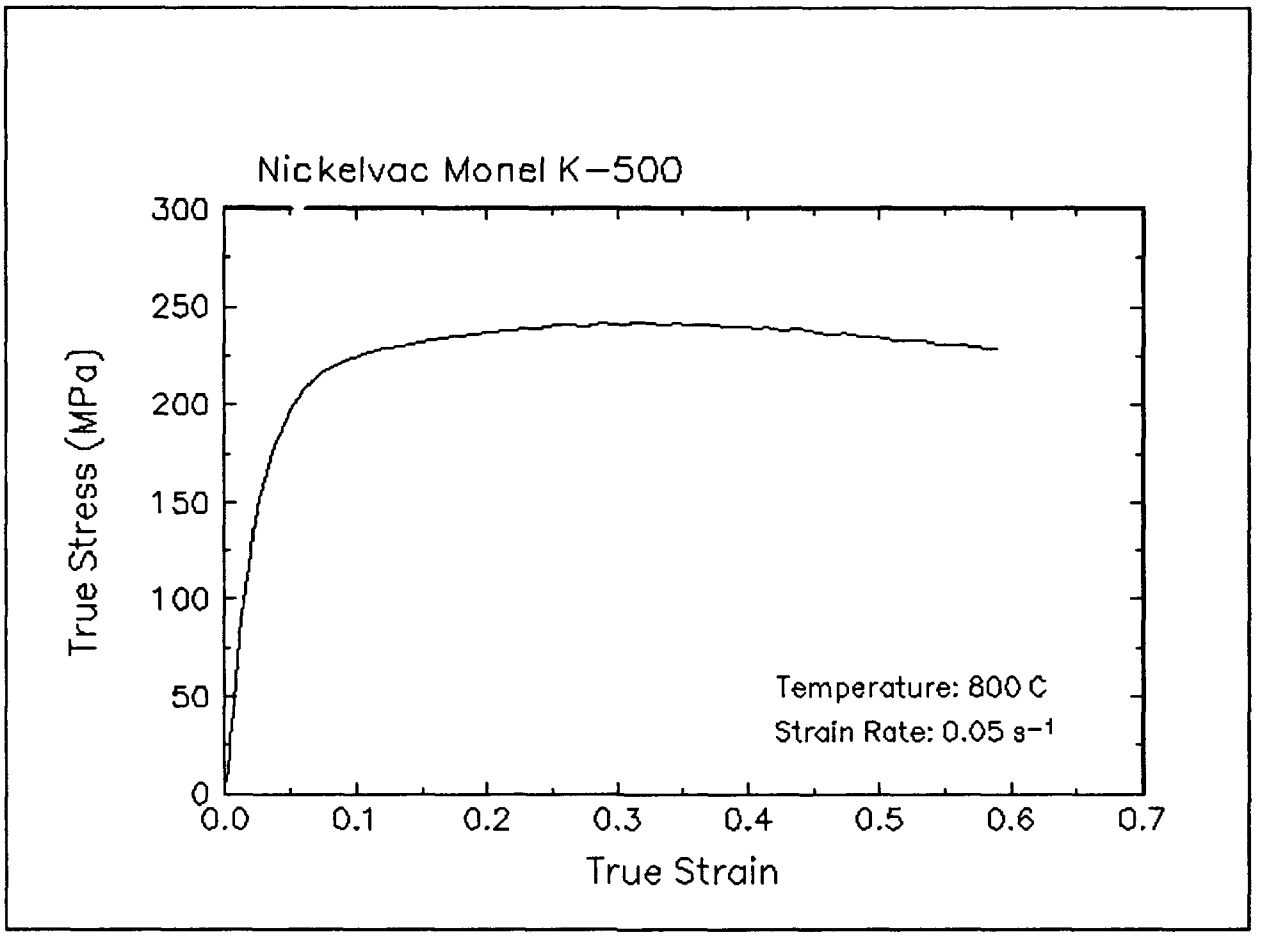

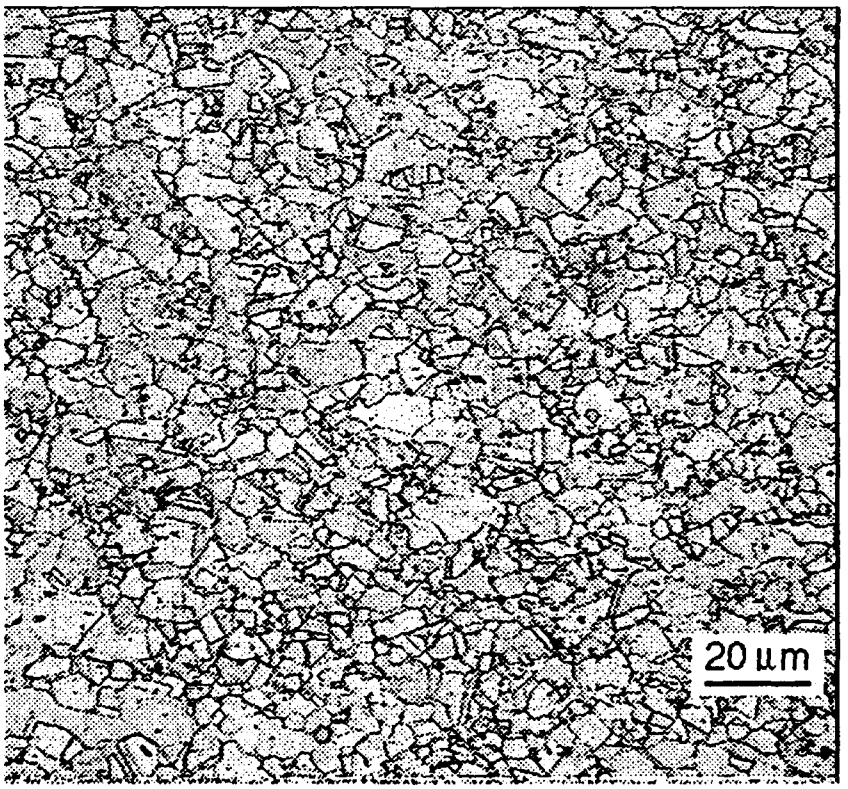

Figure 4. True stress-true strain curve and an optical micrograph from the center of the compressed sample cut through the compression axis, 800 C and 0.05 s^{-1}.

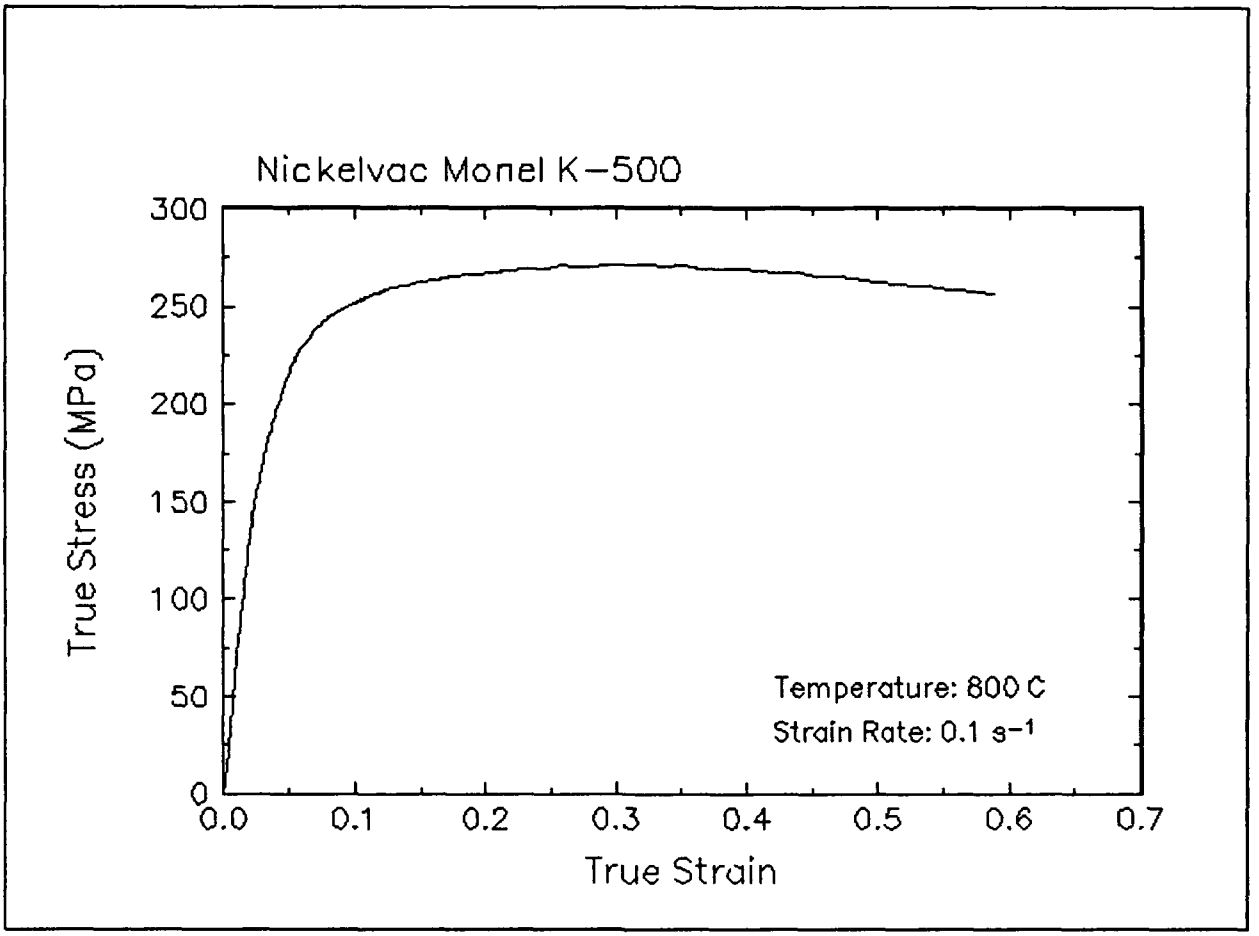

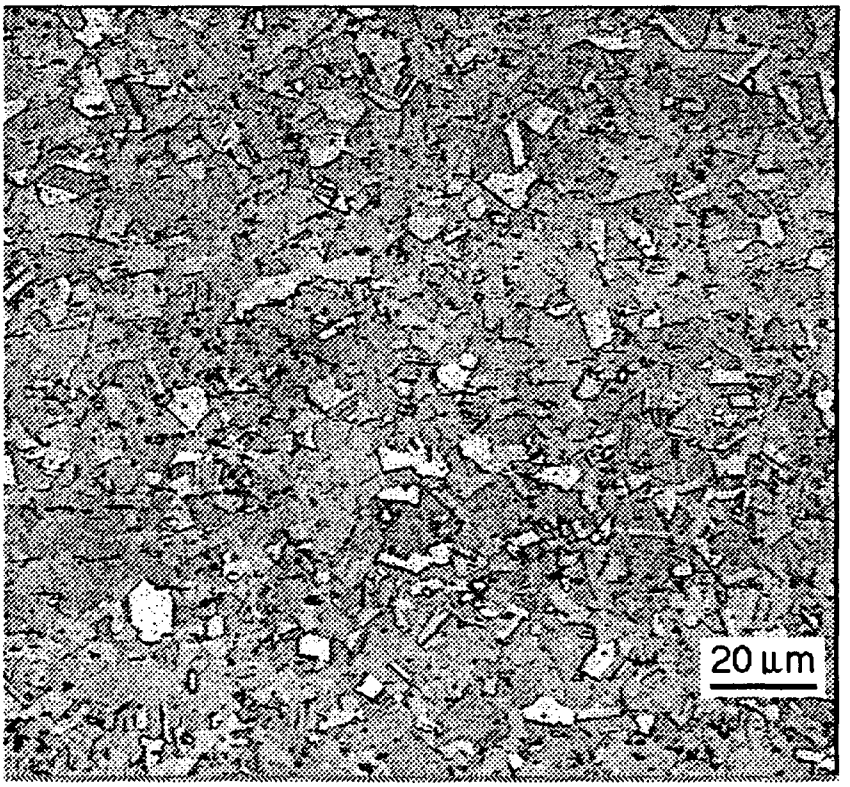

Figure 5. True stress-true strain curve and an optical micrograph from the center of the compressed sample cut through the compression axis, 800 C and 0.1 s^{-1}.

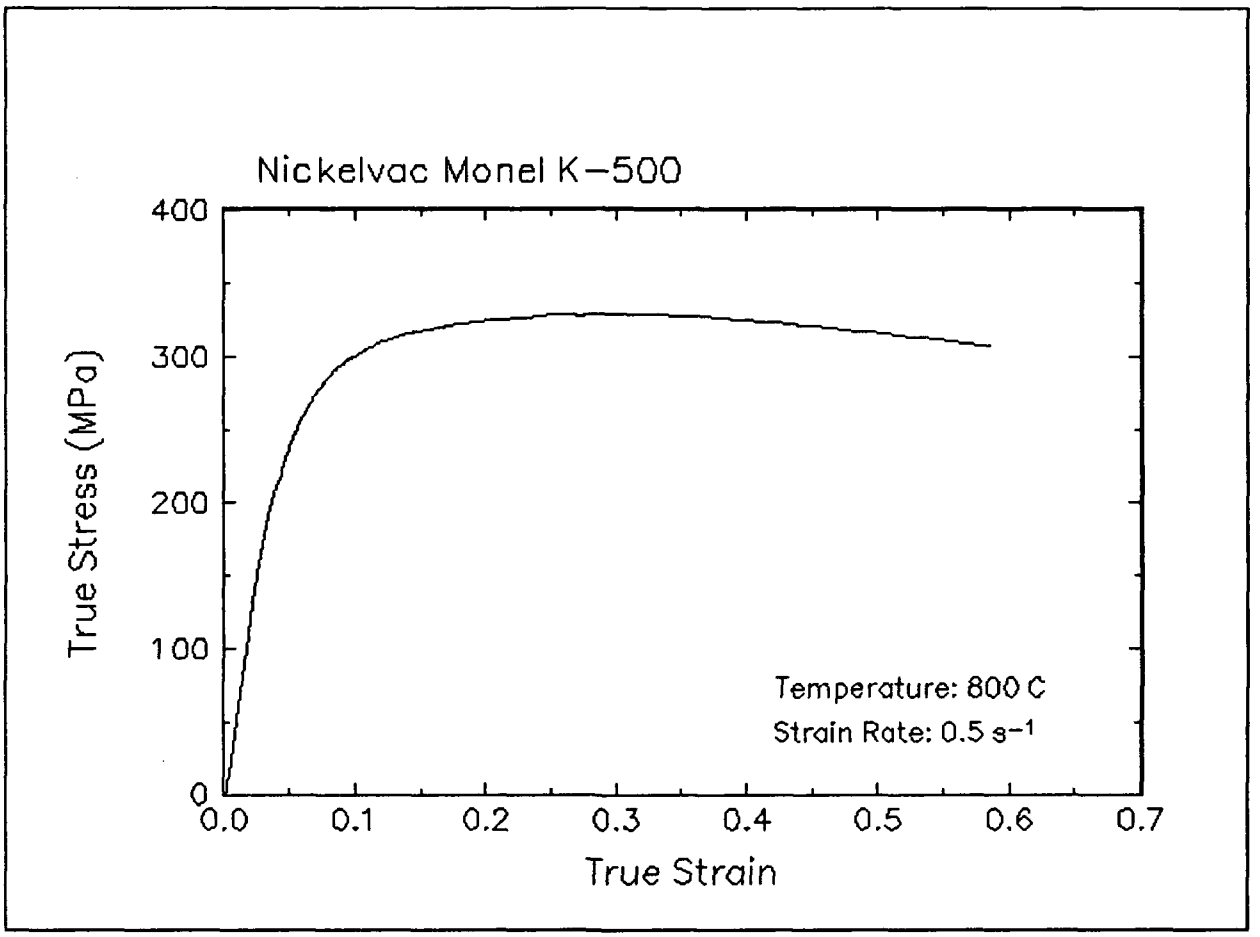

Figure 6. True stress-true strain curve, 800 C and 0.5 s^{-1}.

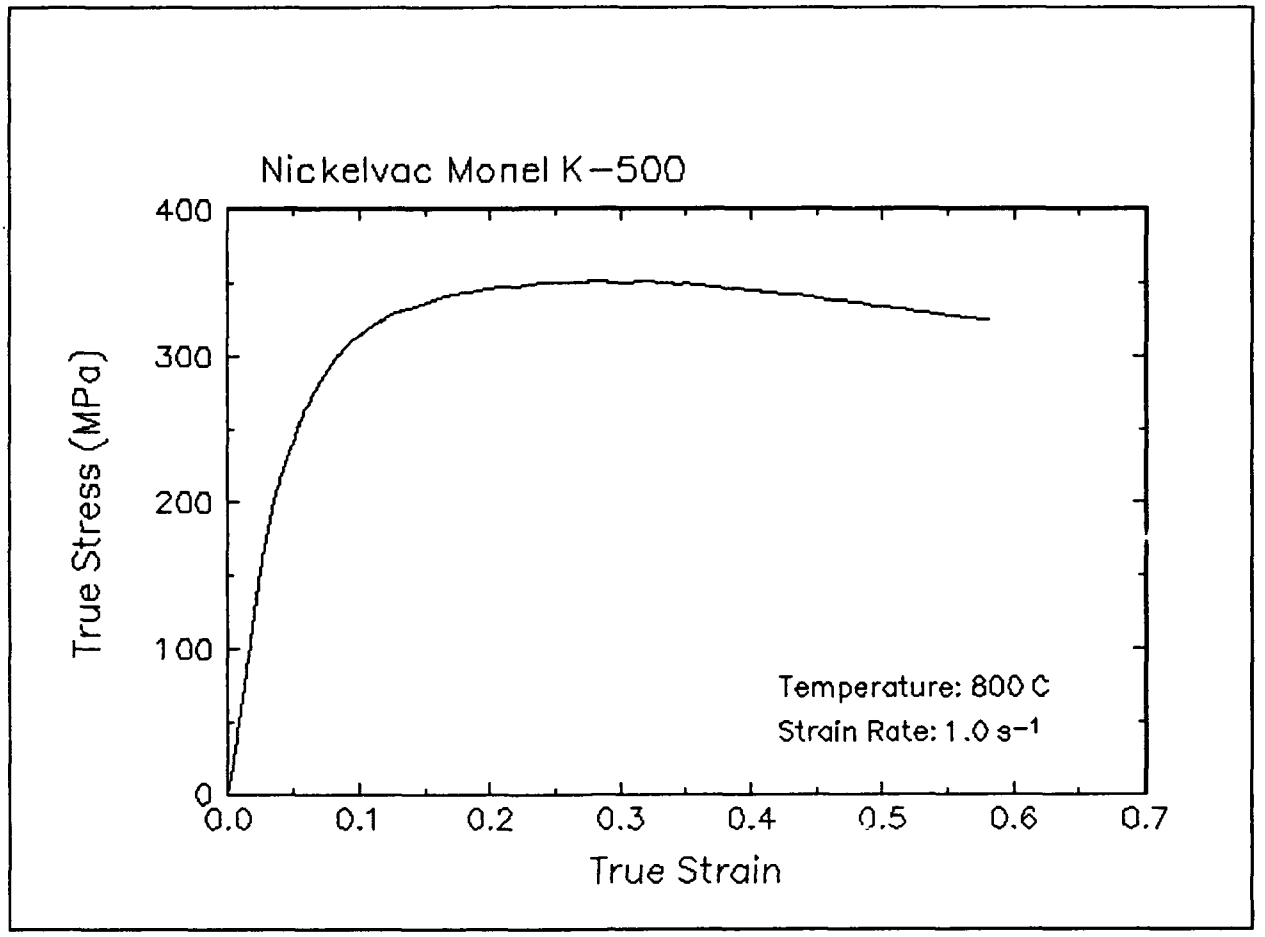

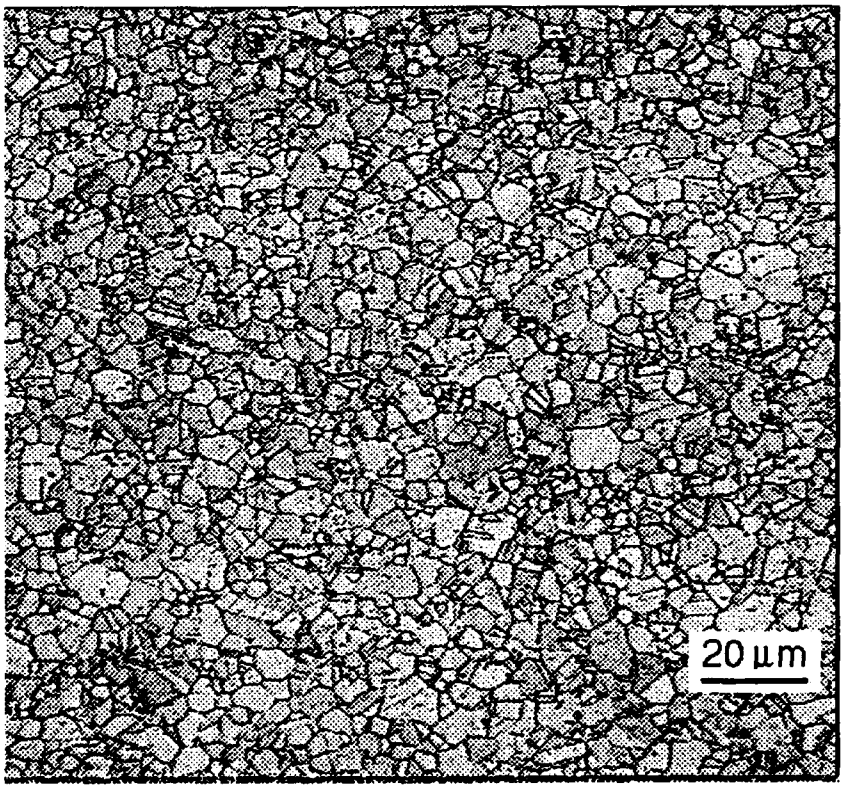

Figure 7. True stress-true strain curve and an optical micrograph from the center of the compressed sample cut through the compression axis, 800 C and 1 s^{-1}.

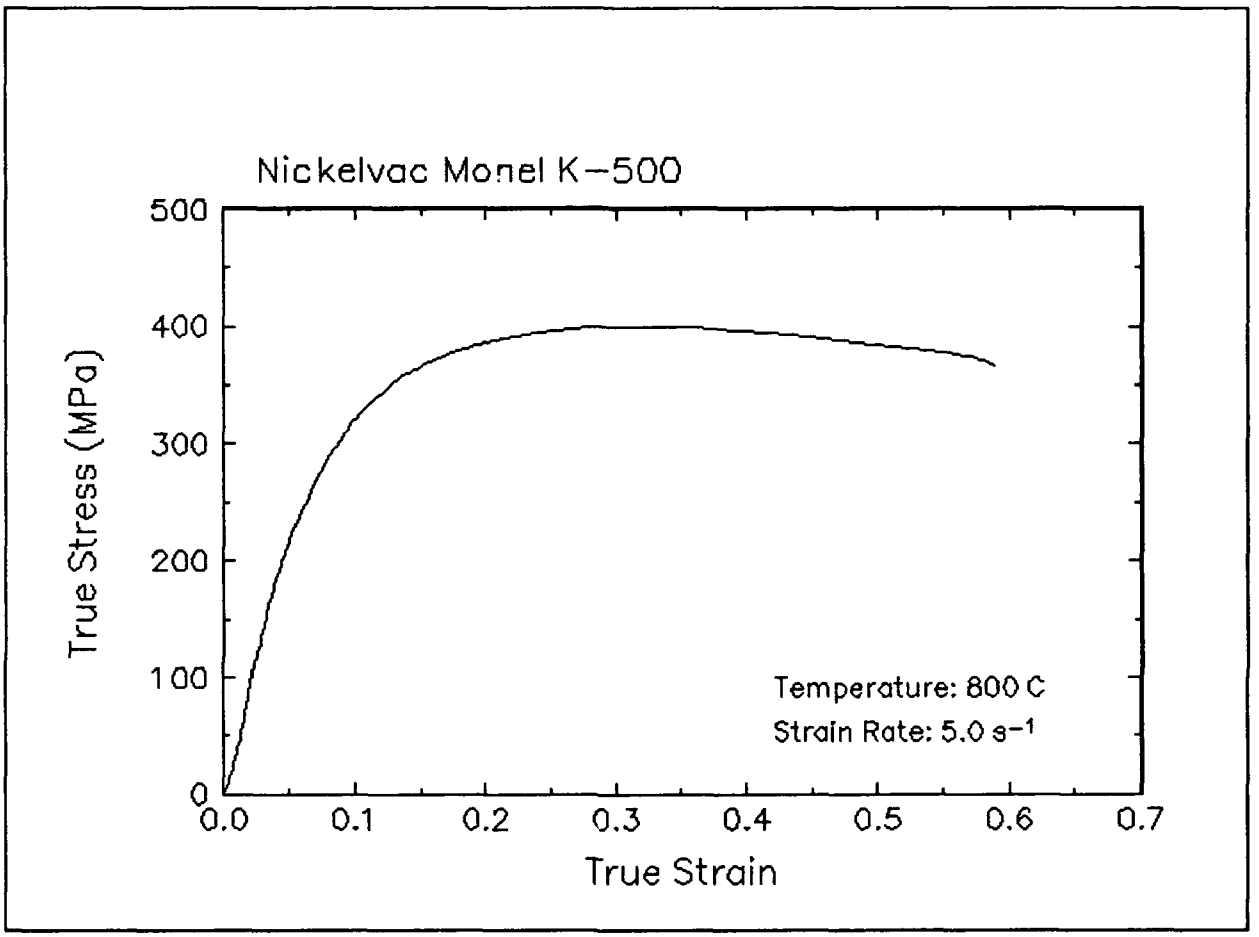

Figure 8. True stress-true strain curve, 800 C and 5 s^{-1}.

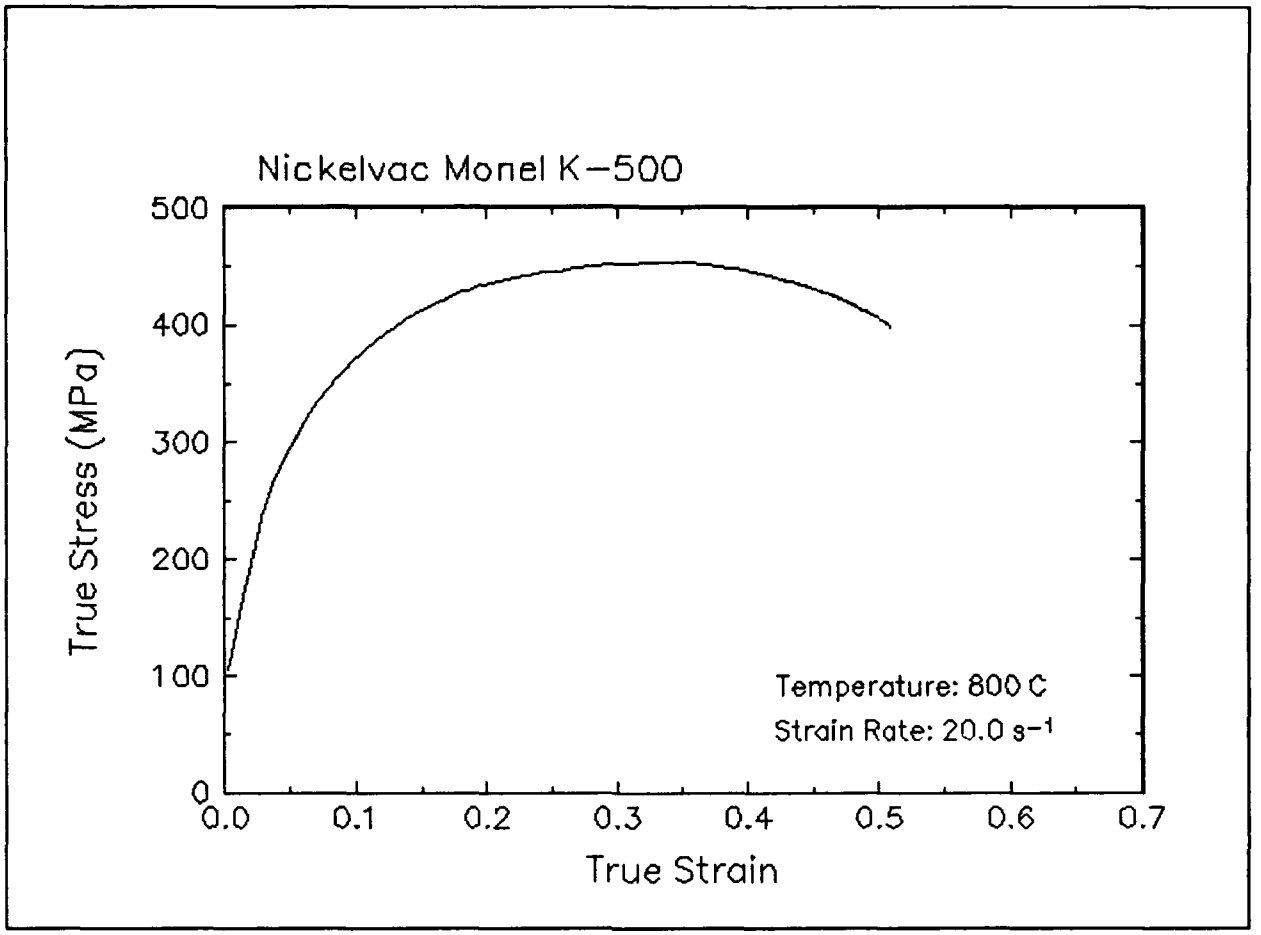

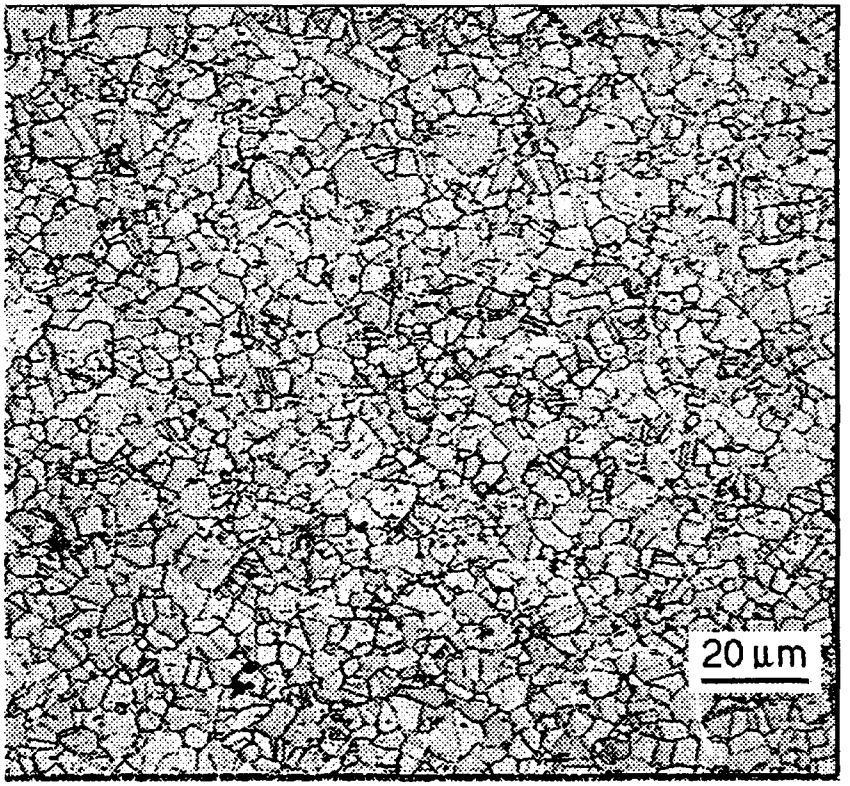

Figure 9. True stress-true strain curve and an optical micrograph from the center of the compressed sample cut through the compression axis, 800 C and 20 s^{-1}.

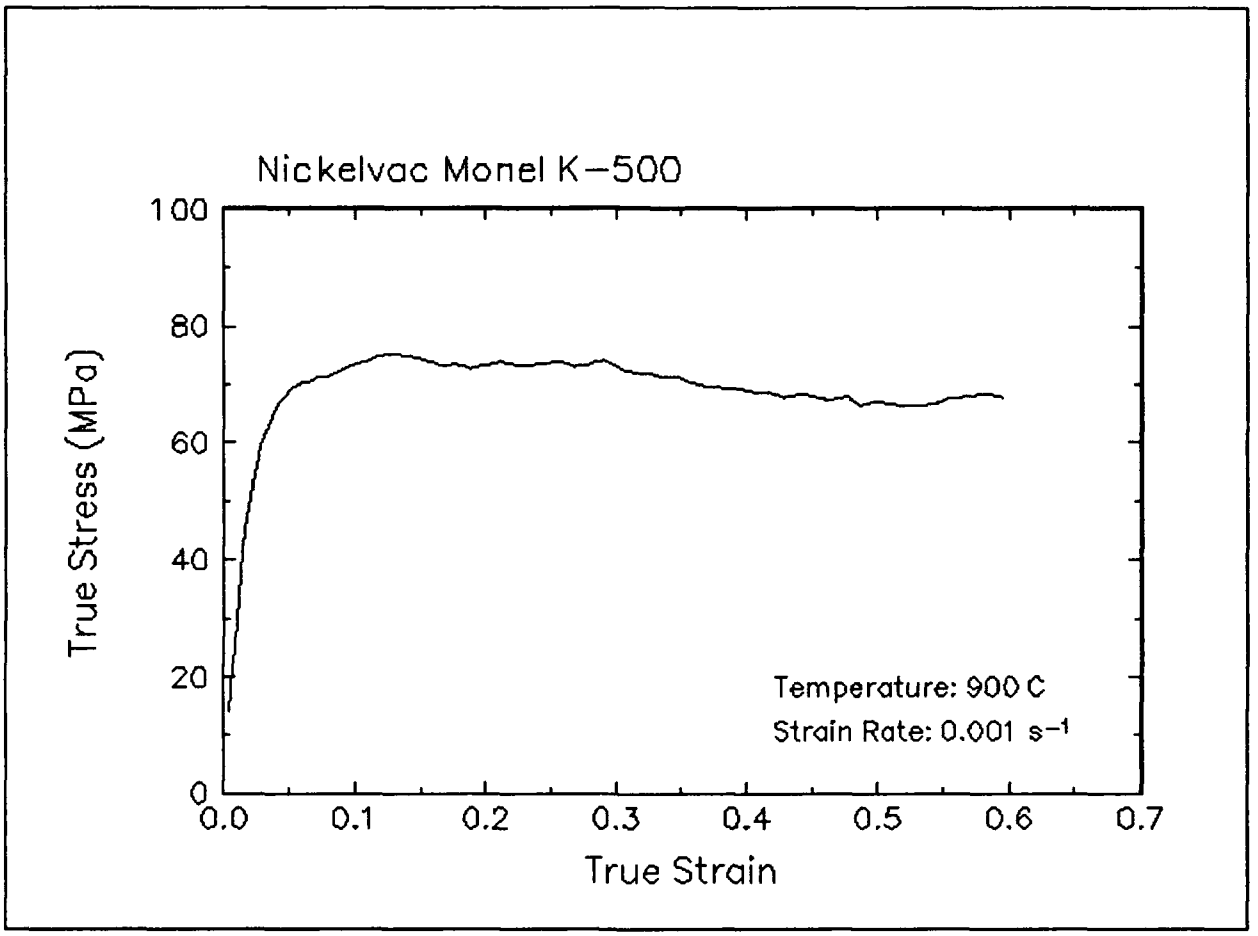

Figure 10. True stress-true strain curve, 900 C and 0.001 s^{-1}.

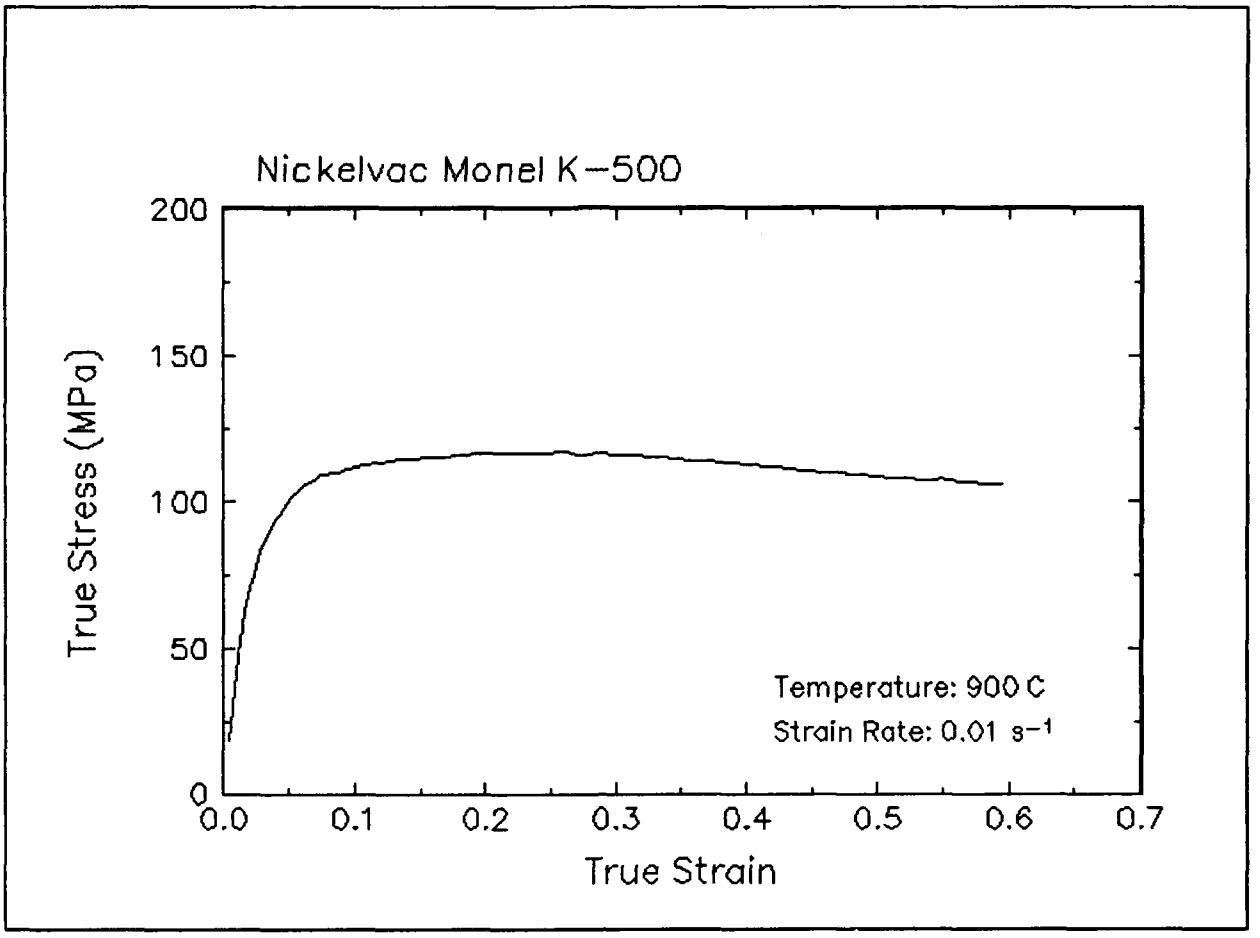

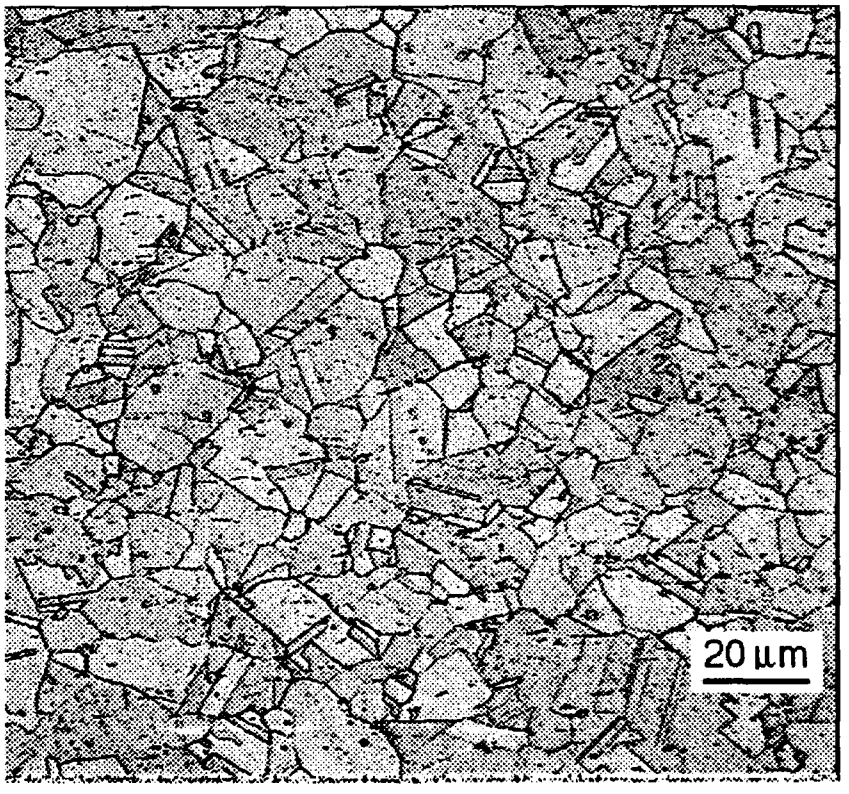

Figure 11. True stress-true strain curve and an optical micrograph from the center of the compressed sample cut through the compression axis, 900 C and 0.01 s^{-1}.

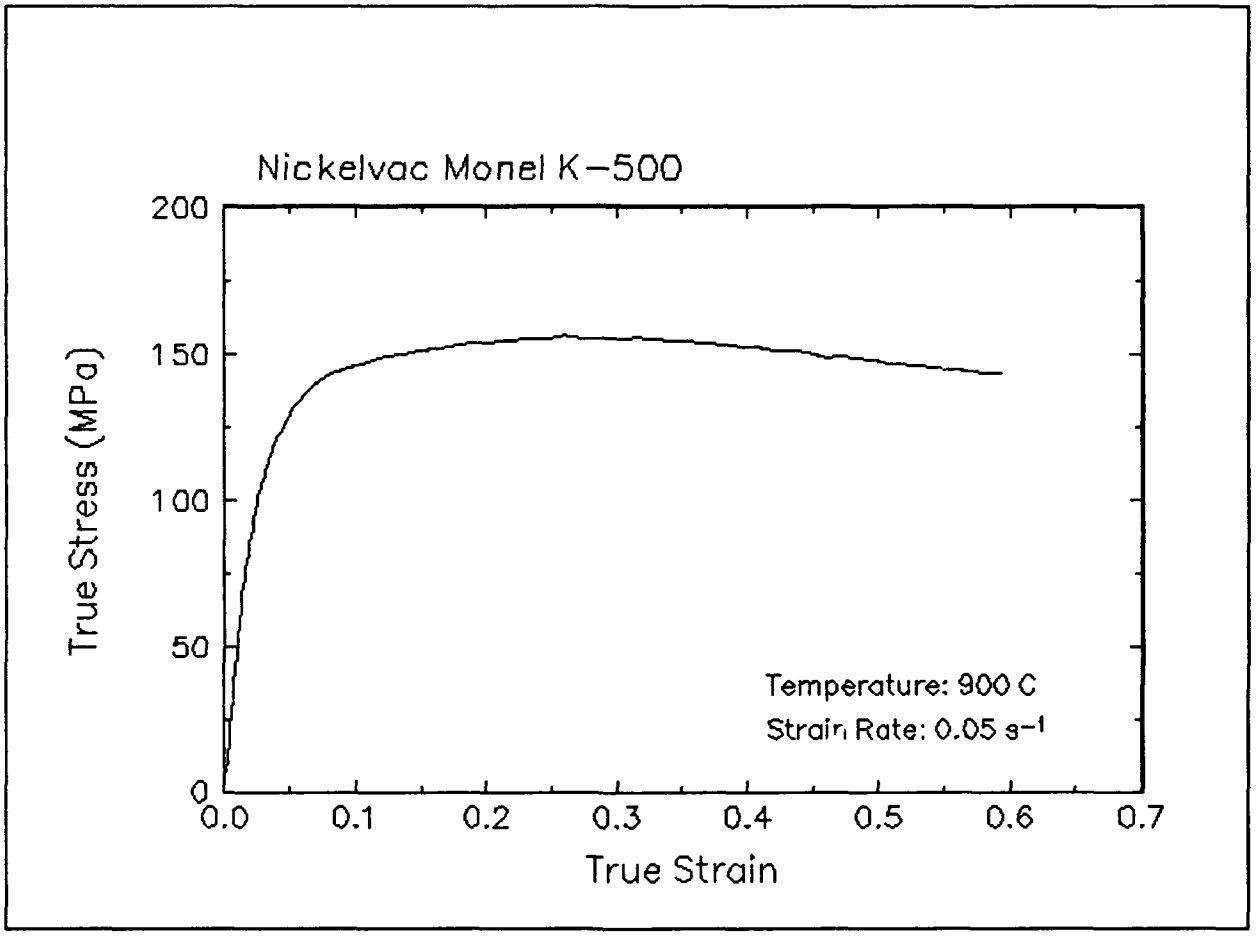

Figure 12. True stress-true strain curve, 900 C and 0.05 s^{-1}.

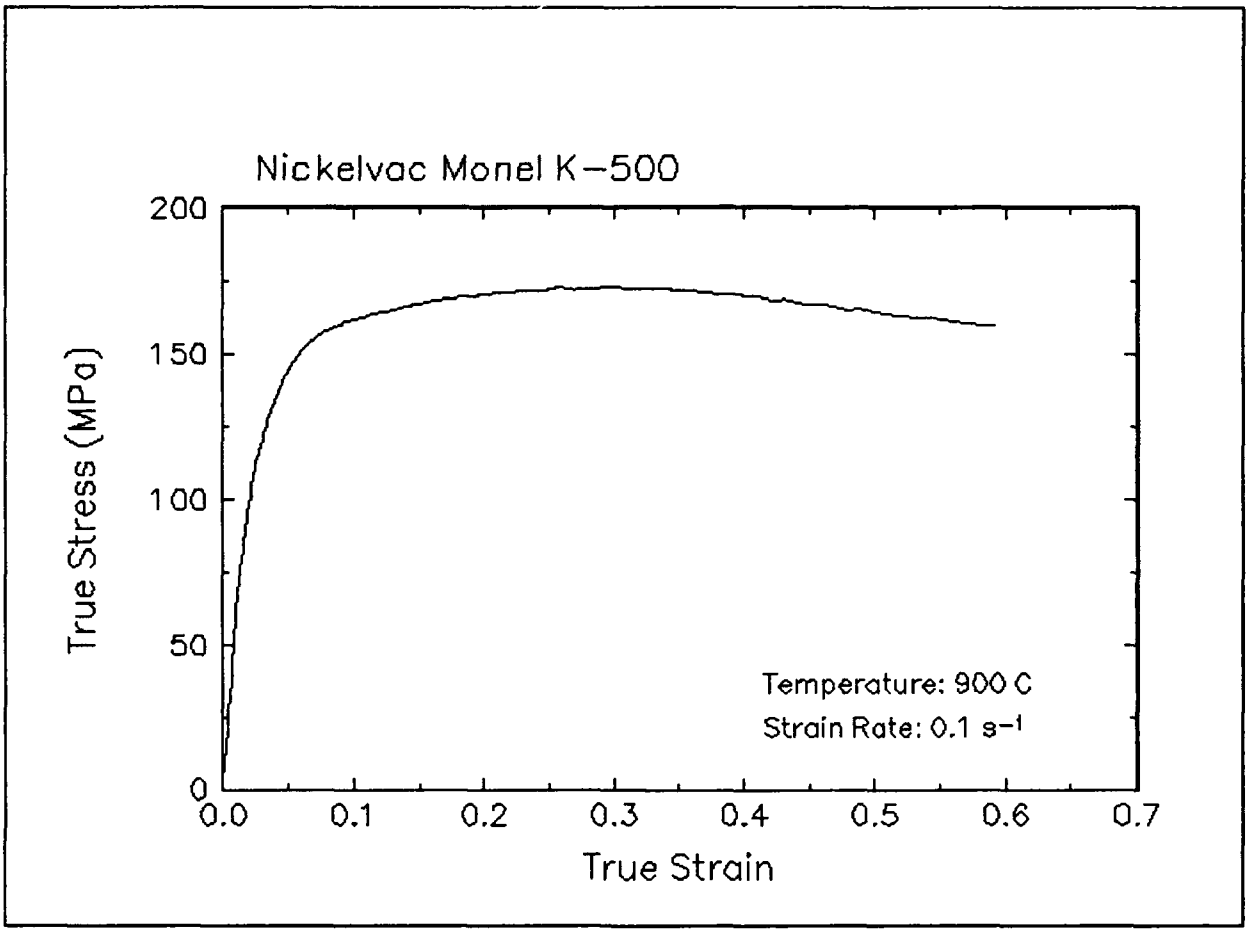

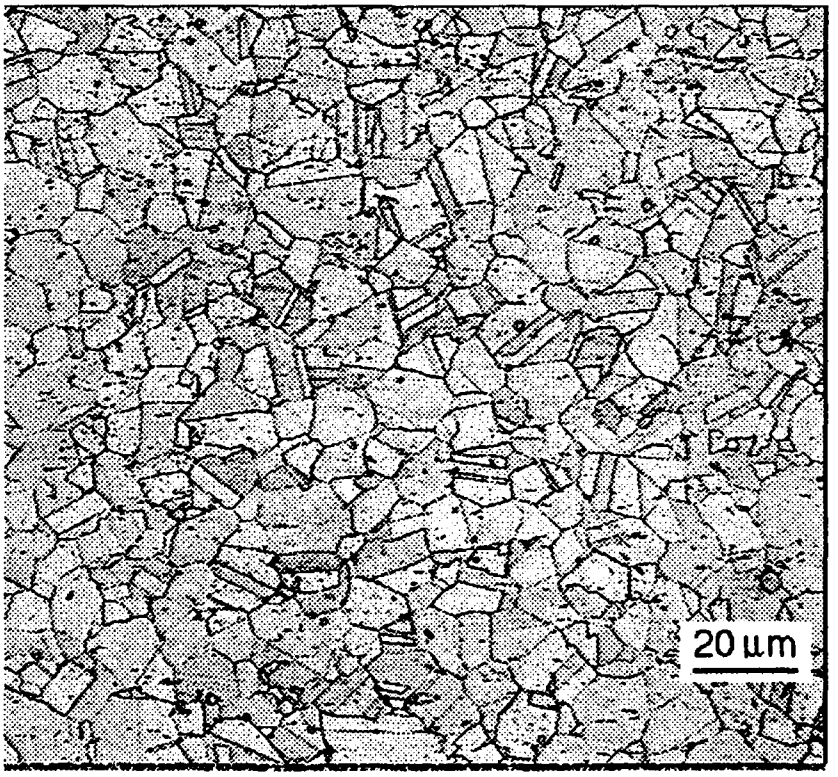

Figure 13. True stress-true strain curve and an optical micrograph from the center of the compressed sample cut through the compression axis, 900 C and 0.1 s^{-1}.

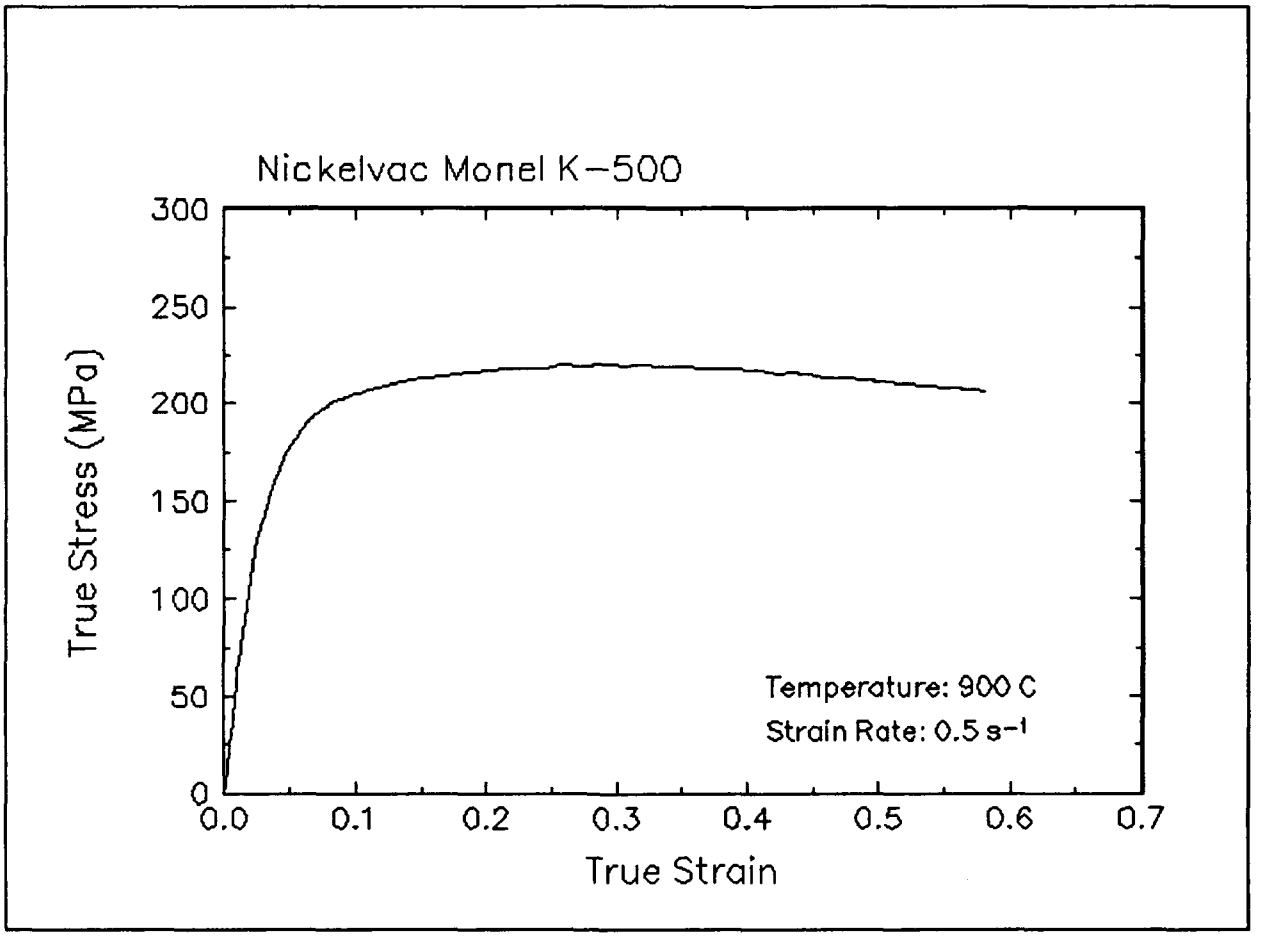

Figure 14. True stress-true strain curve, 900 C and 0.5 s^{-1}.

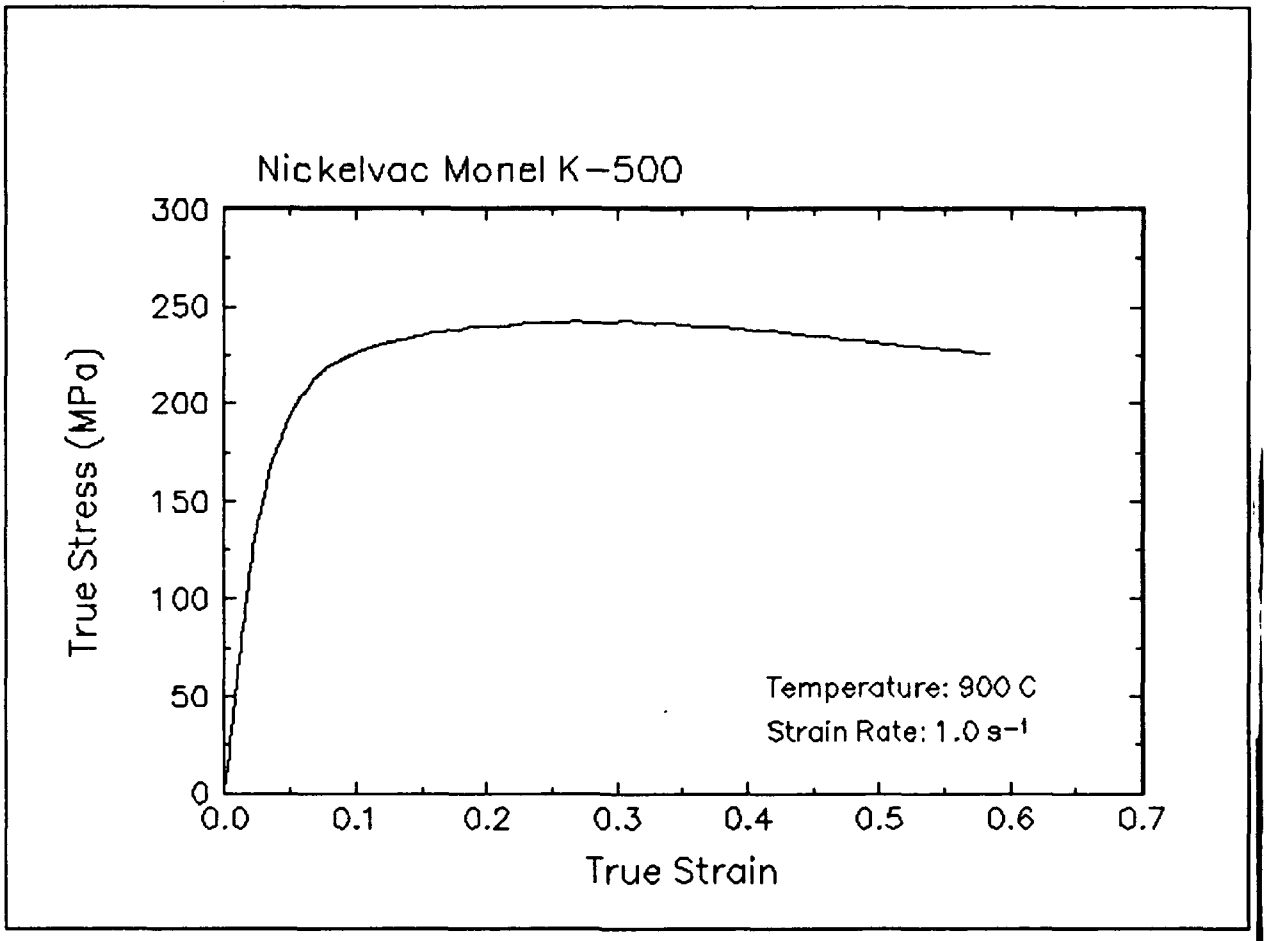

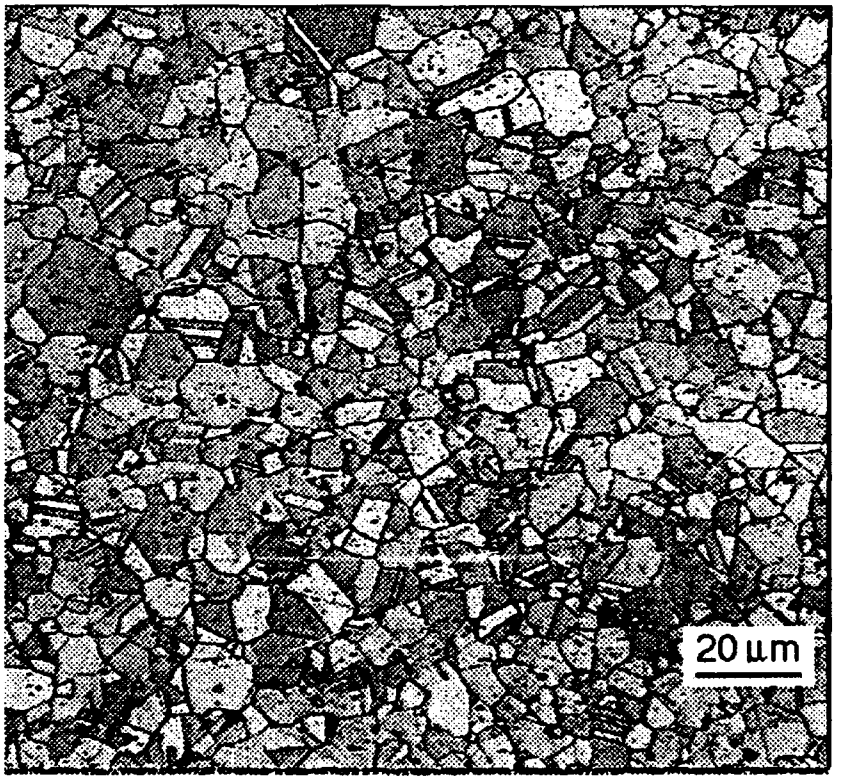

Figure 15. True stress-true strain curve and an optical micrograph from the center of the compressed sample cut through the compression axis, 900 C and 1 s^{-1}.

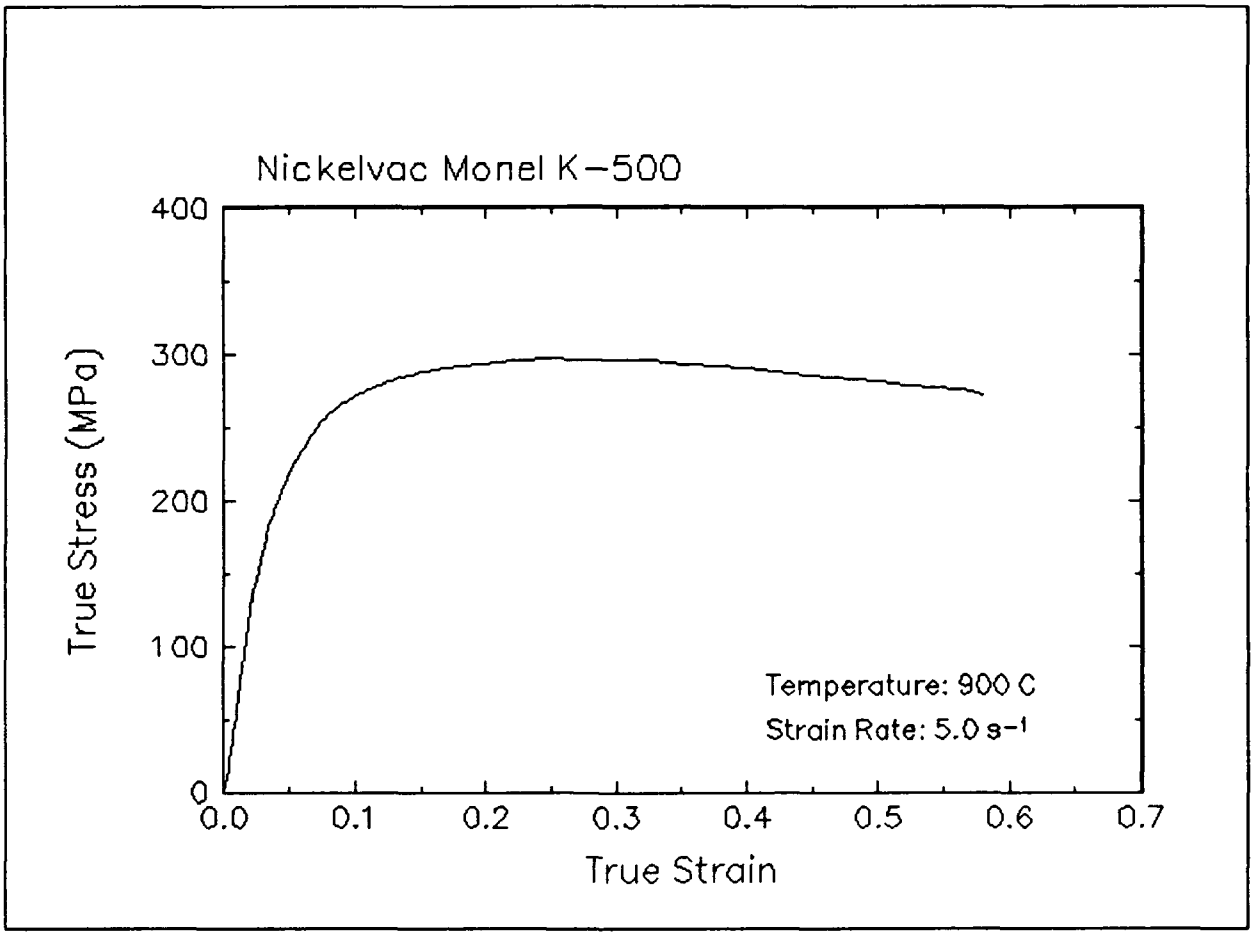

Figure 16. True stress-true strain curve, 900 C and 5 s^{-1}.

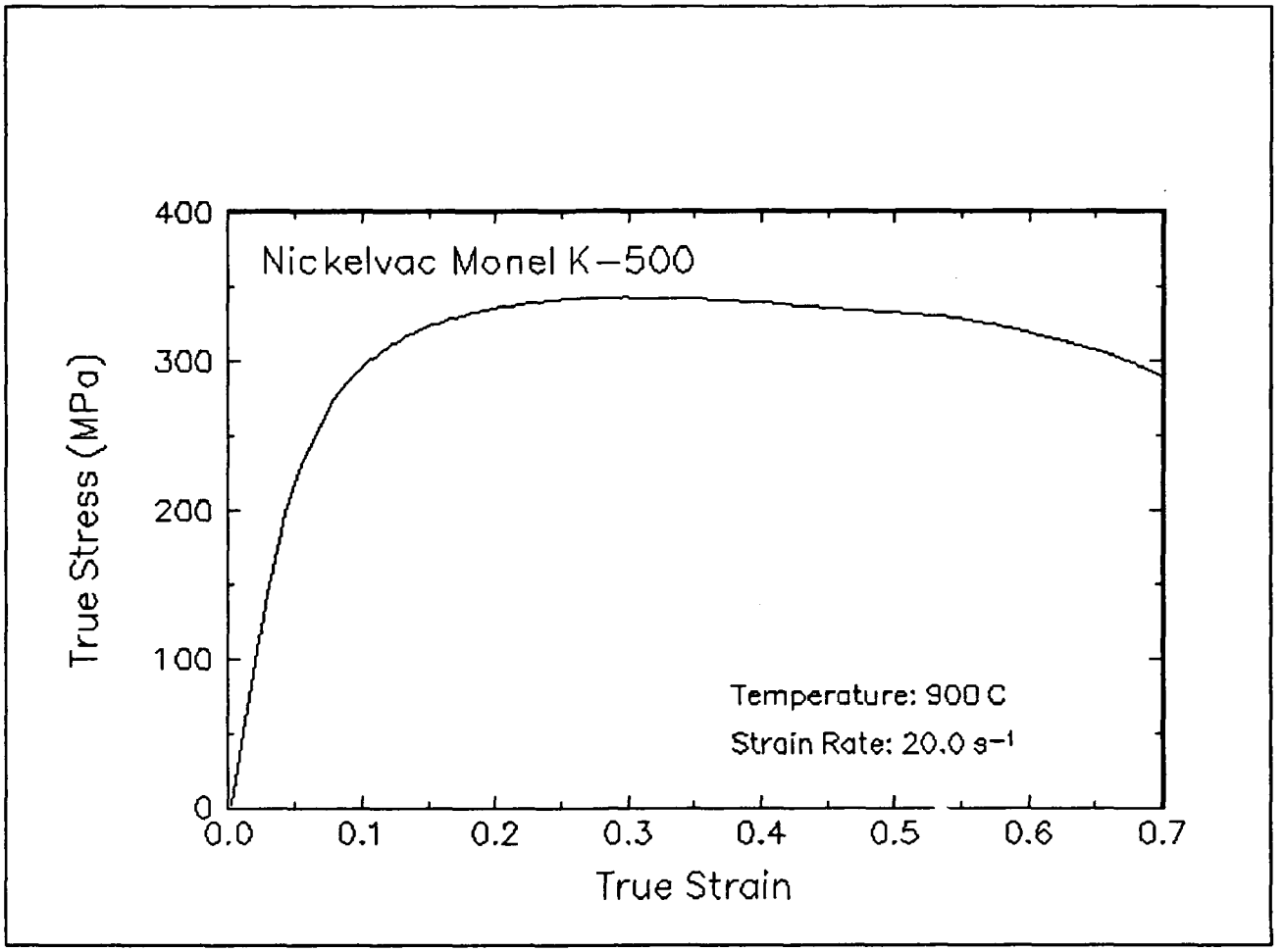

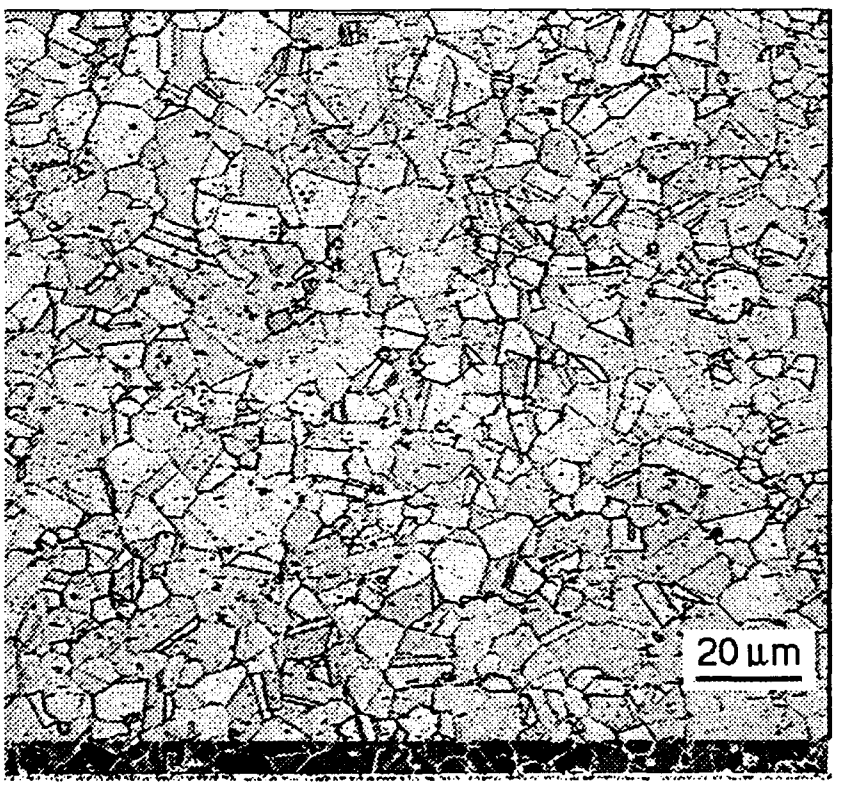

Figure 17. True stress-true strain curve and an optical micrograph from the center of the compressed sample cut through the compression axis, 900 C and 20 s^{-1}.

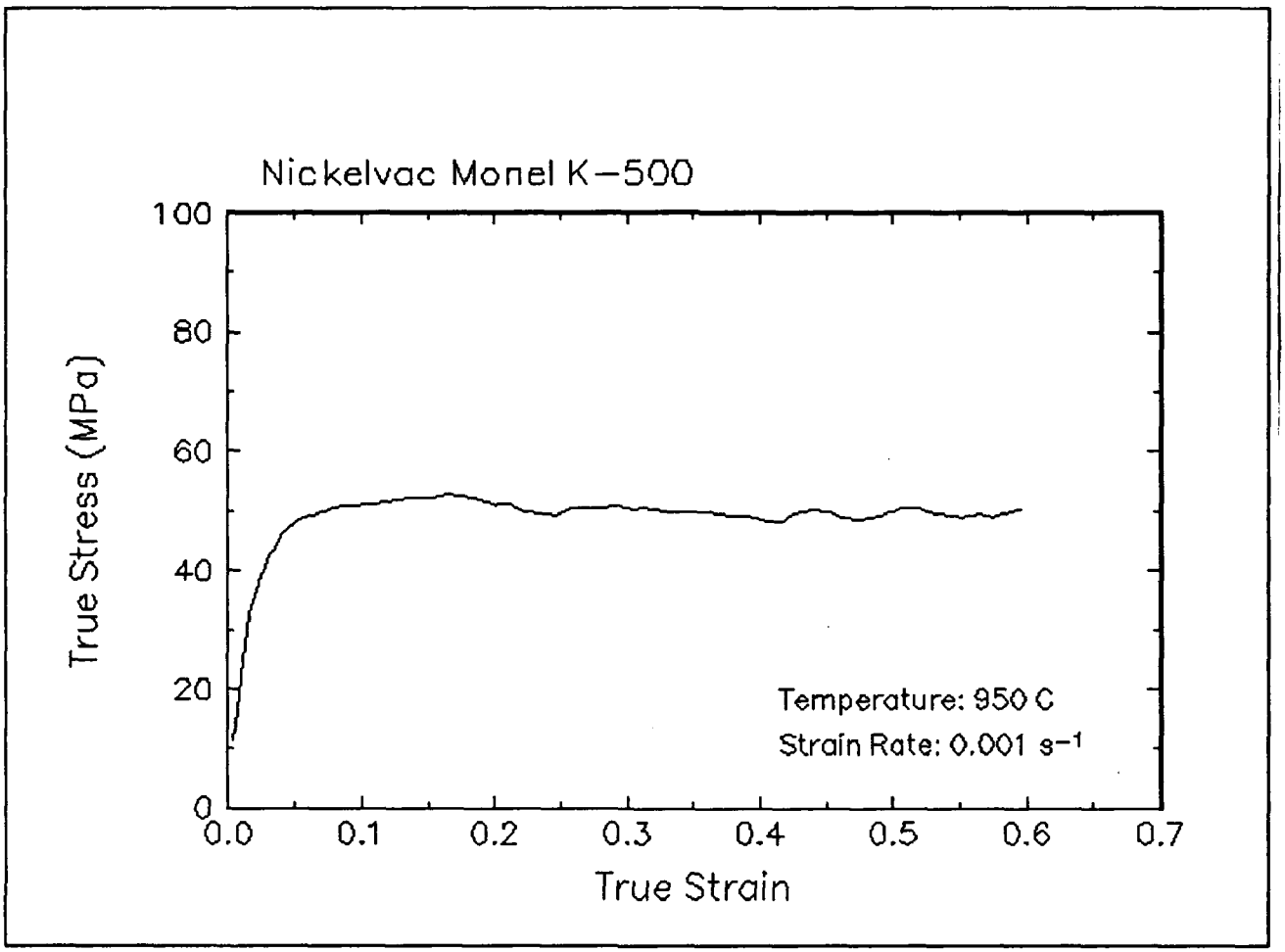

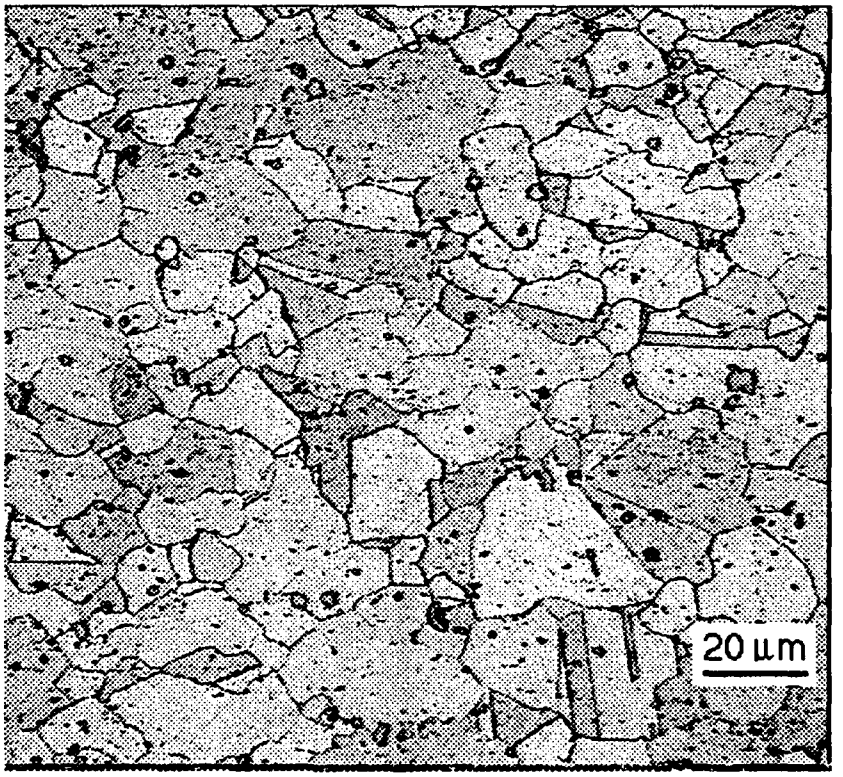

Figure 18. True stress-true strain curve and an optical micrograph from the center of the compressed sample cut through the compression axis, 950 C and 0.001 s^{-1}.

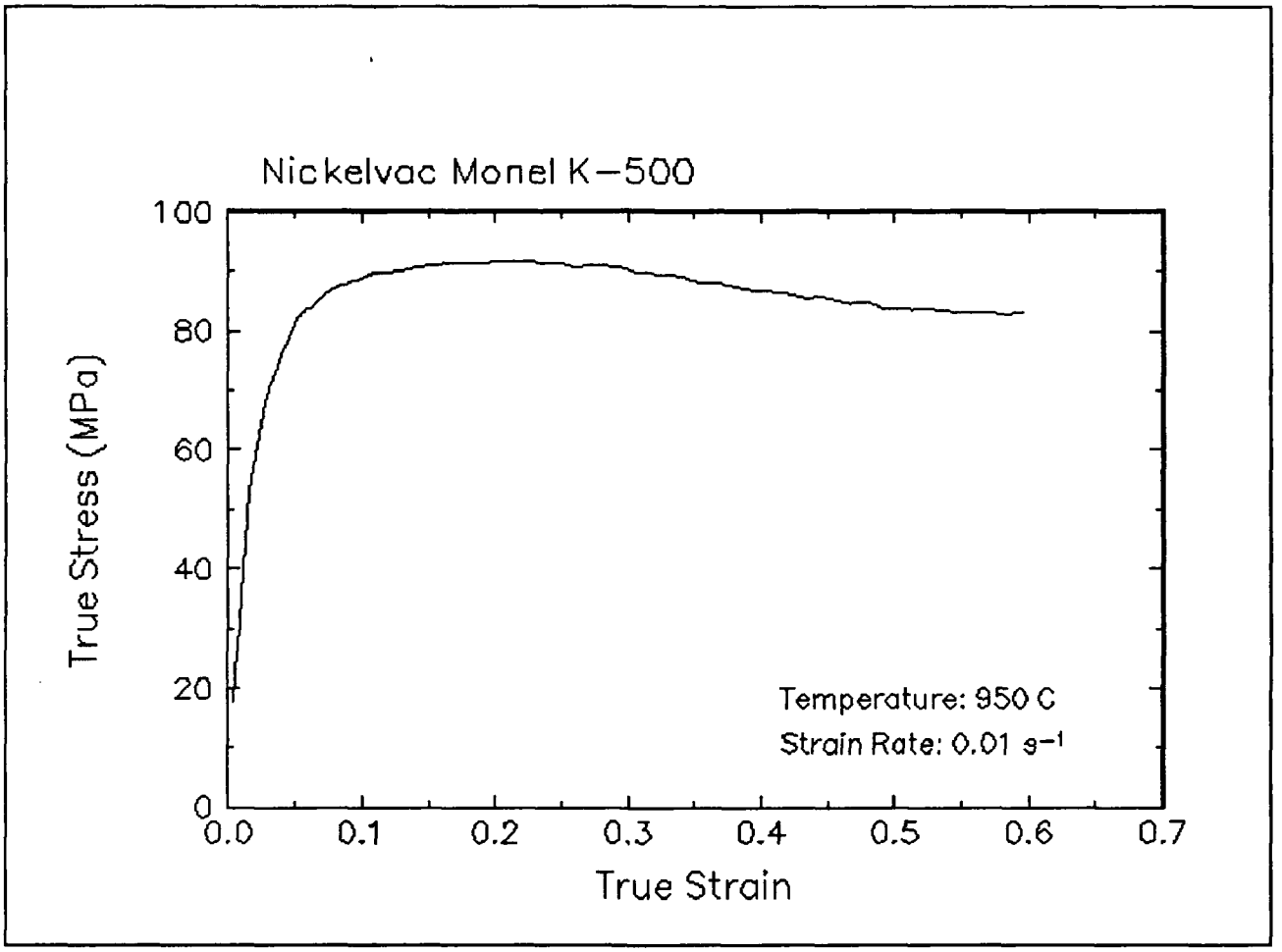

Figure 19. True stress-true strain curve, 950 C and 0.01 s^{-1}.

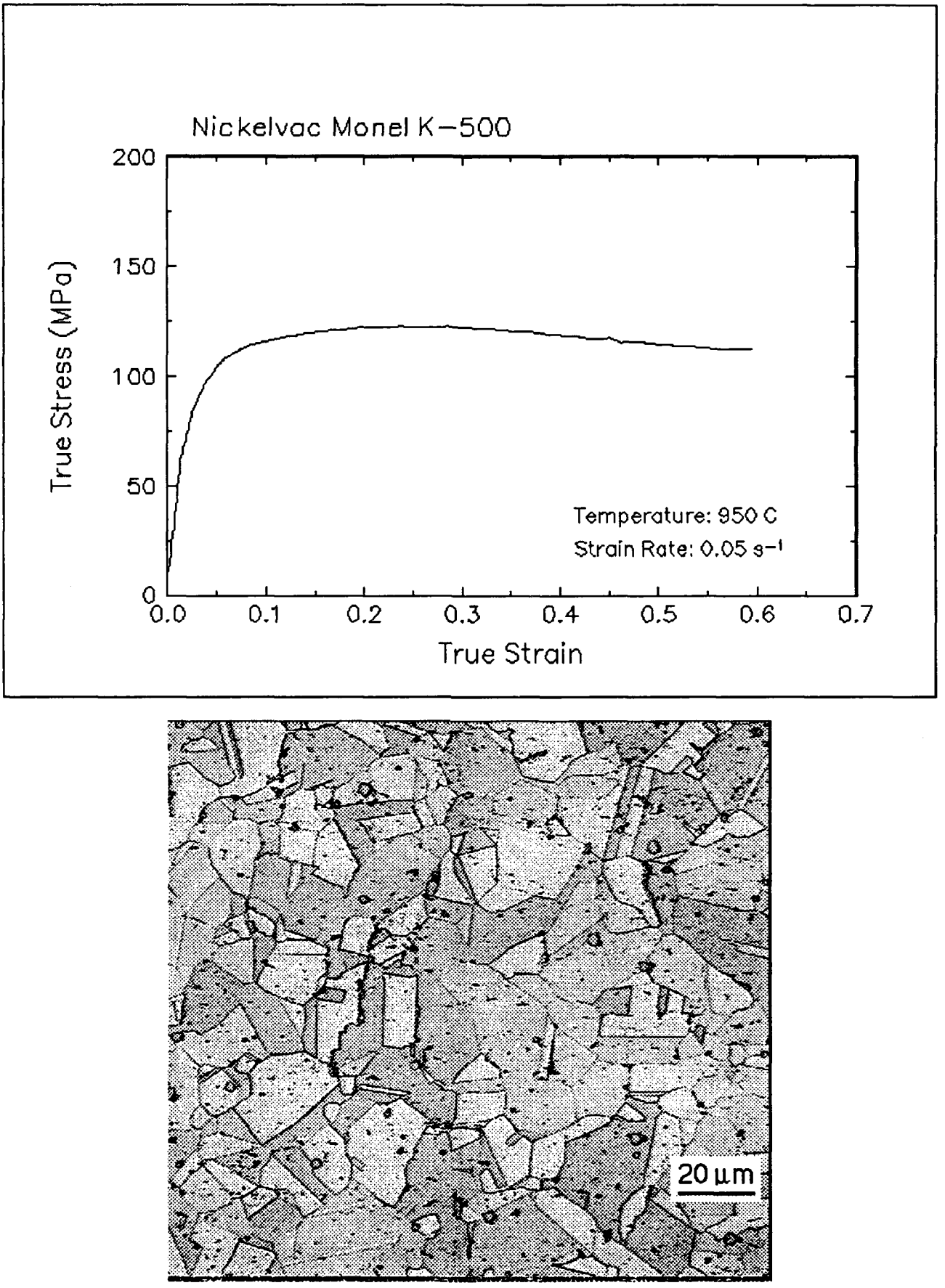

Figure 20. True stress-true strain curve and an optical micrograph from the center of the compressed sample cut through the compression axis, 950 C and 0.05 s^{-1}.

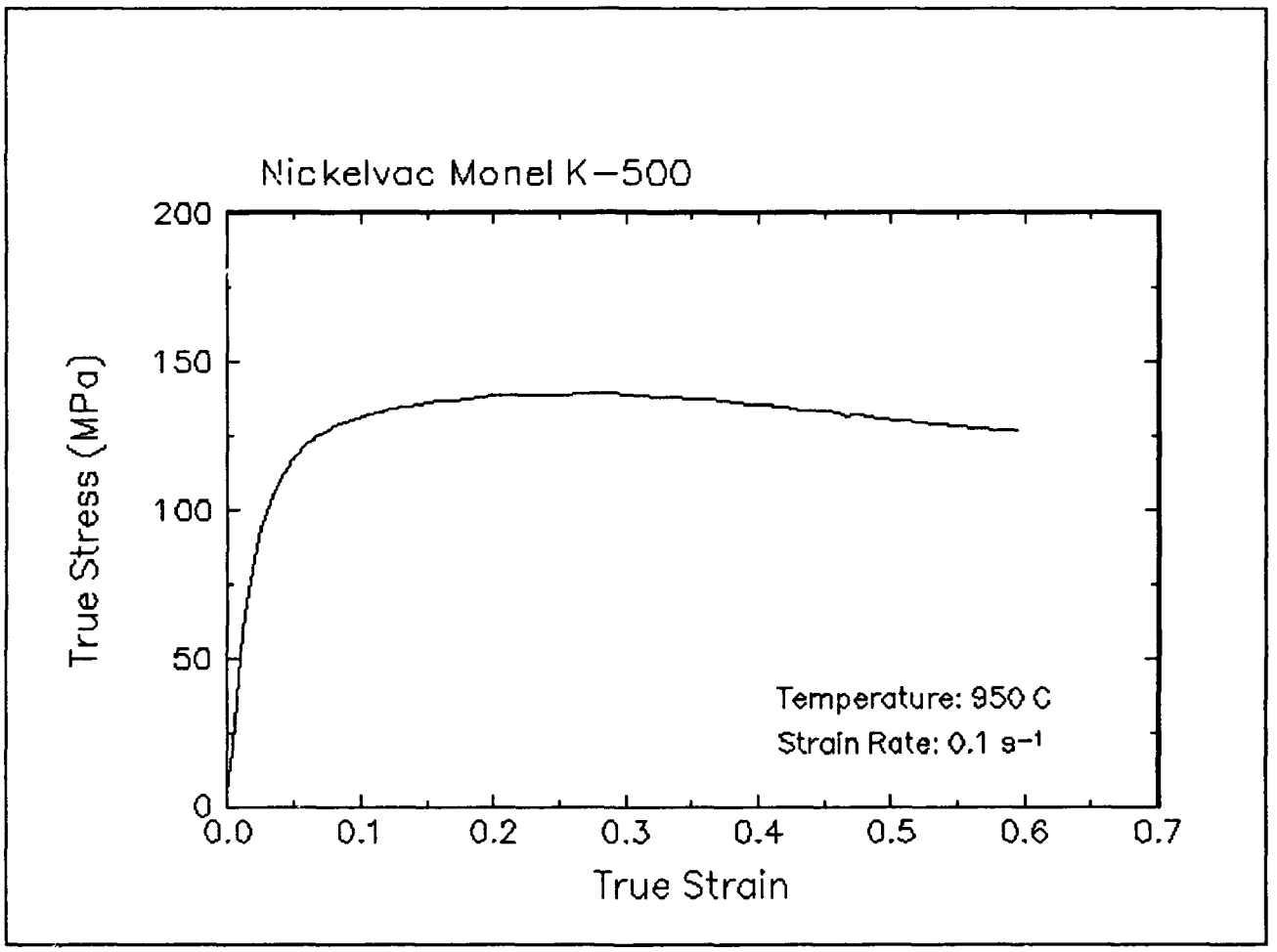

Figure 21. True stress-true strain curve, 950 C and 0.1 s^{-1}.

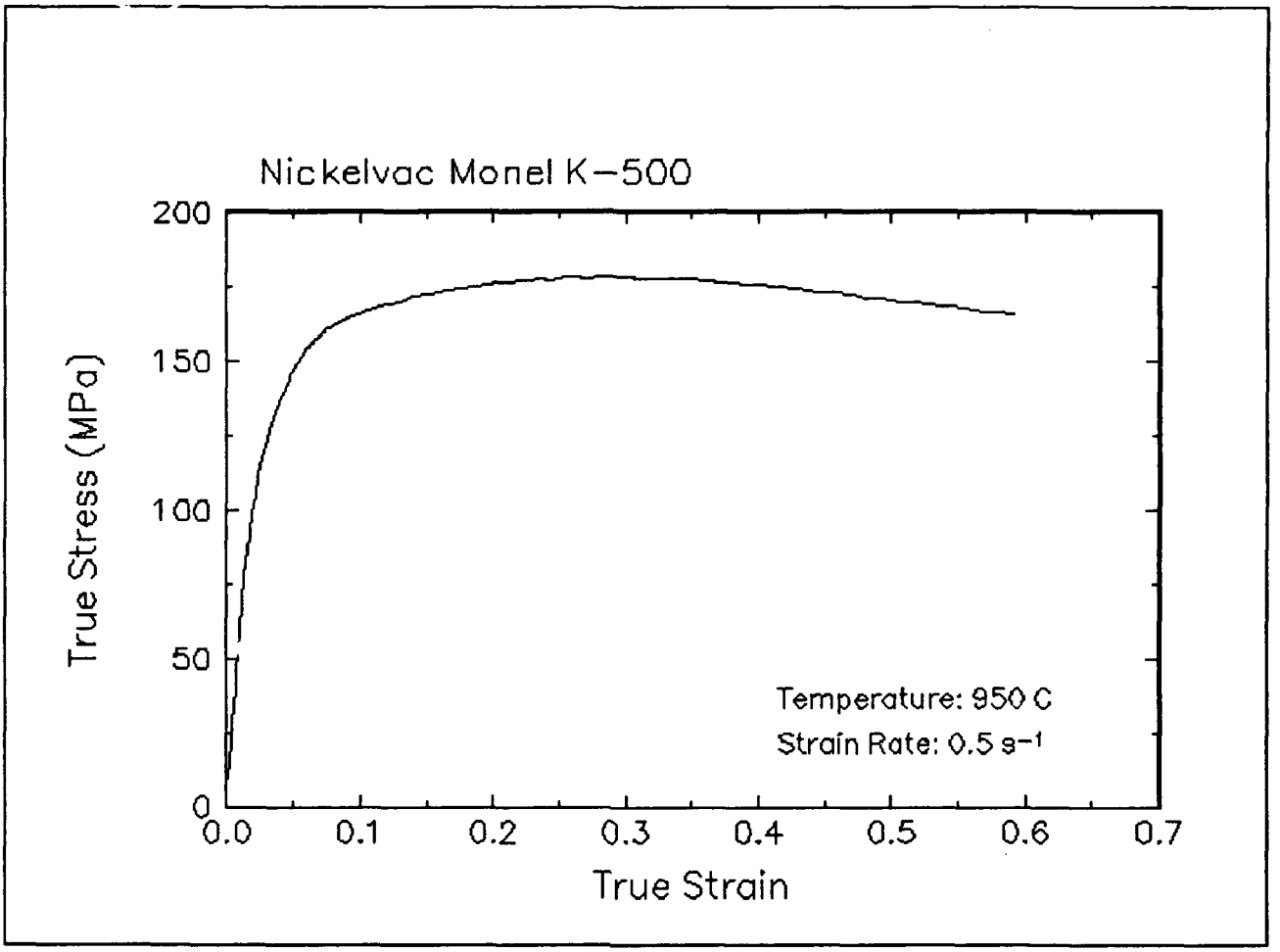

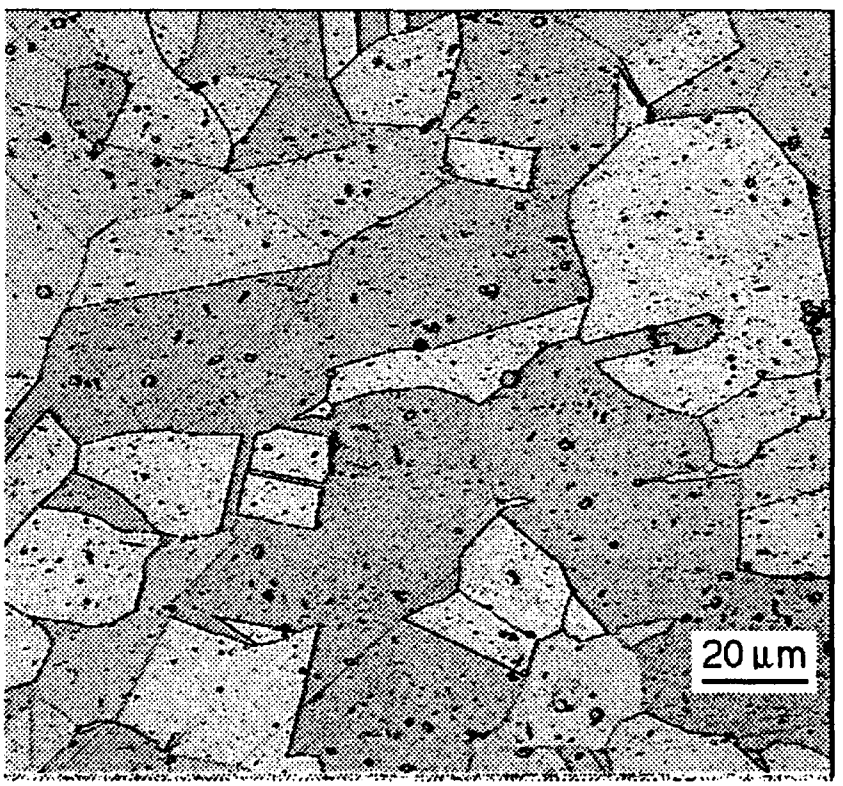

Figure 22. True stress-true strain curve and an optical micrograph from the center of the compressed sample cut through the compression axis, 950 C and 0.5 s^{-1}.

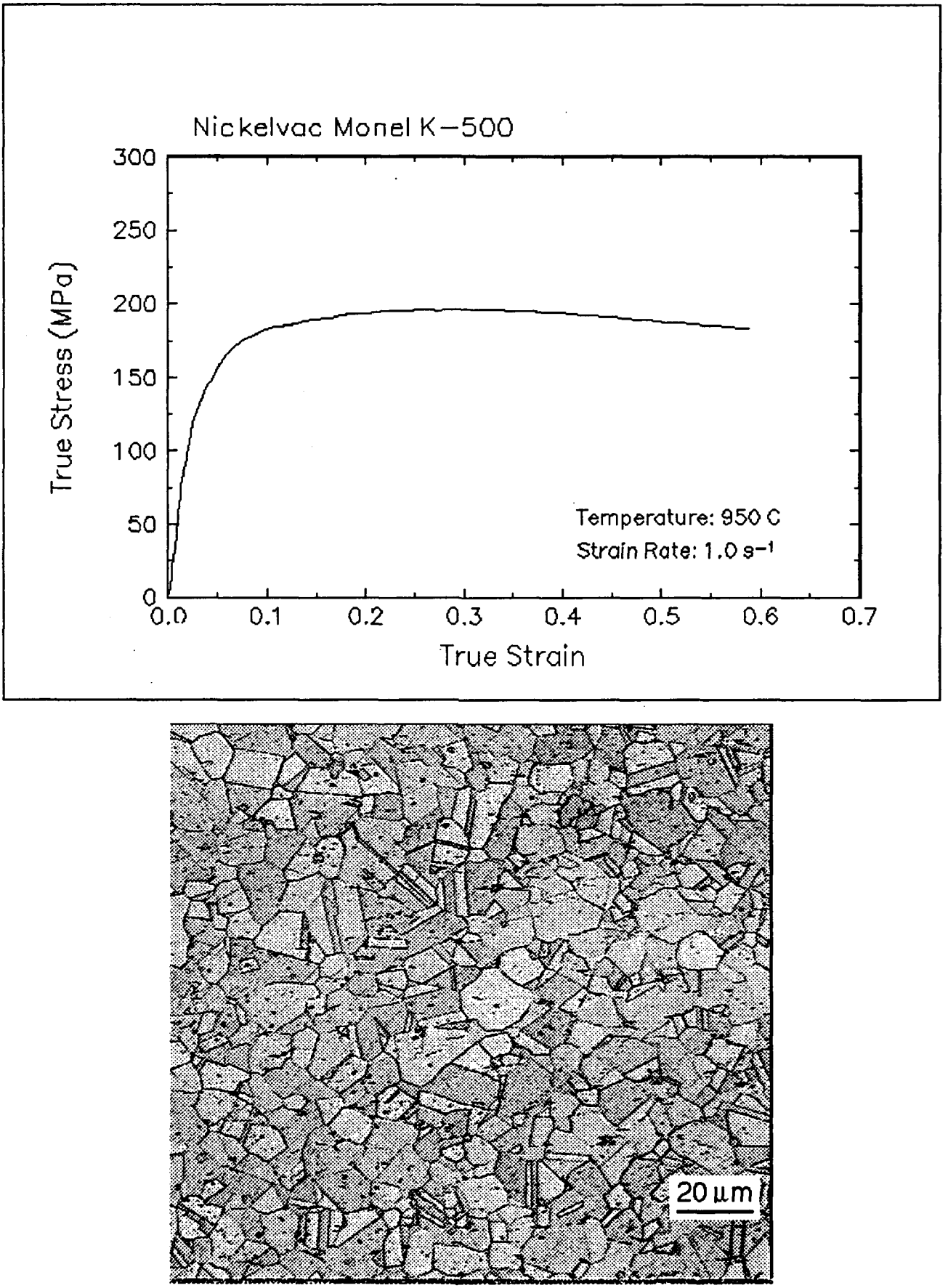

Figure 23. True stress-true strain curve and an optical micrograph from the center of the compressed sample cut through the compression axis, 950 C and 1 s^{-1}.

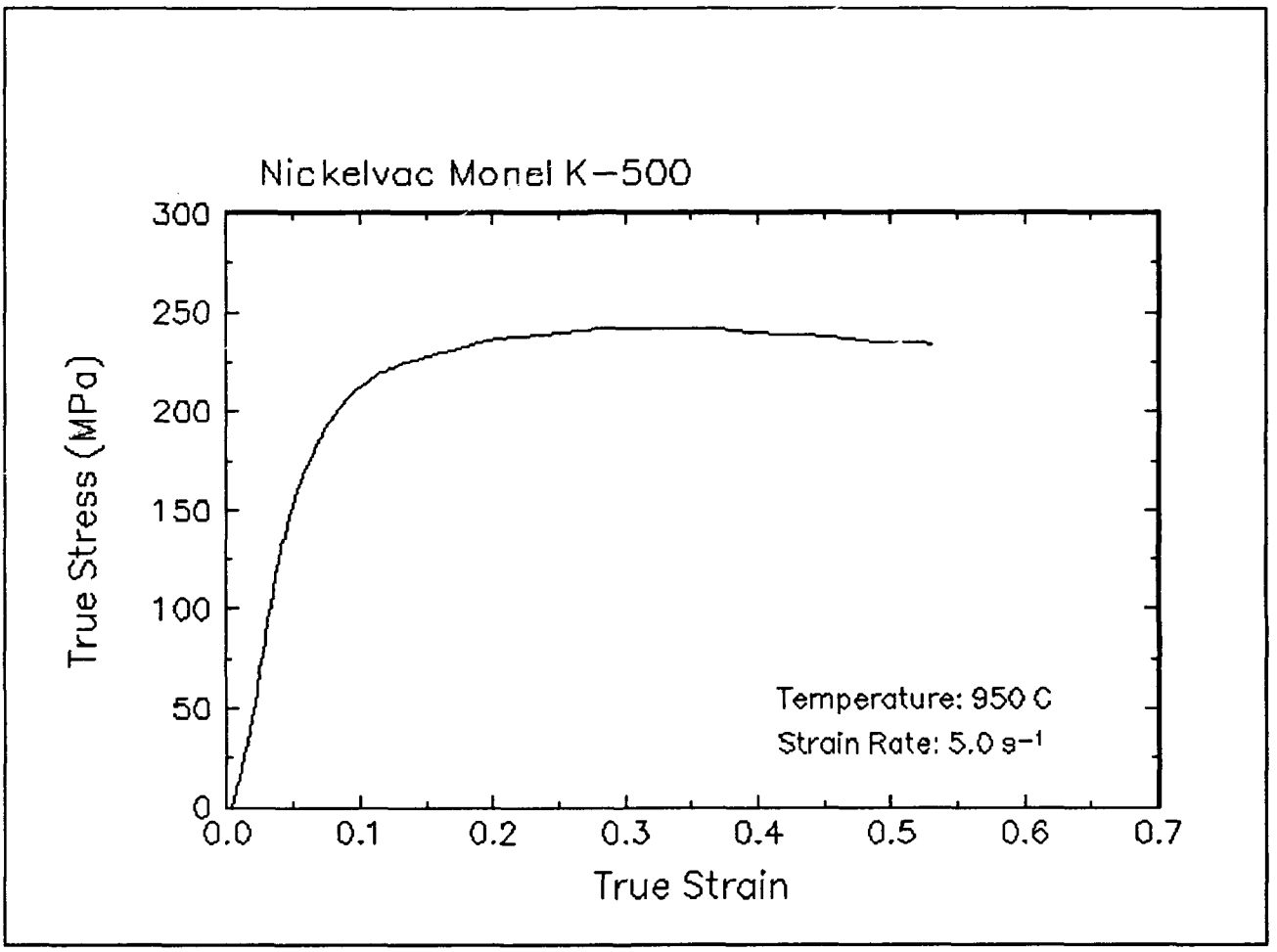

Figure 24. True stress-true strain curve, 950 C and 5 s^{-1}.

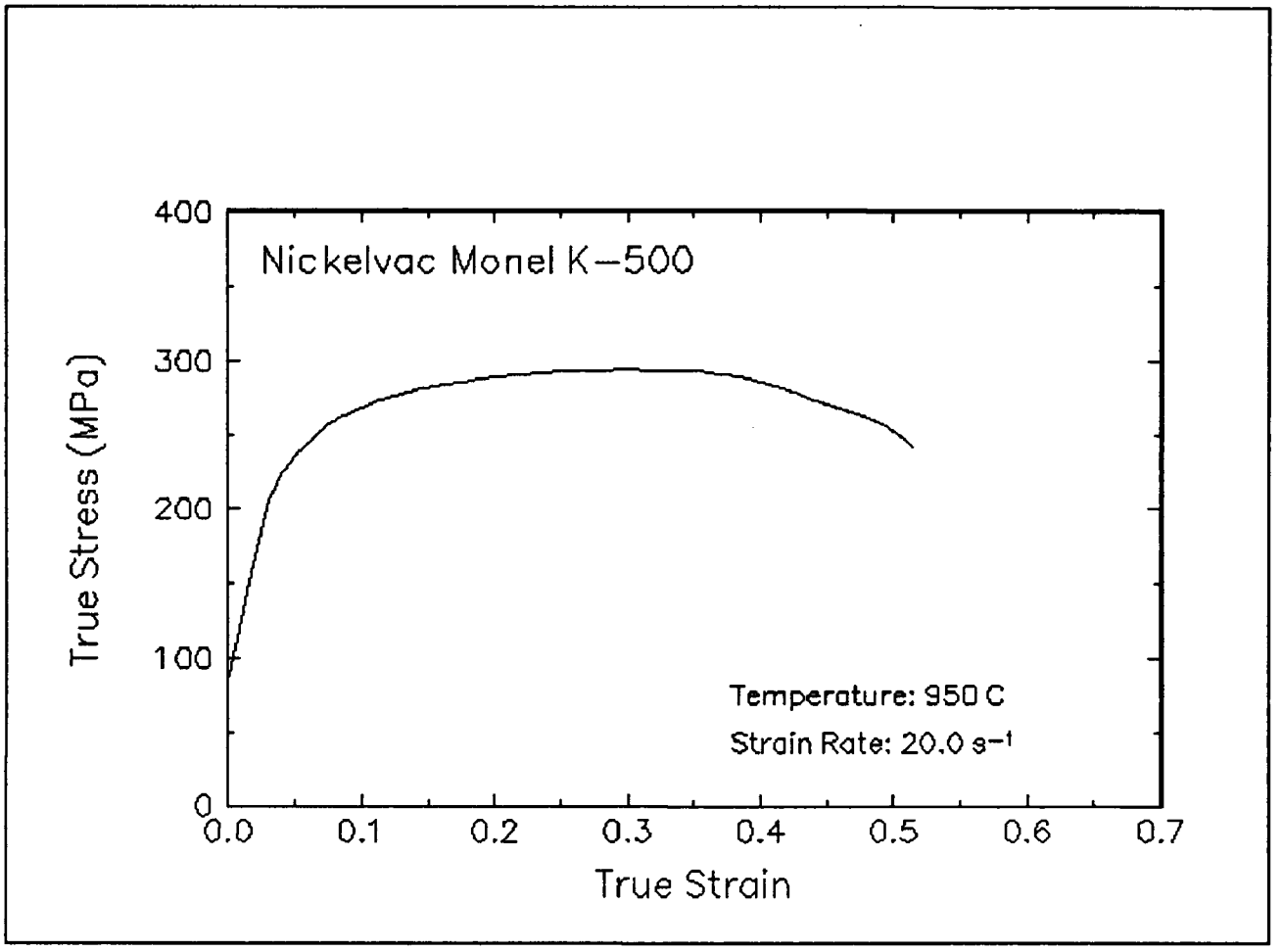

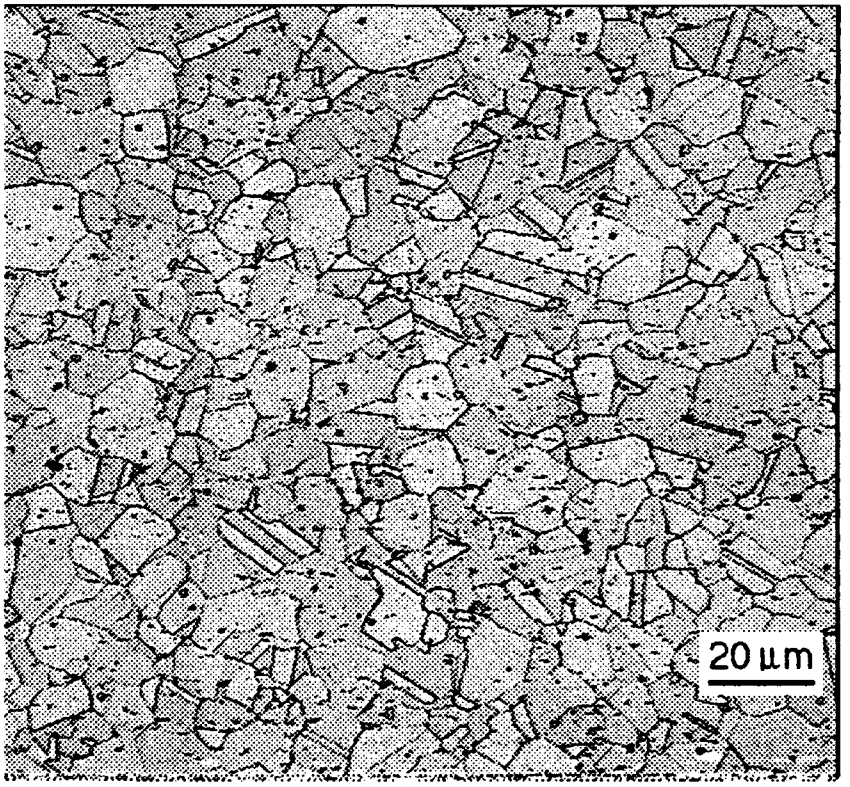

Figure 25. True stress-true strain curve and an optical micrograph from the center of the compressed sample cut through the compression axis, 950 C and 20 s^{-1}.

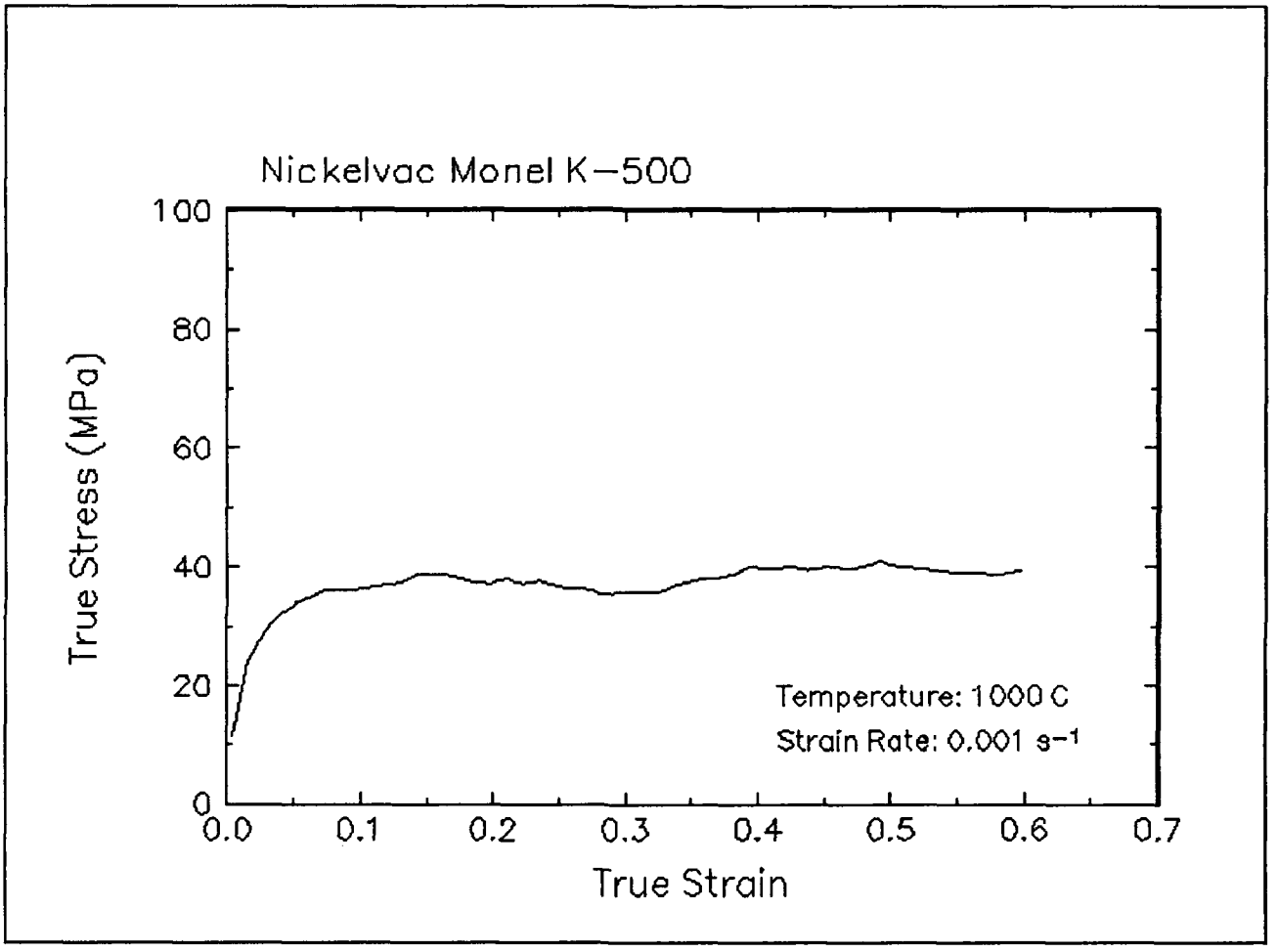

Figure 26. True stress-true strain curve, 1000 C and 0.001 s^{-1}.

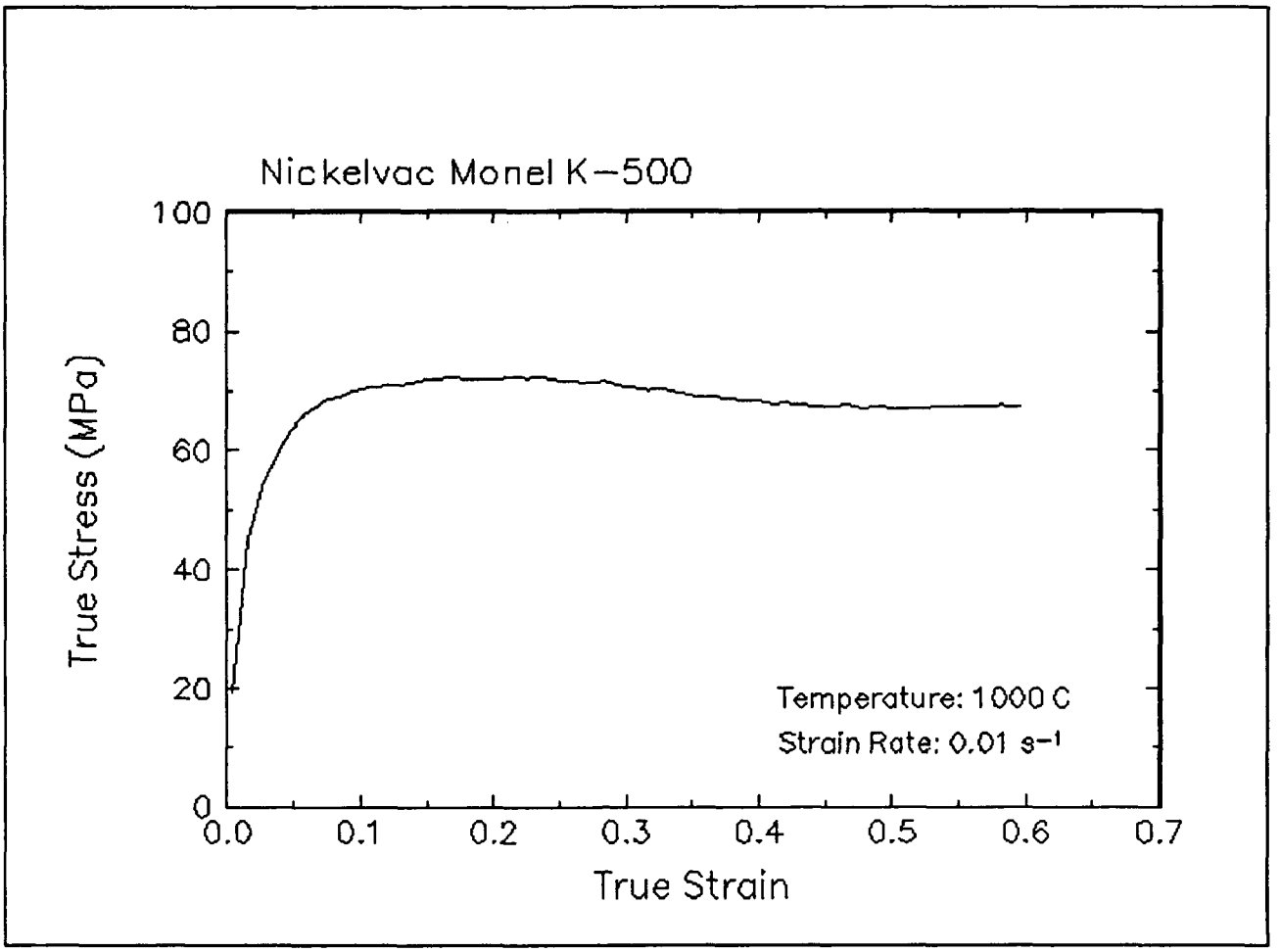

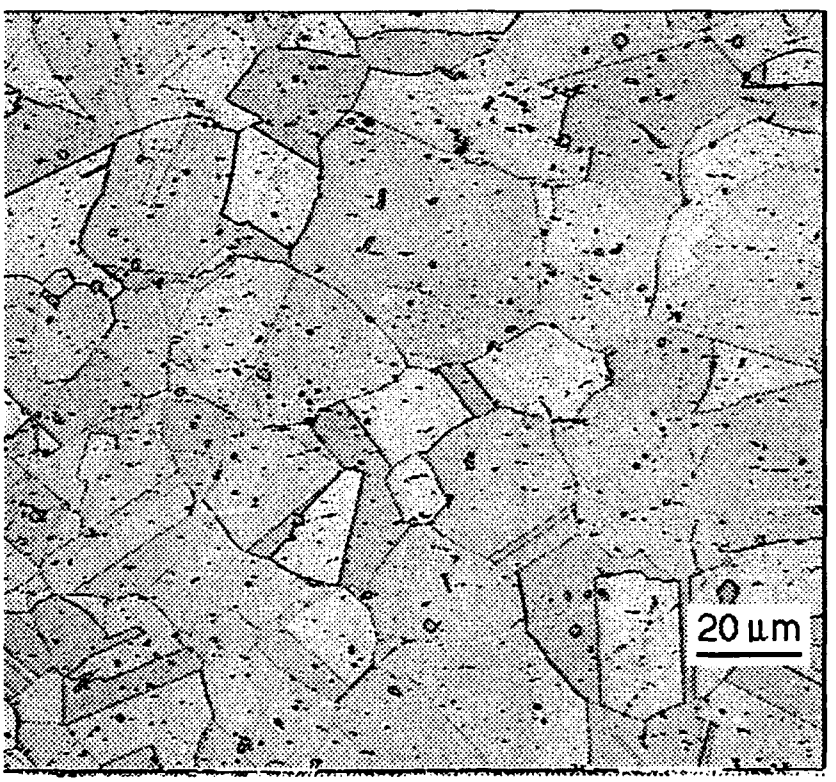

Figure 27. True stress-true strain curve and an optical micrograph from the center of the compressed sample cut through the compression axis, 1000 C and 0.01 s^{-1}.

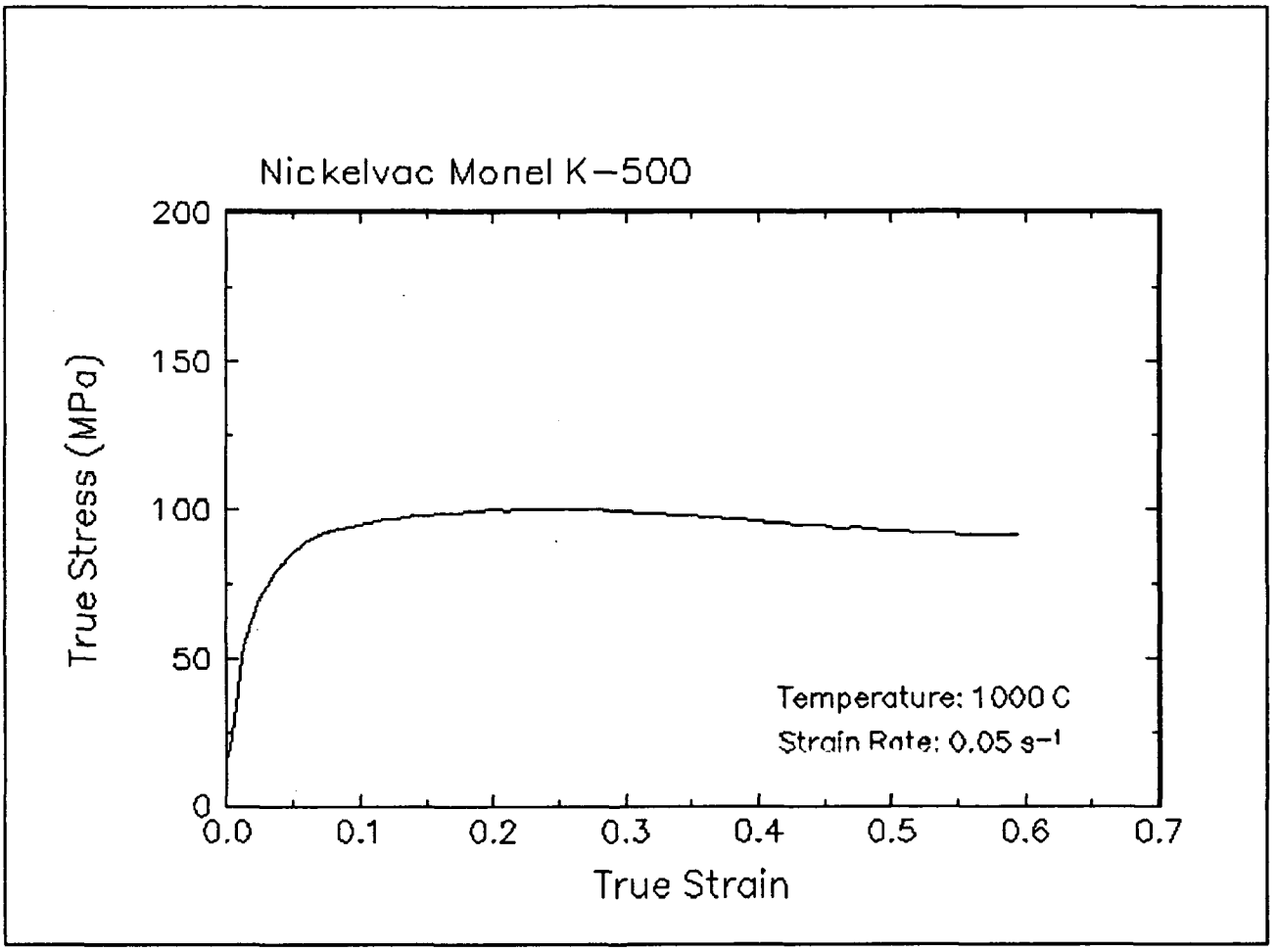

Figure 28. True stress-true strain curve, 1000 C and 0.05 s^{-1}.

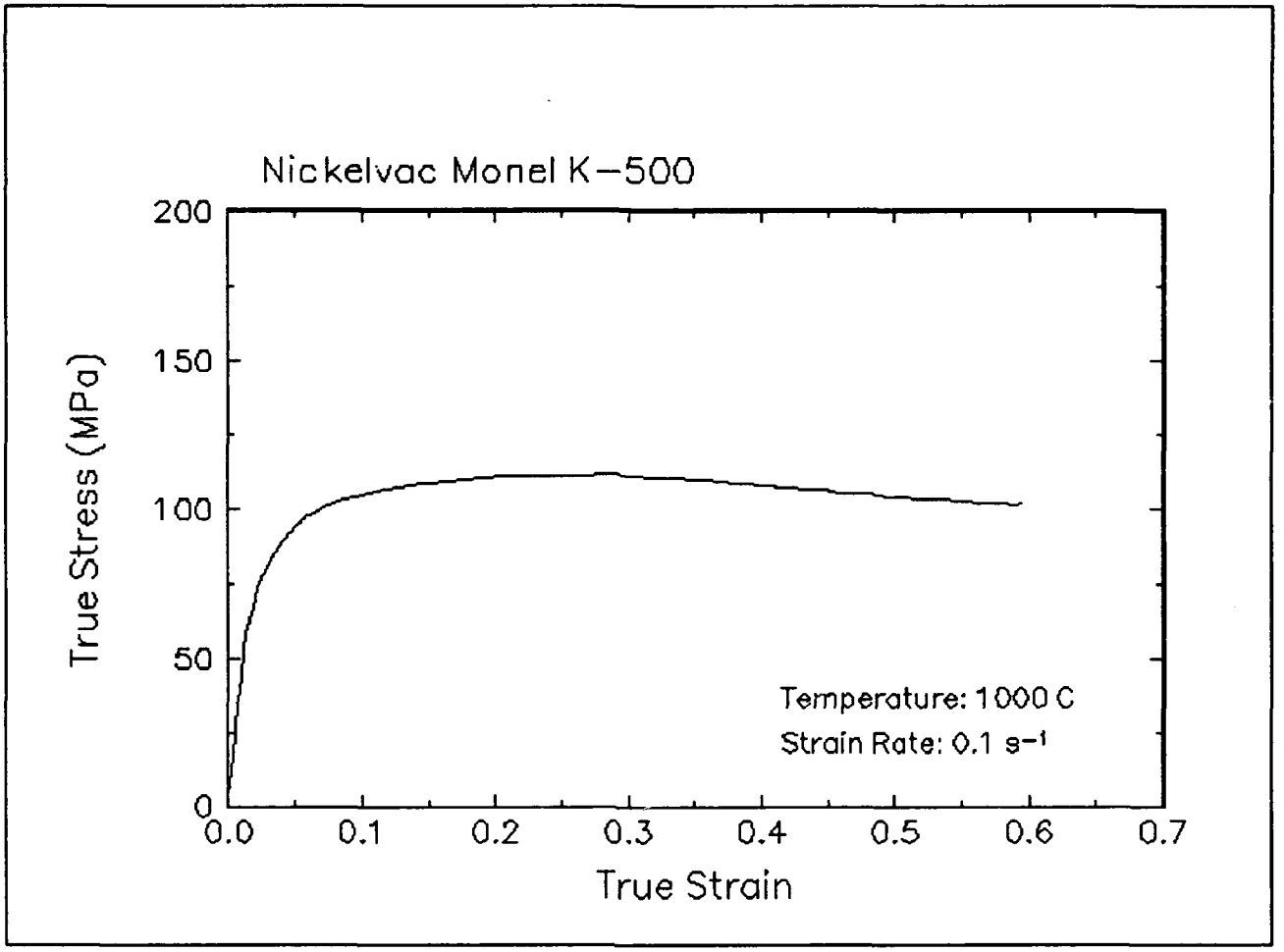

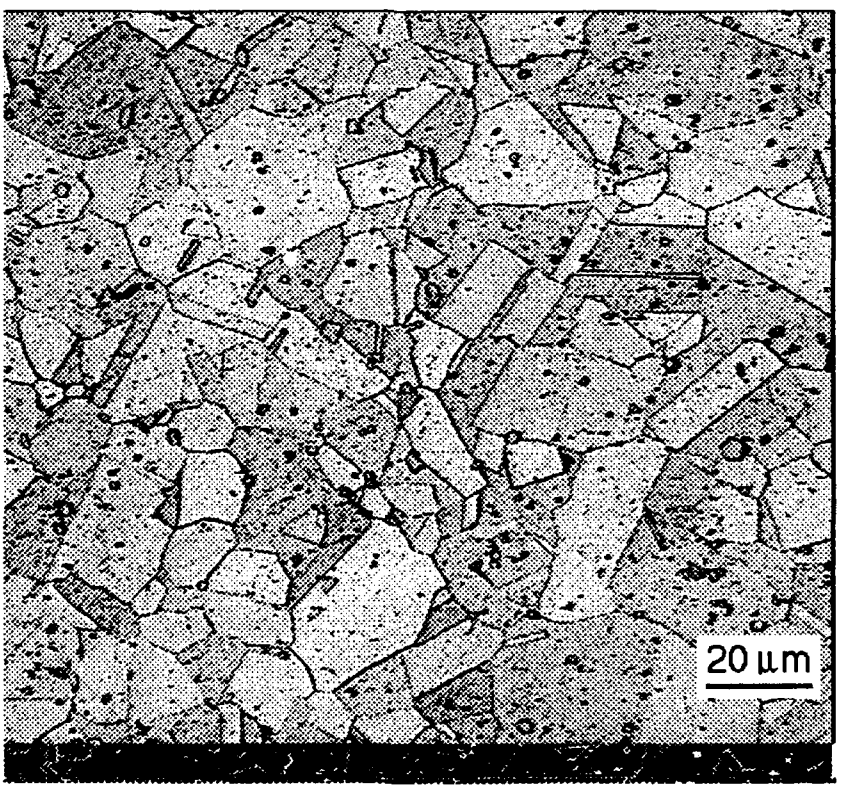

Figure 29. True stress-true strain curve and an optical micrograph from the center of the compressed sample cut through the compression axis, 1000 C and 0.1 s^{-1}.

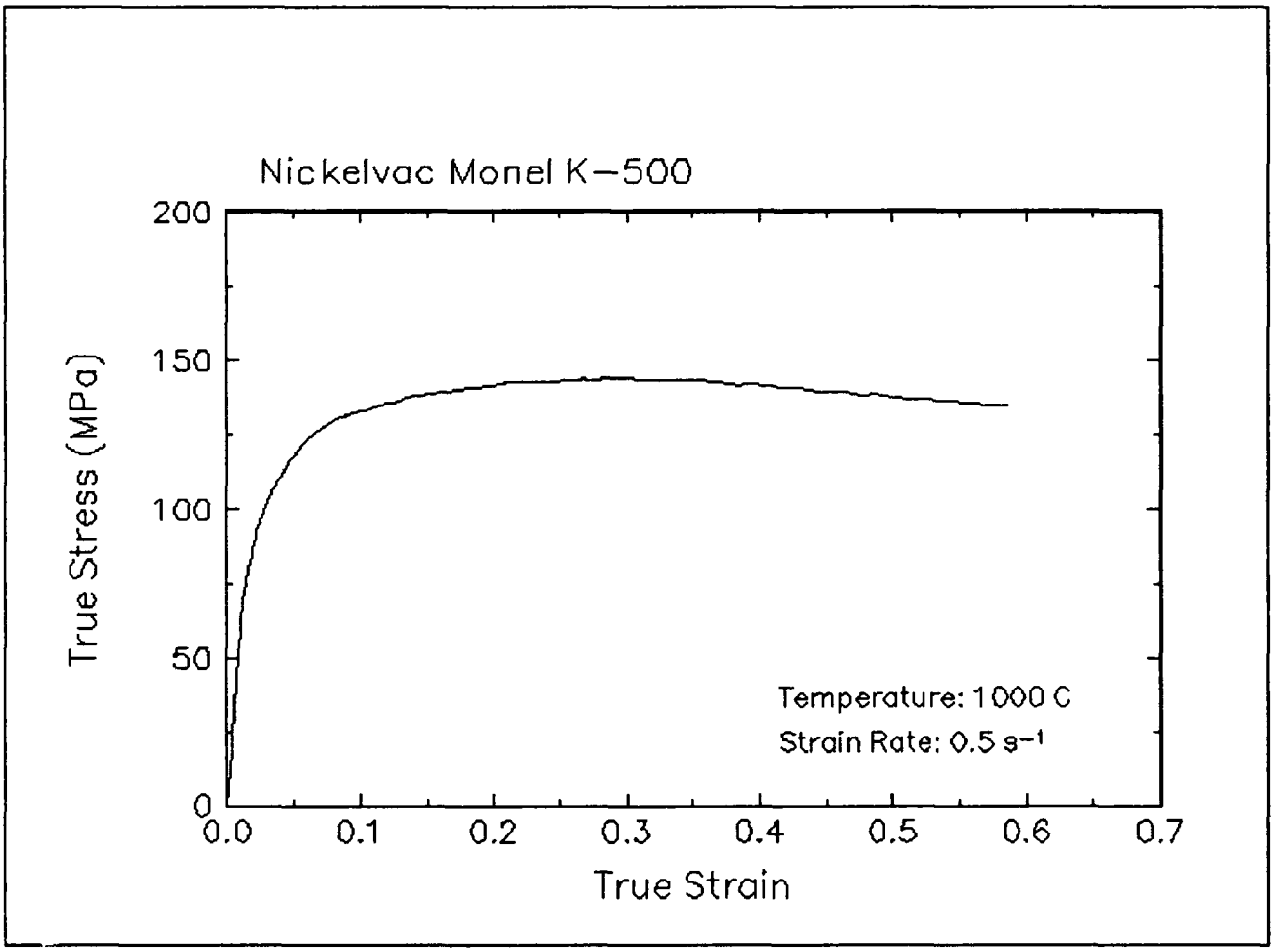

Figure 30. True stress-true strain curve, 1000 C and 0.5 s^{-1}.

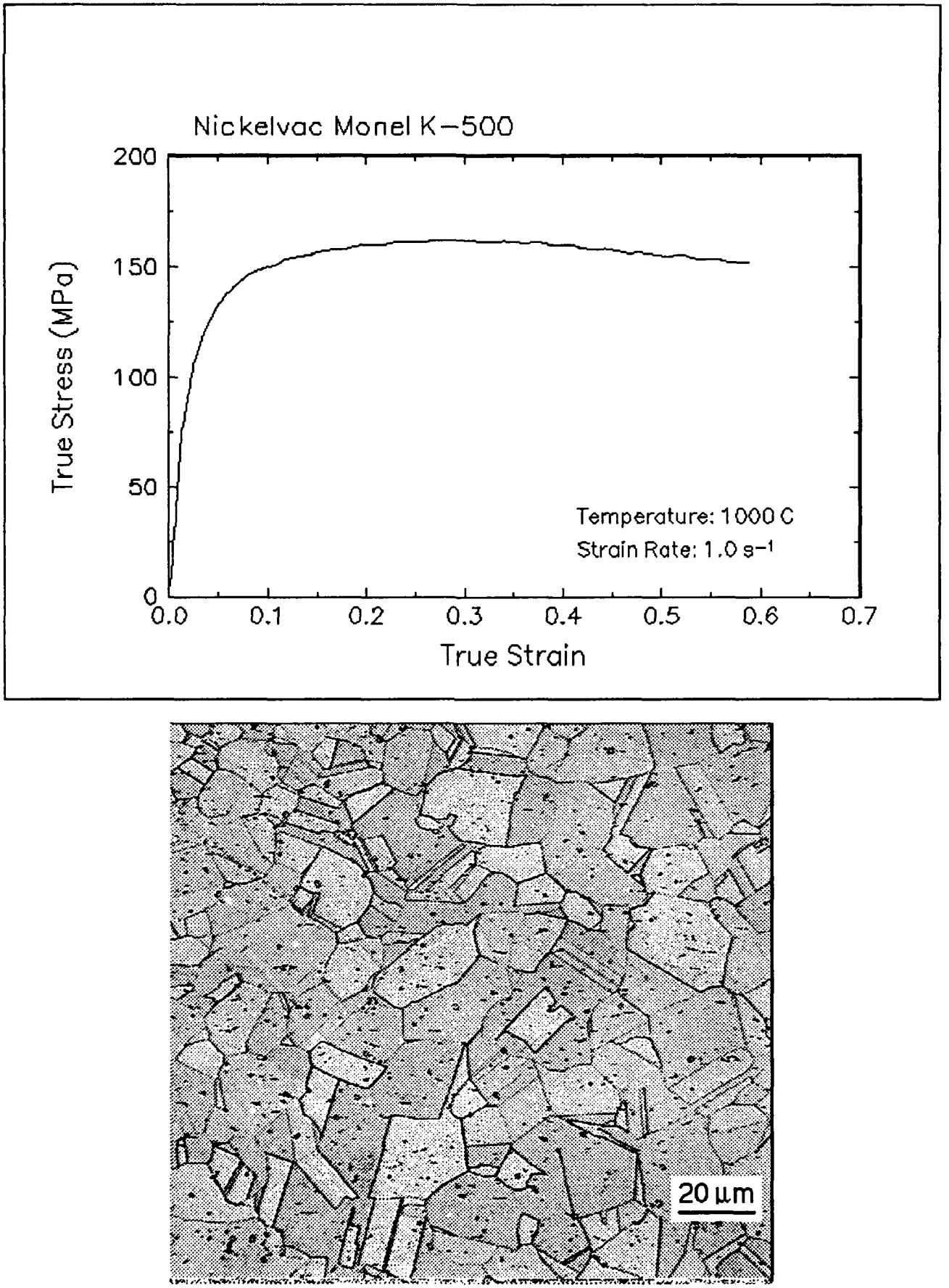

Figure 31. True stress-true strain curve and an optical micrograph from the center of the compressed sample cut through the compression axis, 1000 C and 1 s^{-1}.

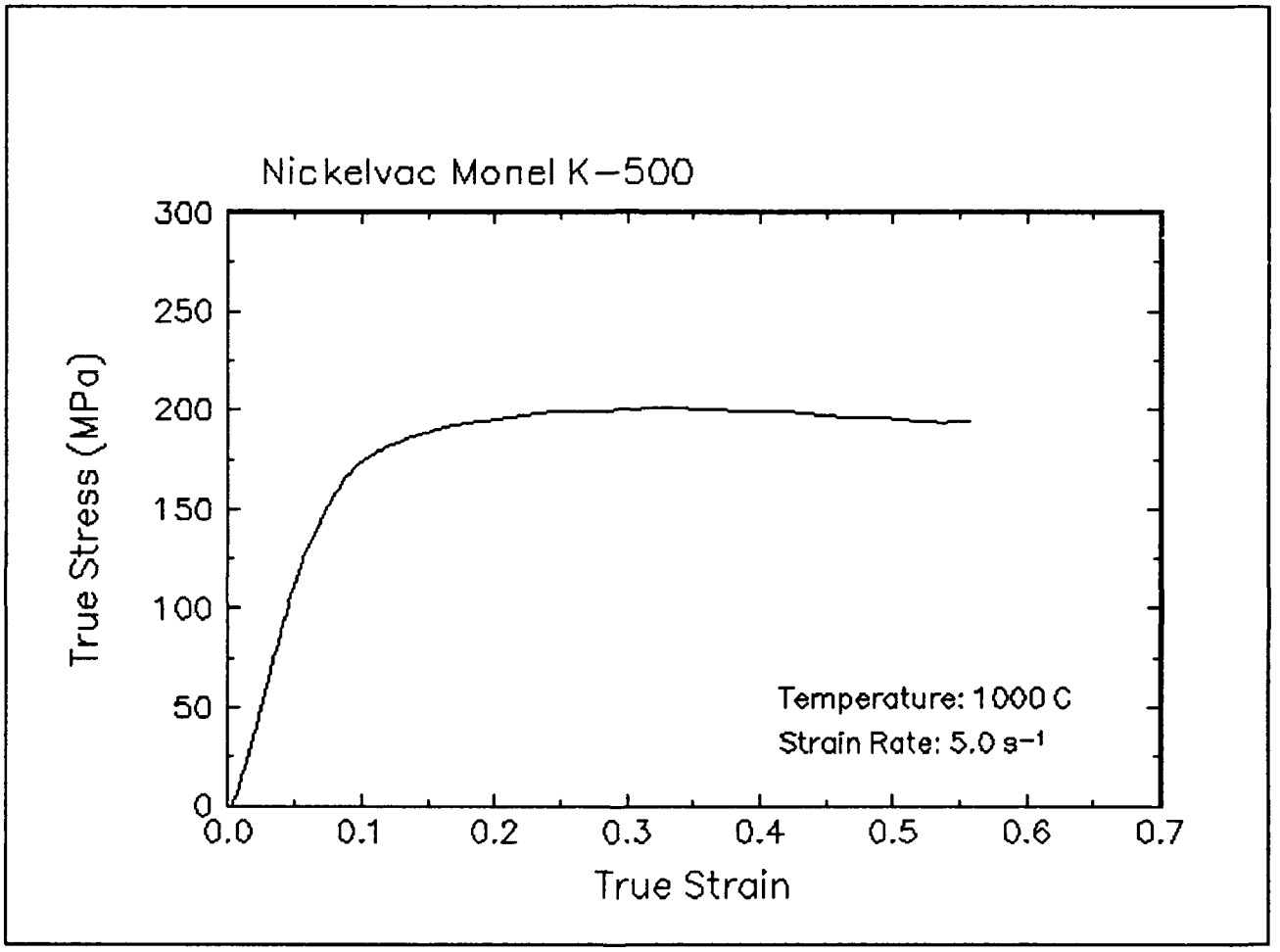

Figure 32. True stress-true strain curve, 1000 C and 5 s^{-1}.

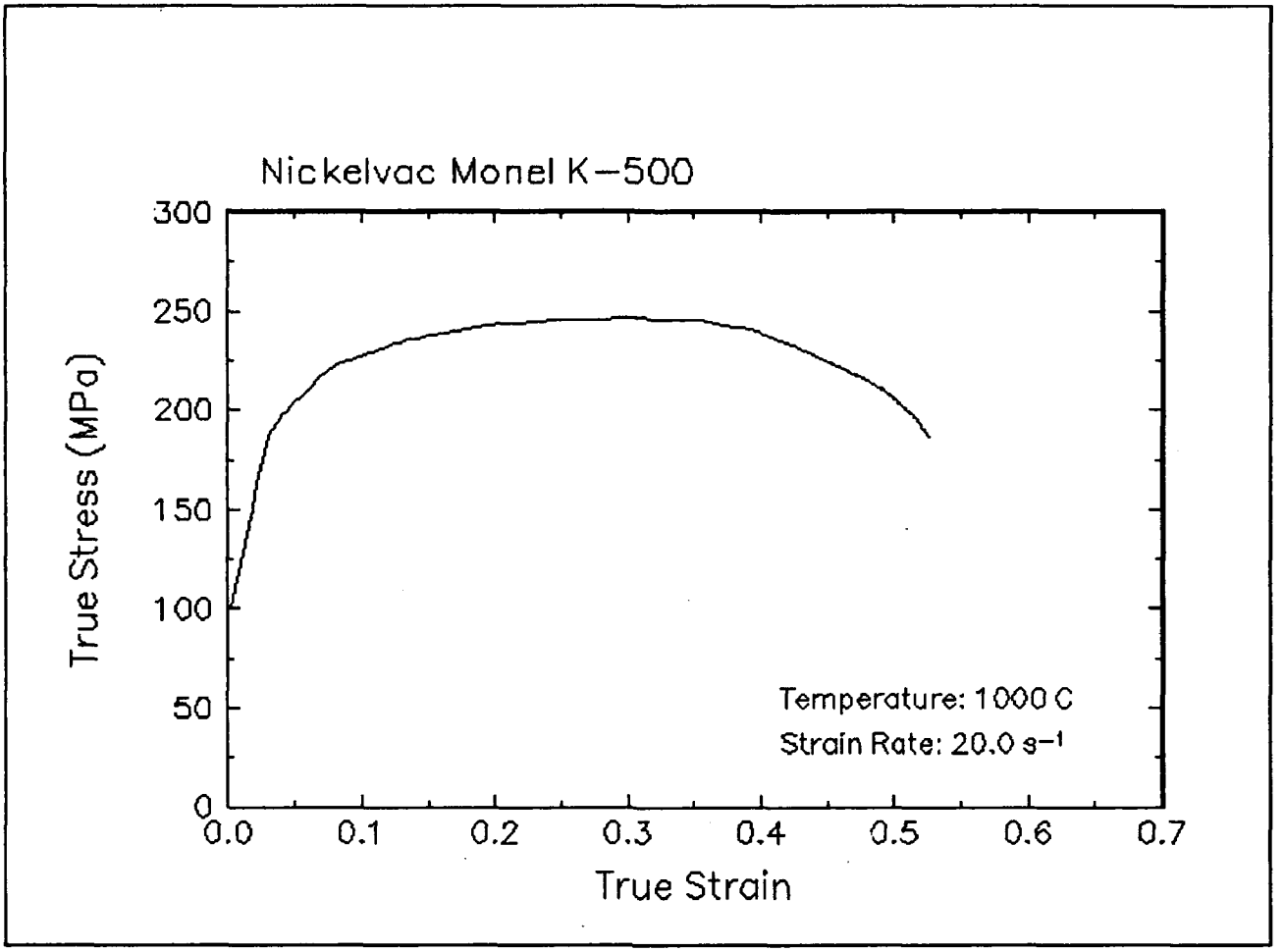

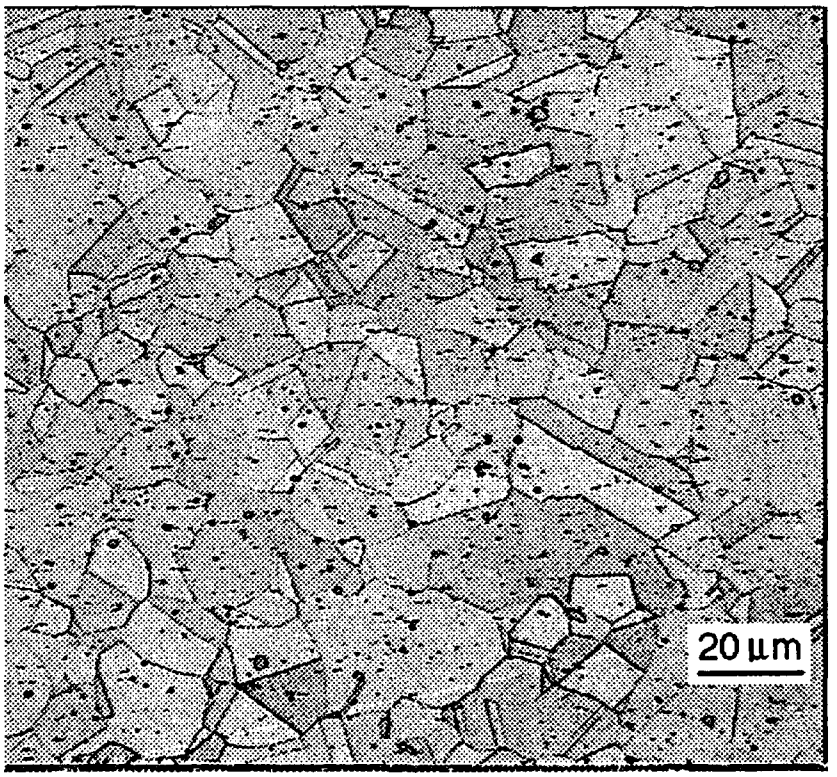

Figure 33. True stress-true strain curve and an optical micrograph from the center of the compressed sample cut through the compression axis, 1000 C and 20 s^{-1}.

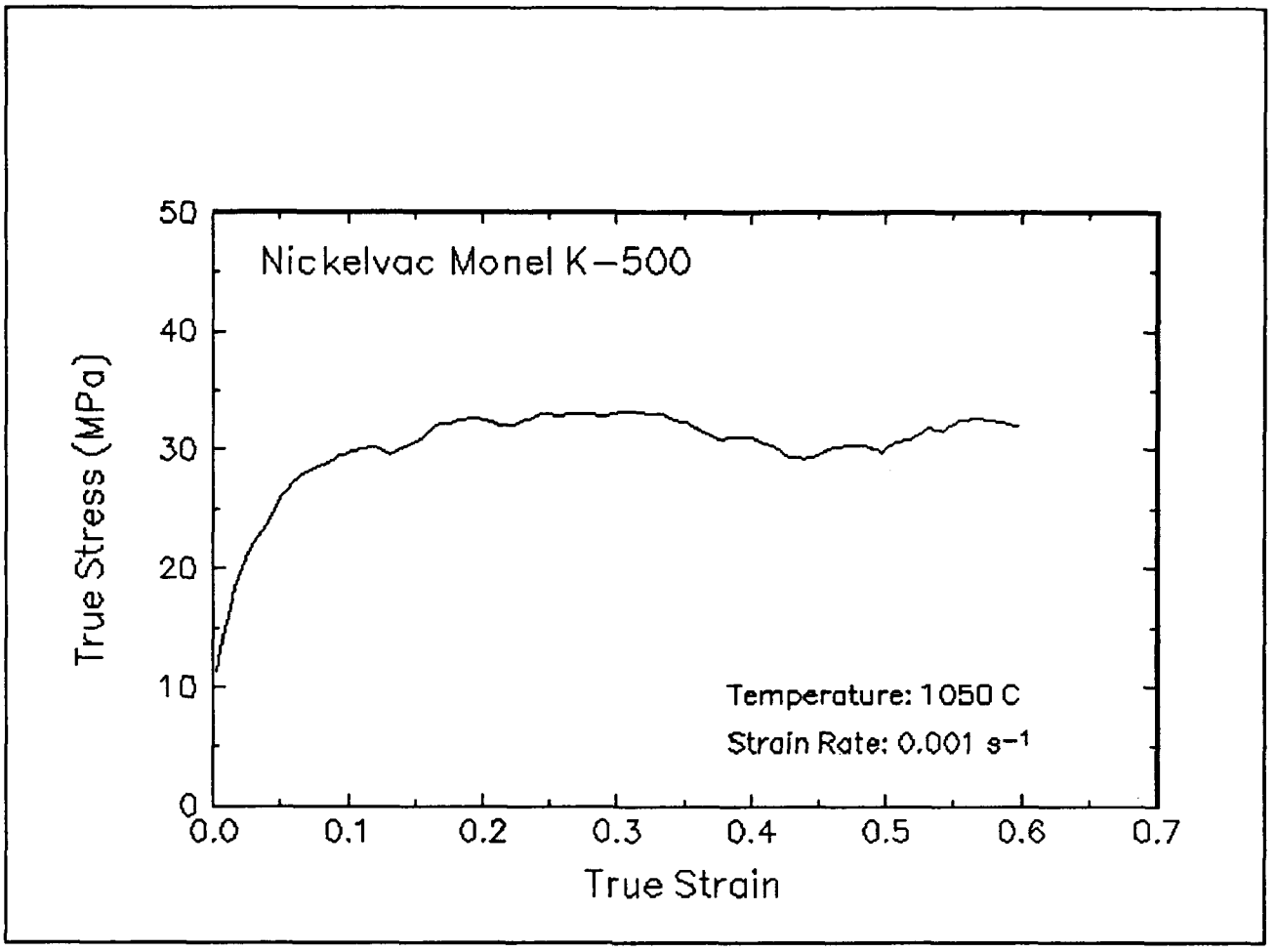

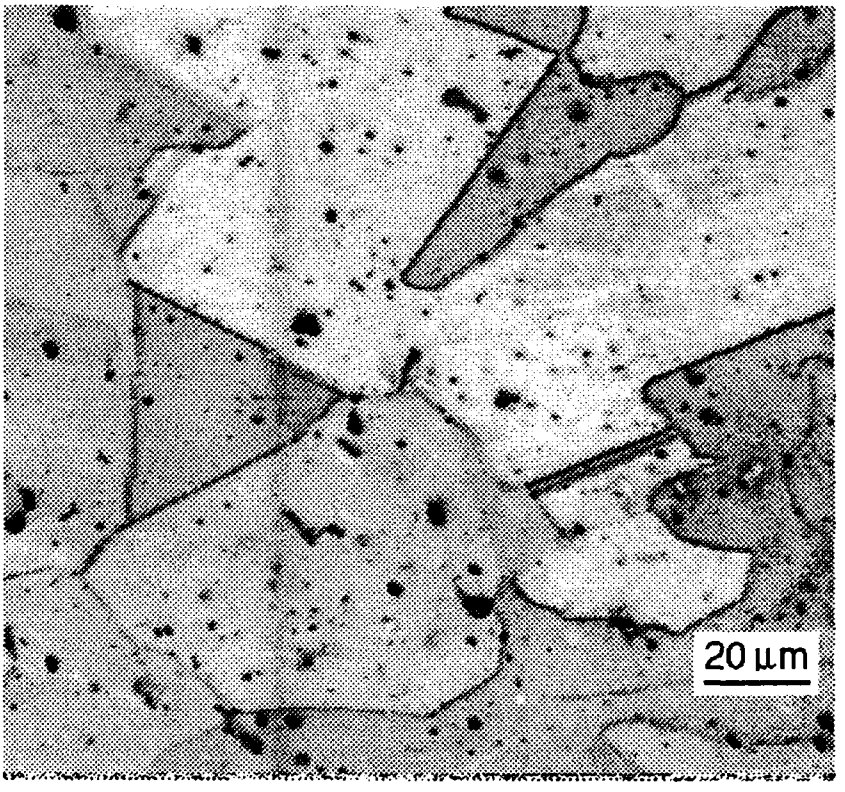

Figure 34. True stress-true strain curve and an optical micrograph from the center of the compressed sample cut through the compression axis, 1050 C and 0.001 s^{-1}.

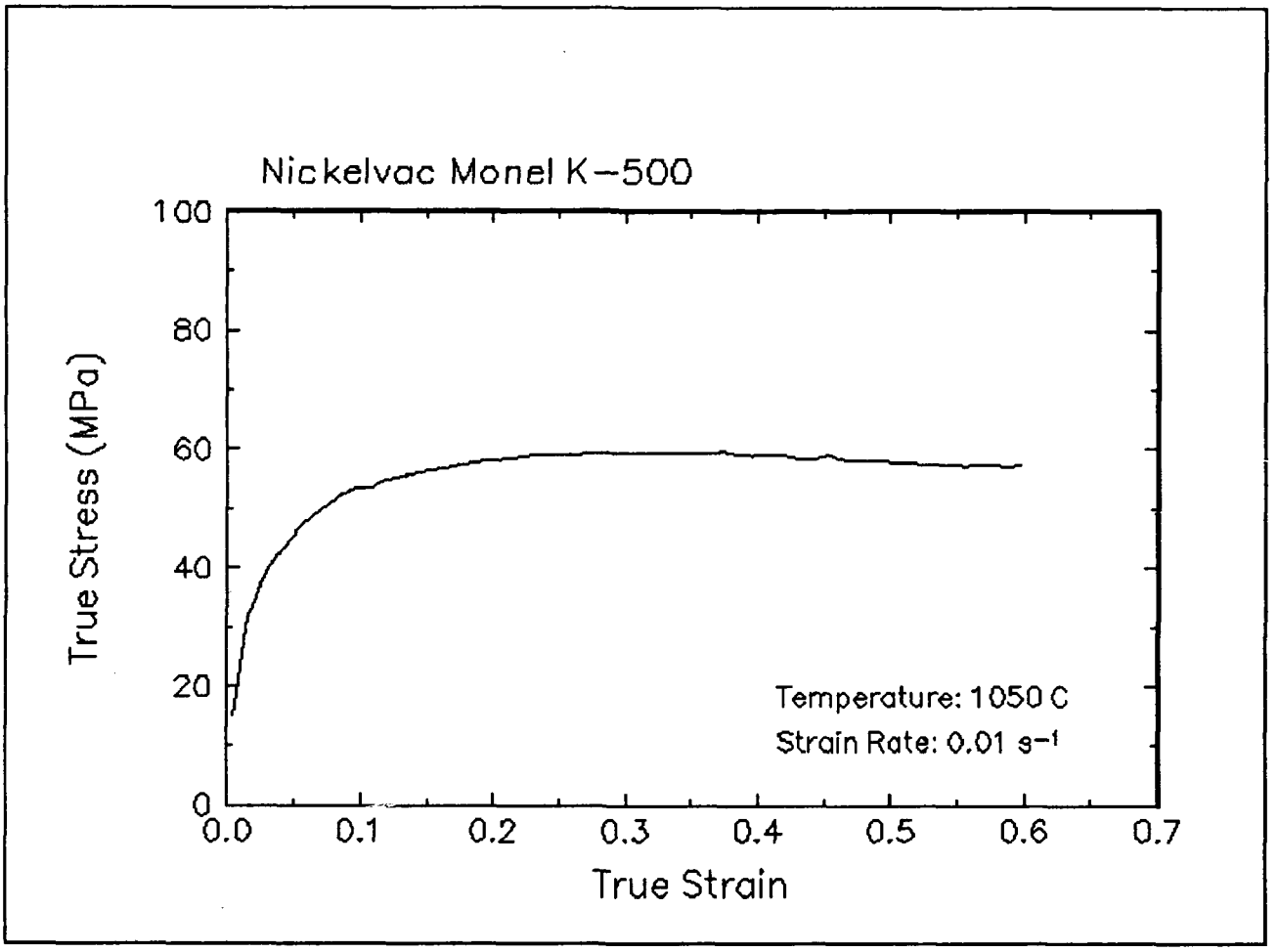

Figure 35. True stress-true strain curve, 1050 C and 0.01 s^{-1}.

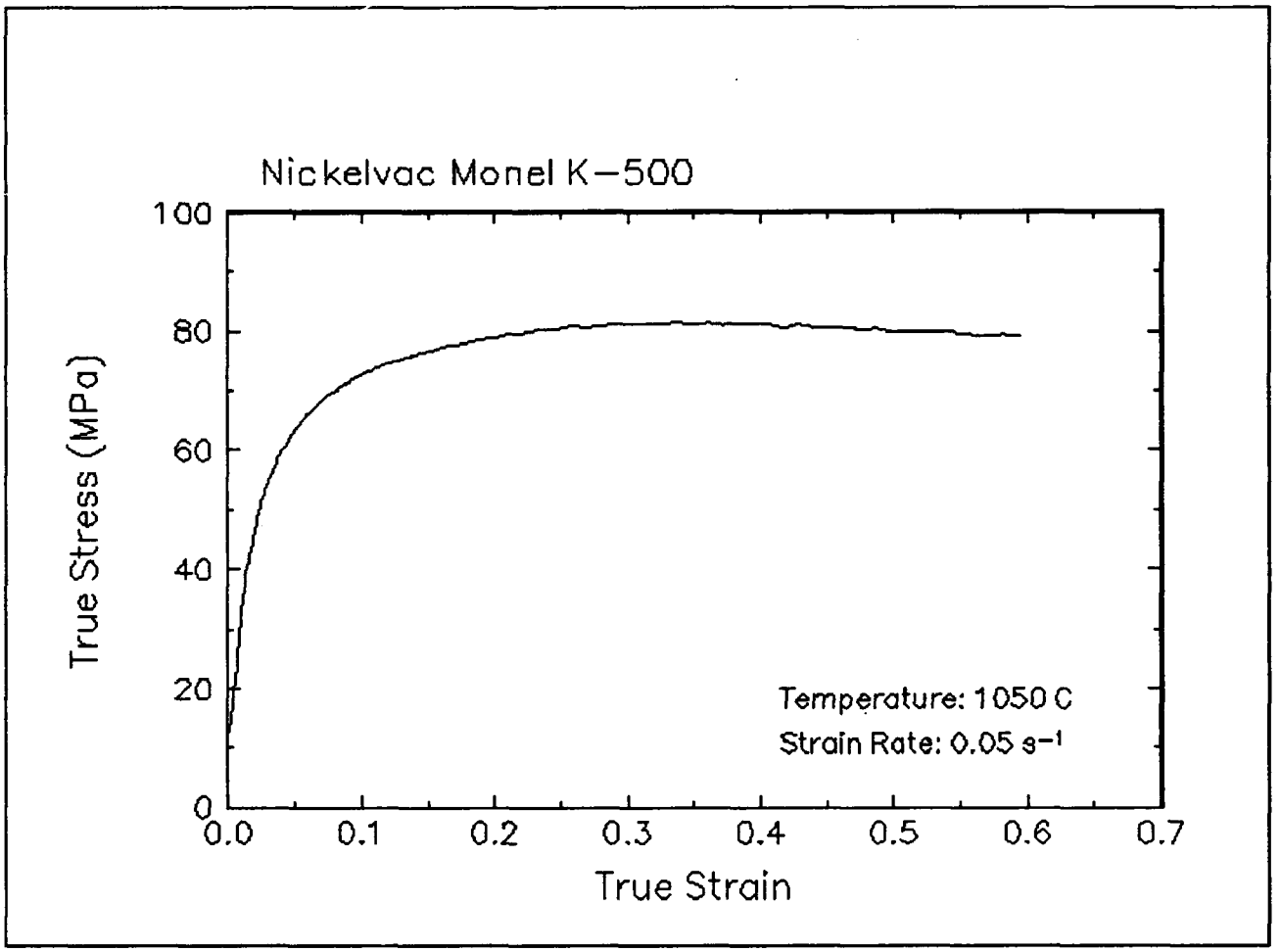

Figure 36. True stress-true strain curve, 1050 C and 0.05 s^{-1}.

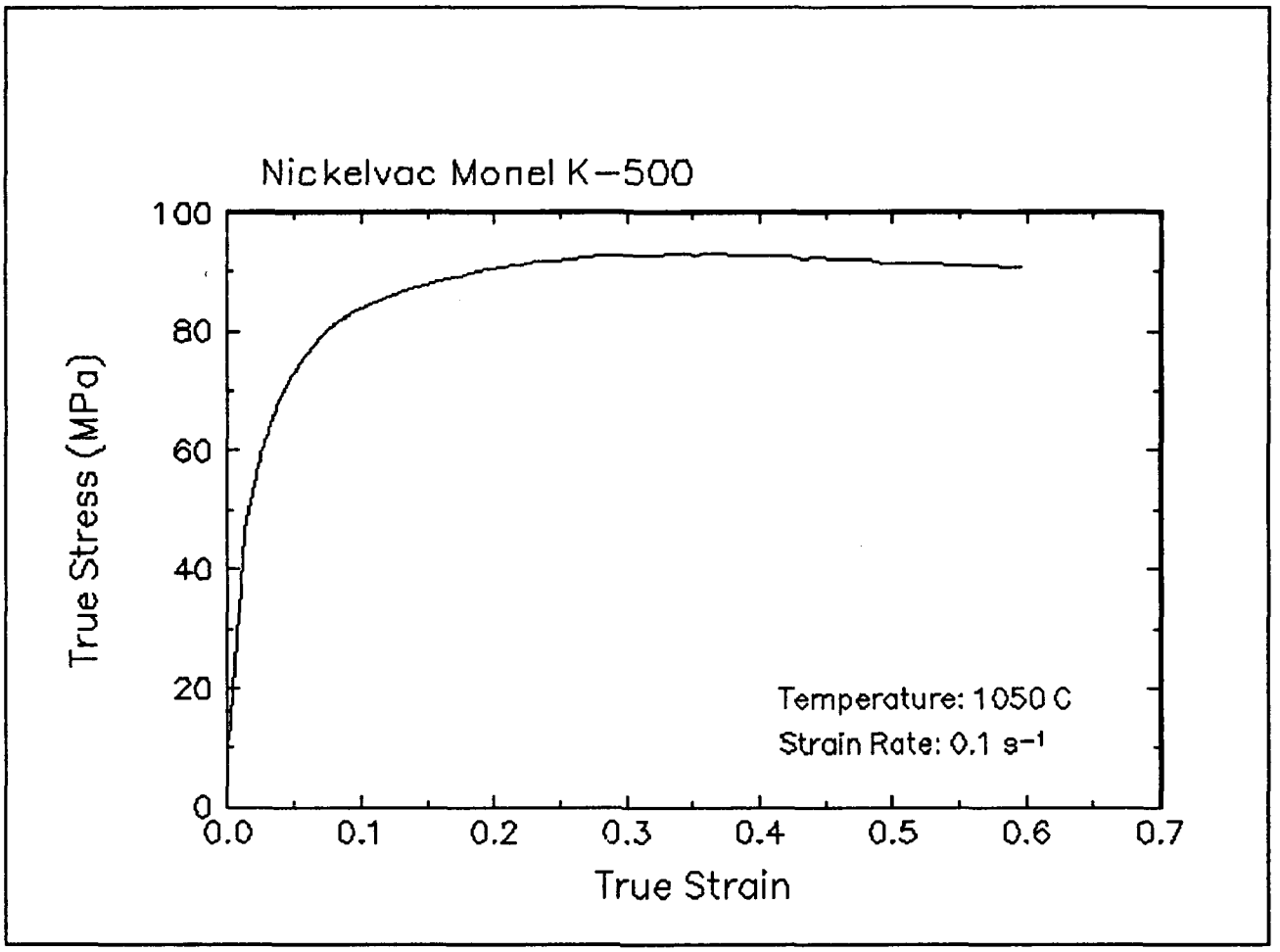

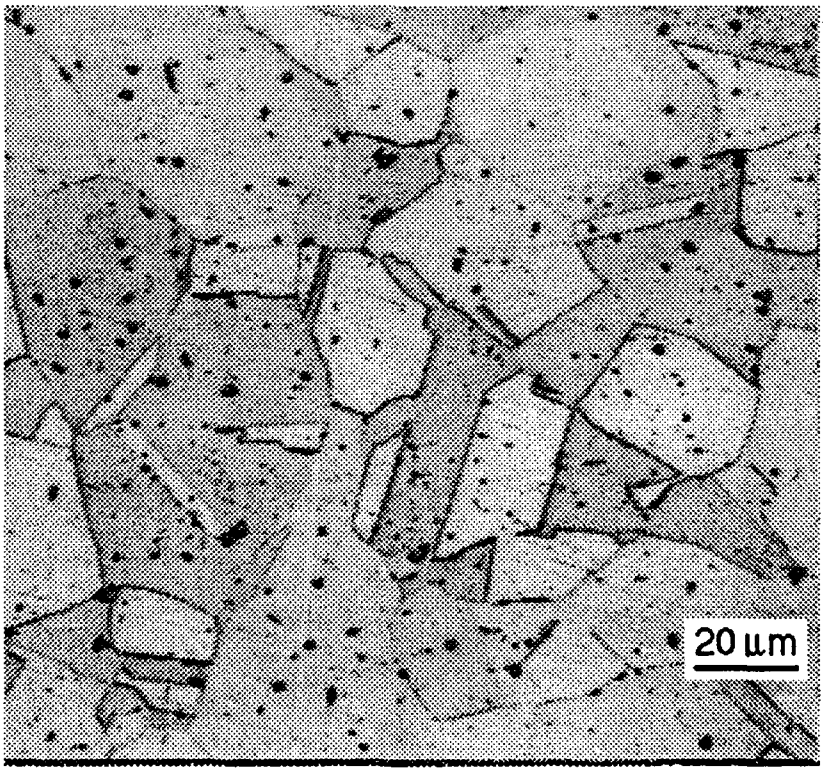

Figure 37. True stress-true strain curve and an optical micrograph from the center of the compressed sample cut through the compression axis, 1050 C and 0.1 s^{-1}.

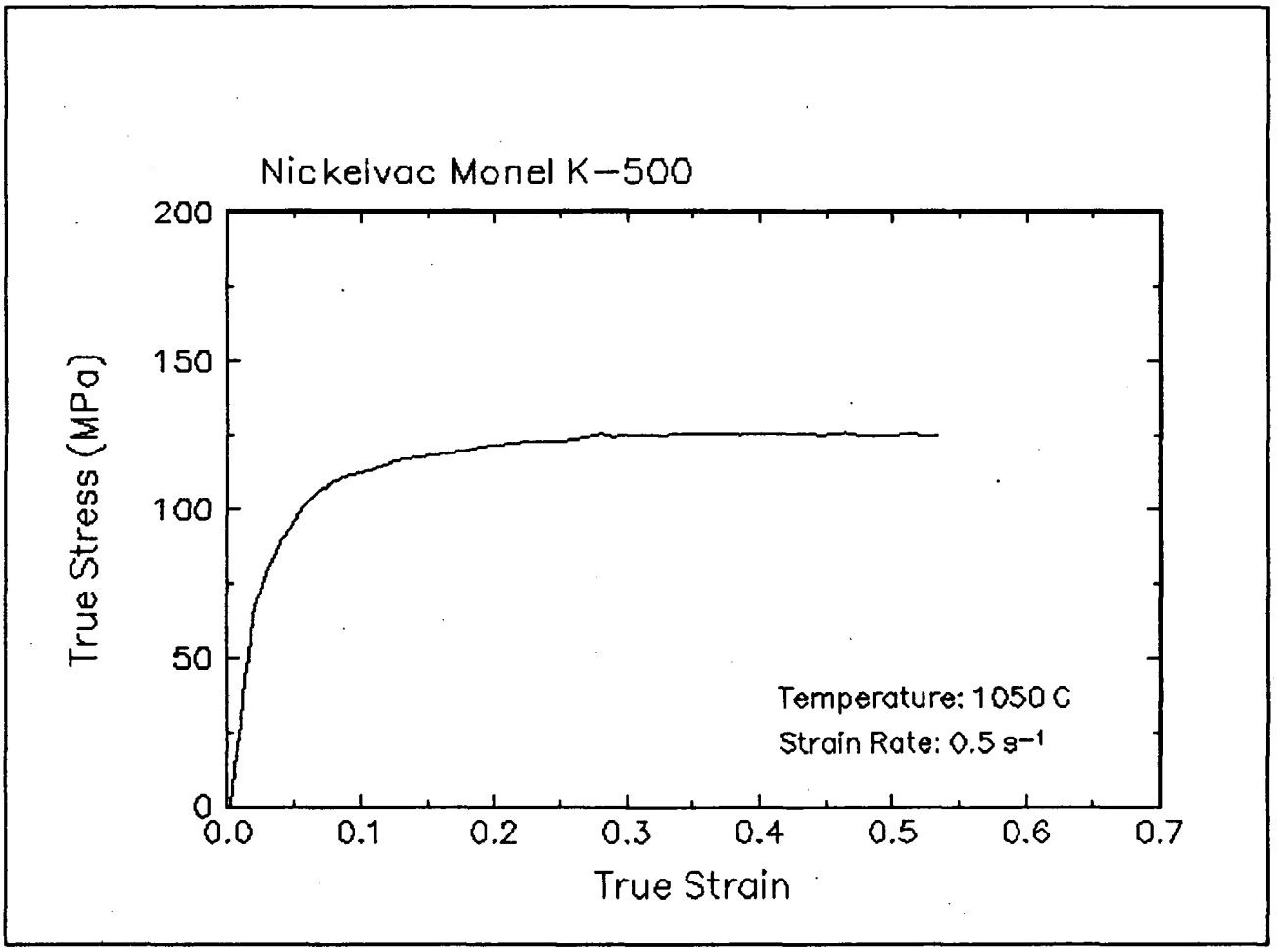

Figure 38. True stress-true strain curve, 1050 C and 0.5 s^{-1}.

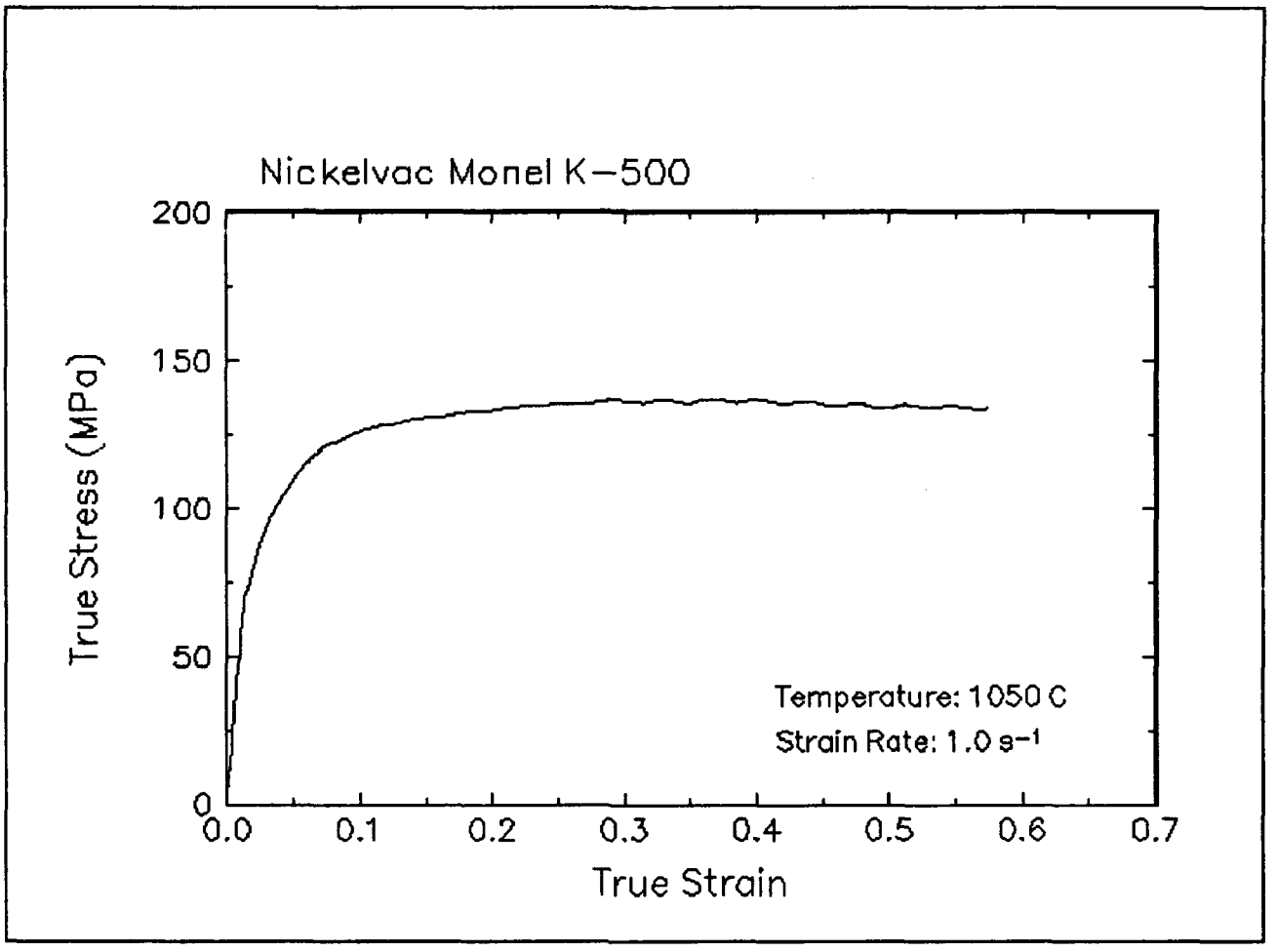

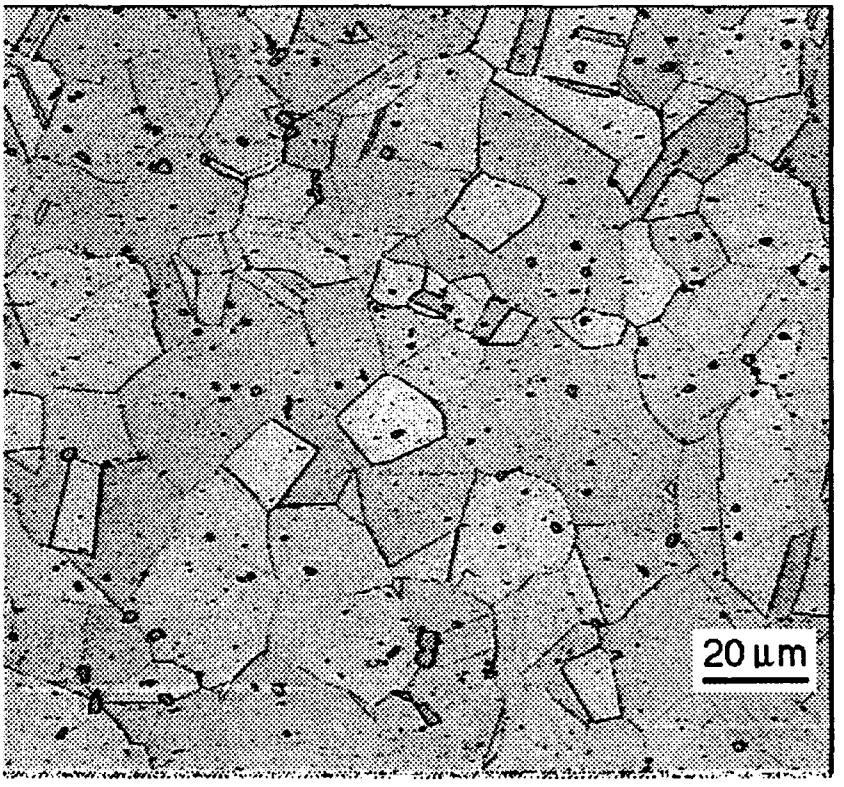

Figure 39. True stress-true strain curve and an optical micrograph from the center of the compressed sample cut through the compression axis, 1050 C and 1 s^{-1}.

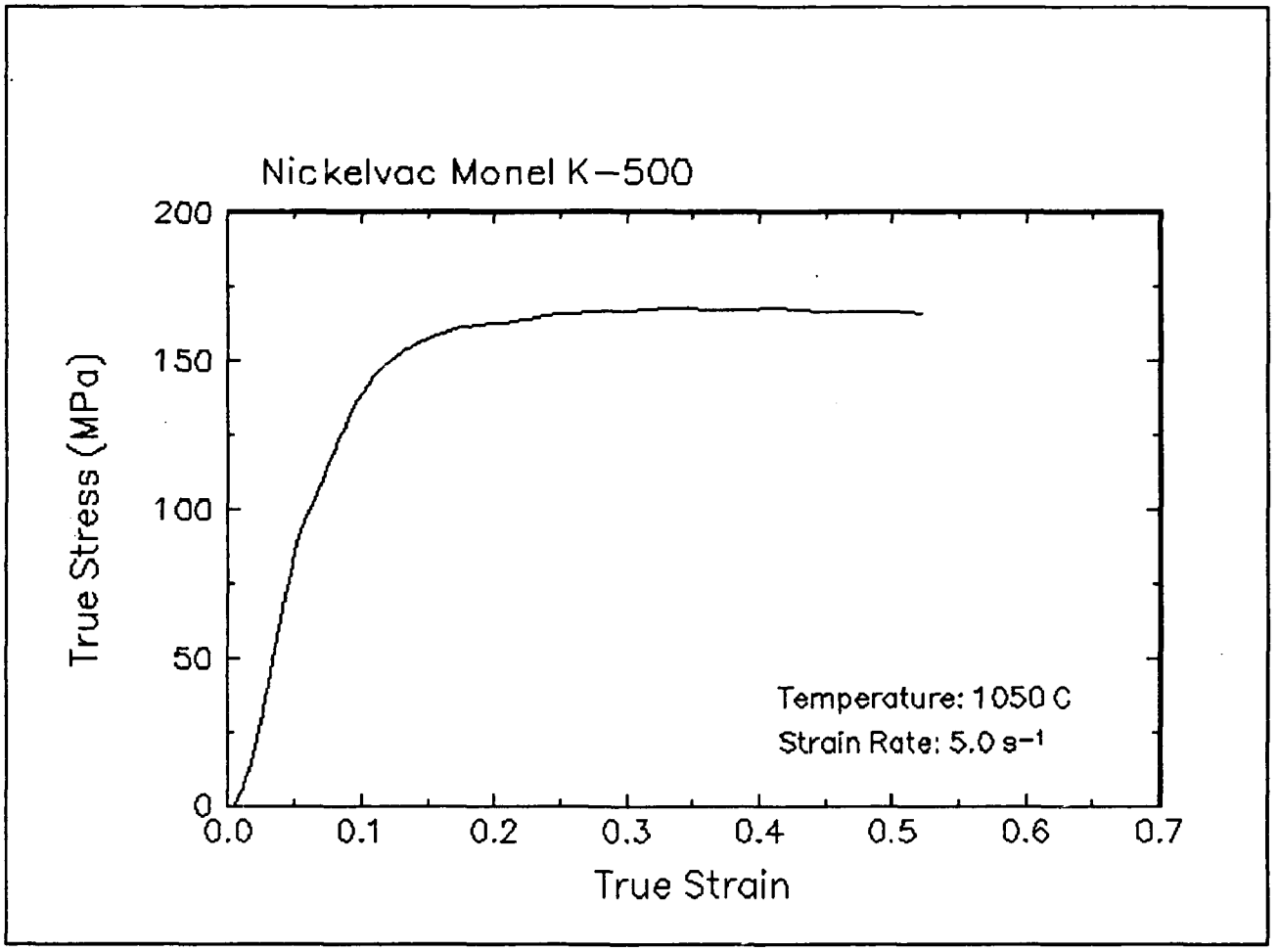

Figure 40. True stress-true strain curve, 1050 C and 5 s^{-1}.

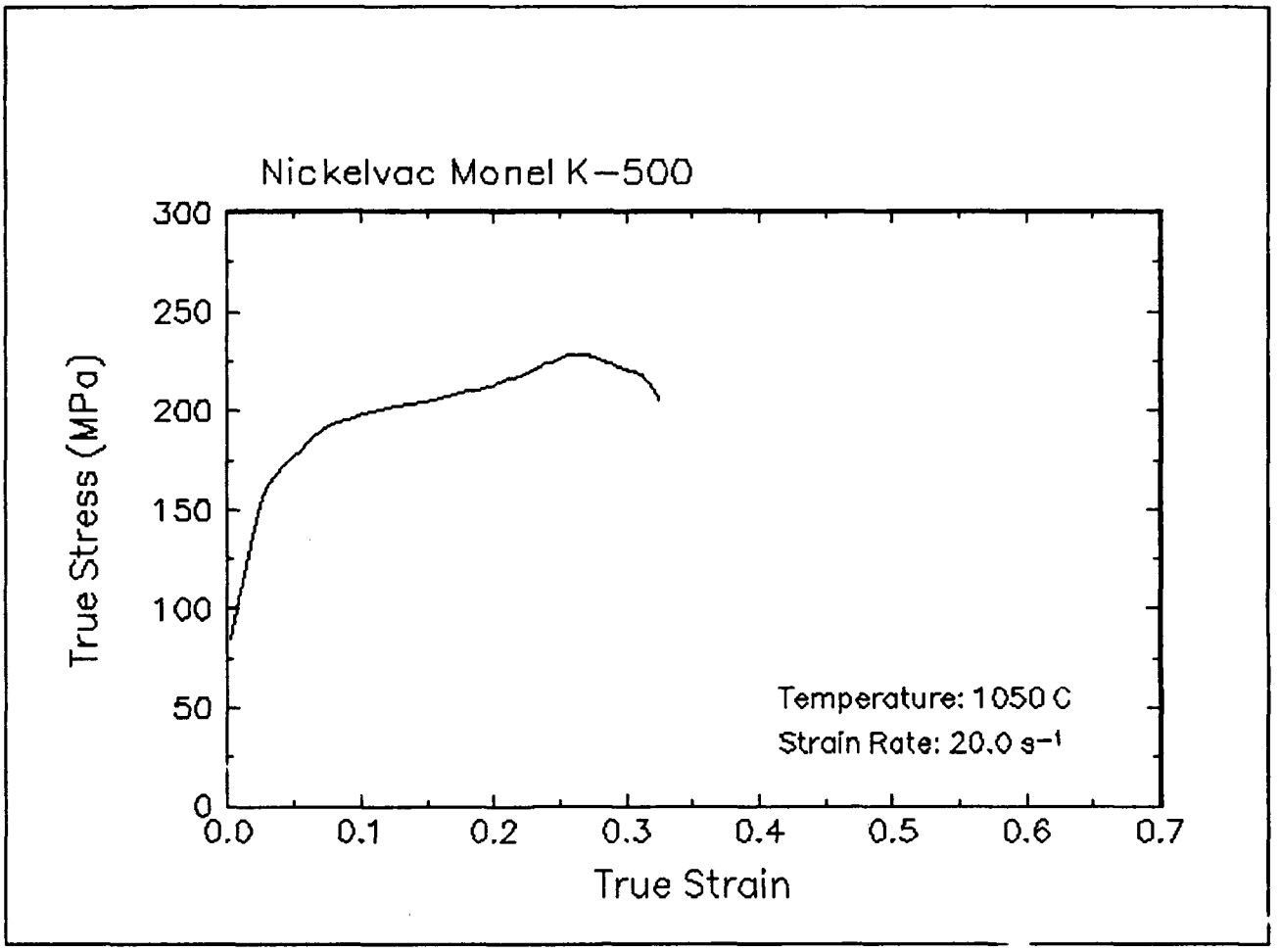

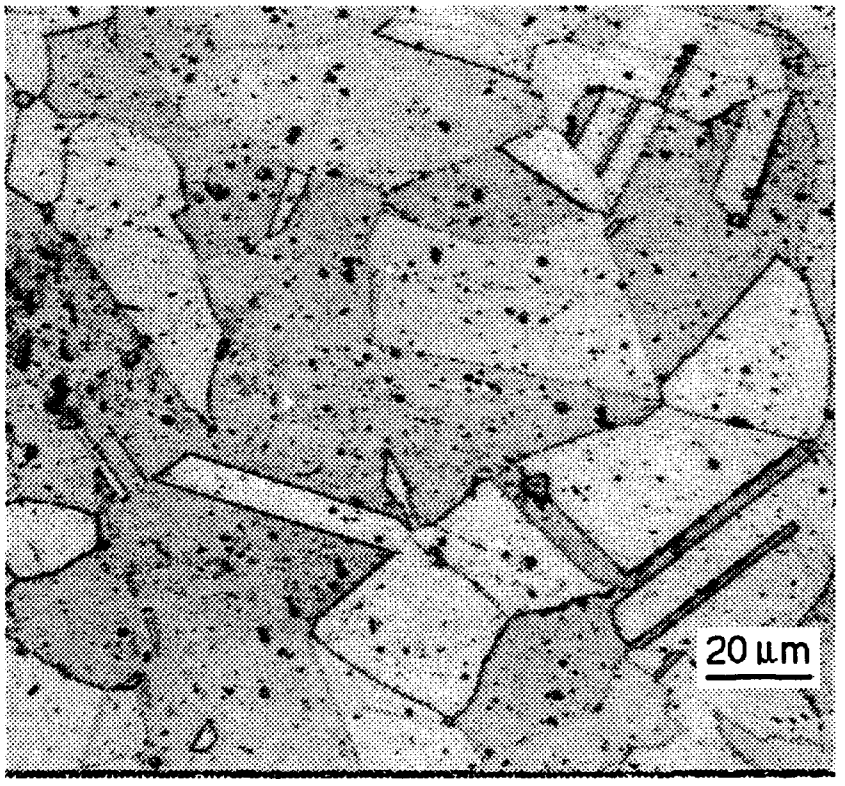

Figure 41. True stress-true strain curve and an optical micrograph from the center of the compressed sample cut through the compression axis, 1050 C and 20 s^{-1}.

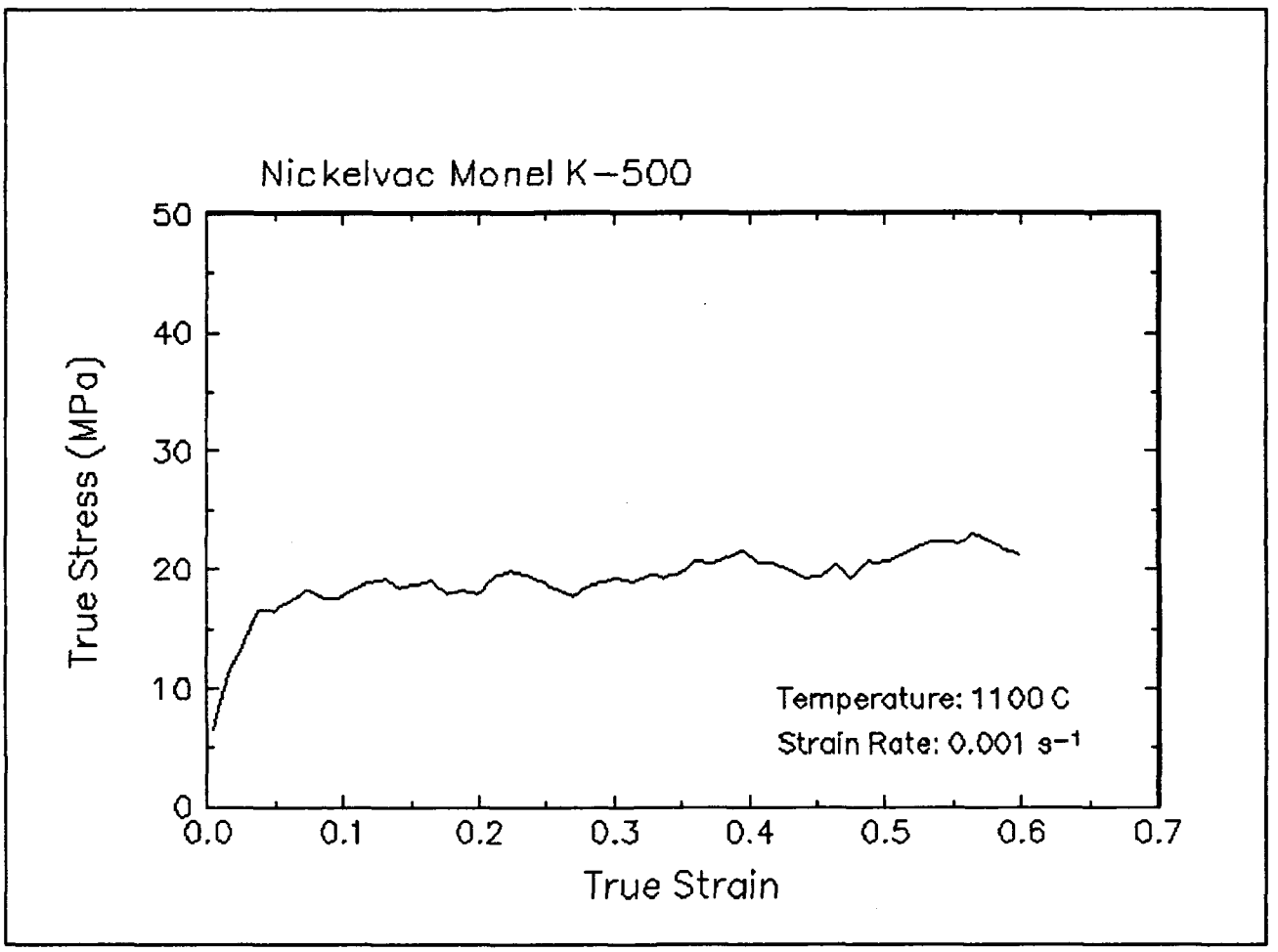

Figure 42. True stress-true strain curve, 1100 C and 0.001 s^{-1}.

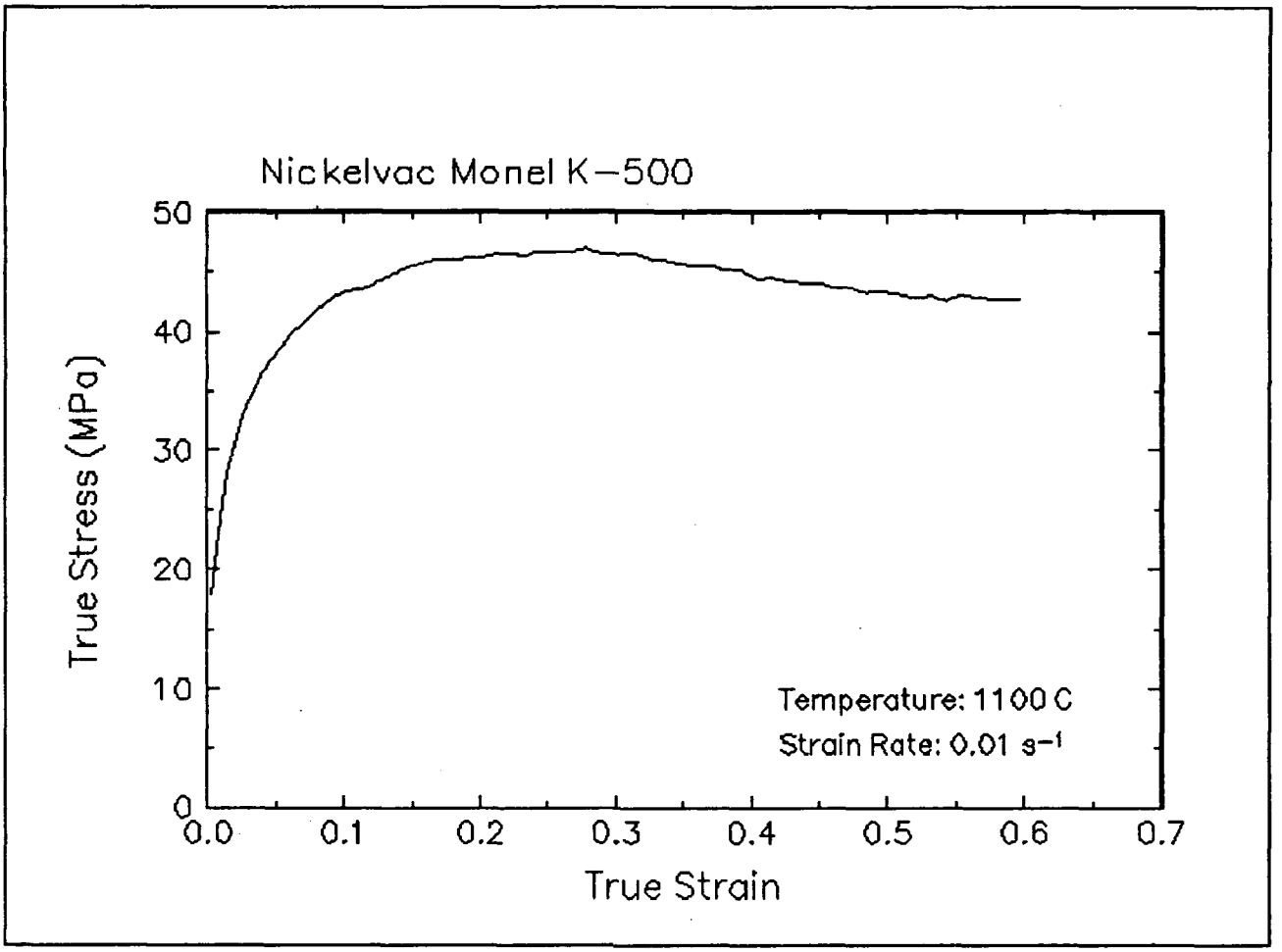

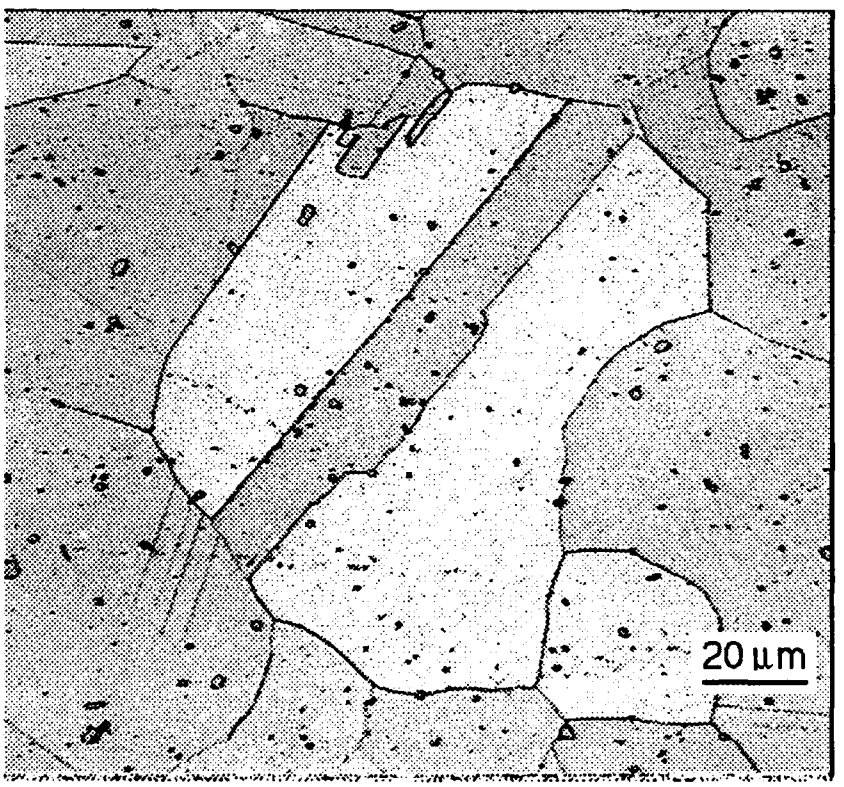

Figure 43. True stress-true strain curve and an optical micrograph from the center of the compressed sample cut through the compression axis, 1100 C and 0.01 s^{-1}.

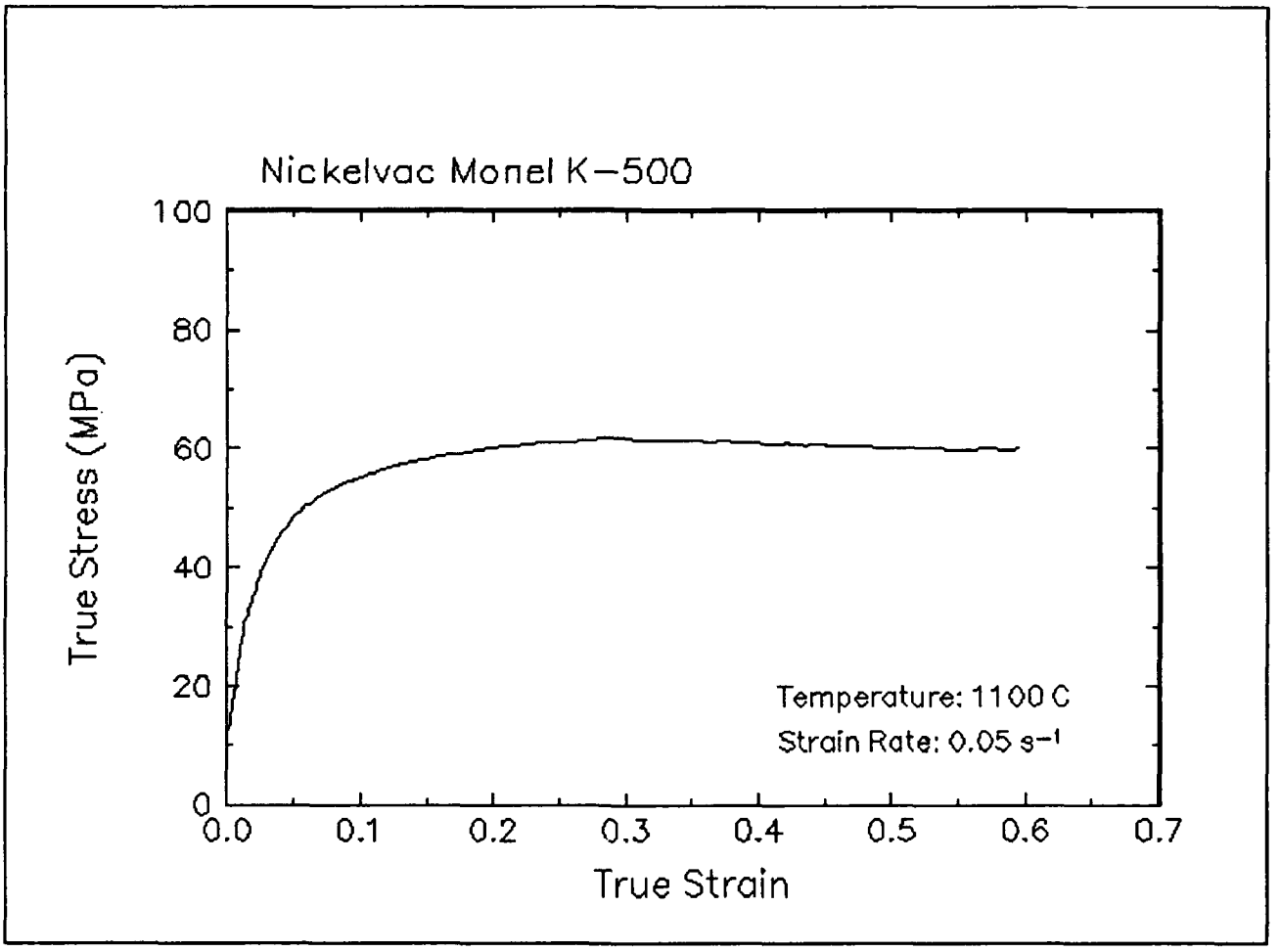

Figure 44. True stress-true strain curve, 1100 C and 0.05 s^{-1}.

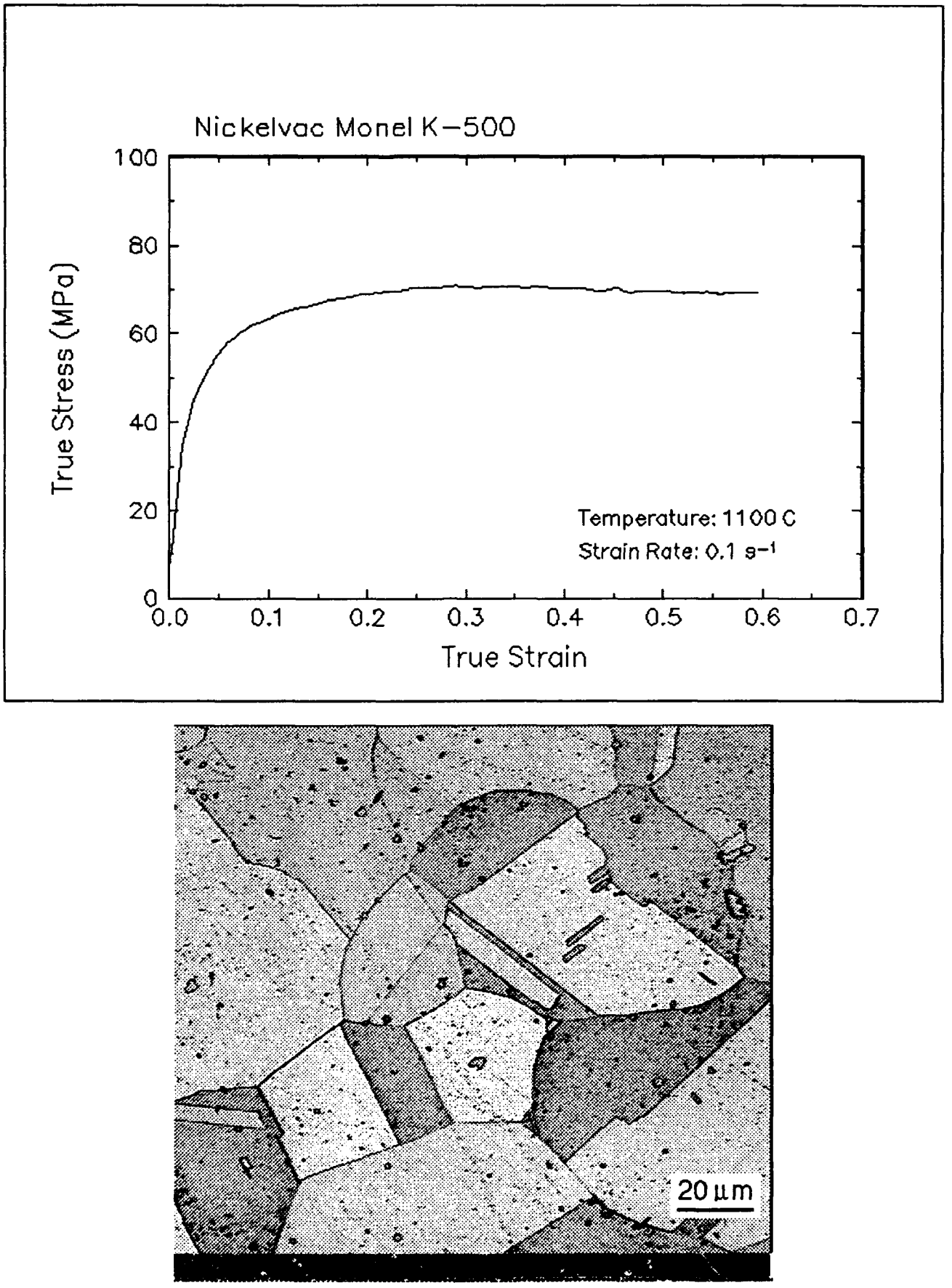

Figure 45. True stress-true strain curve and an optical micrograph from the center of the compressed sample cut through the compression axis, 1100 C and 0.1 s^{-1}.

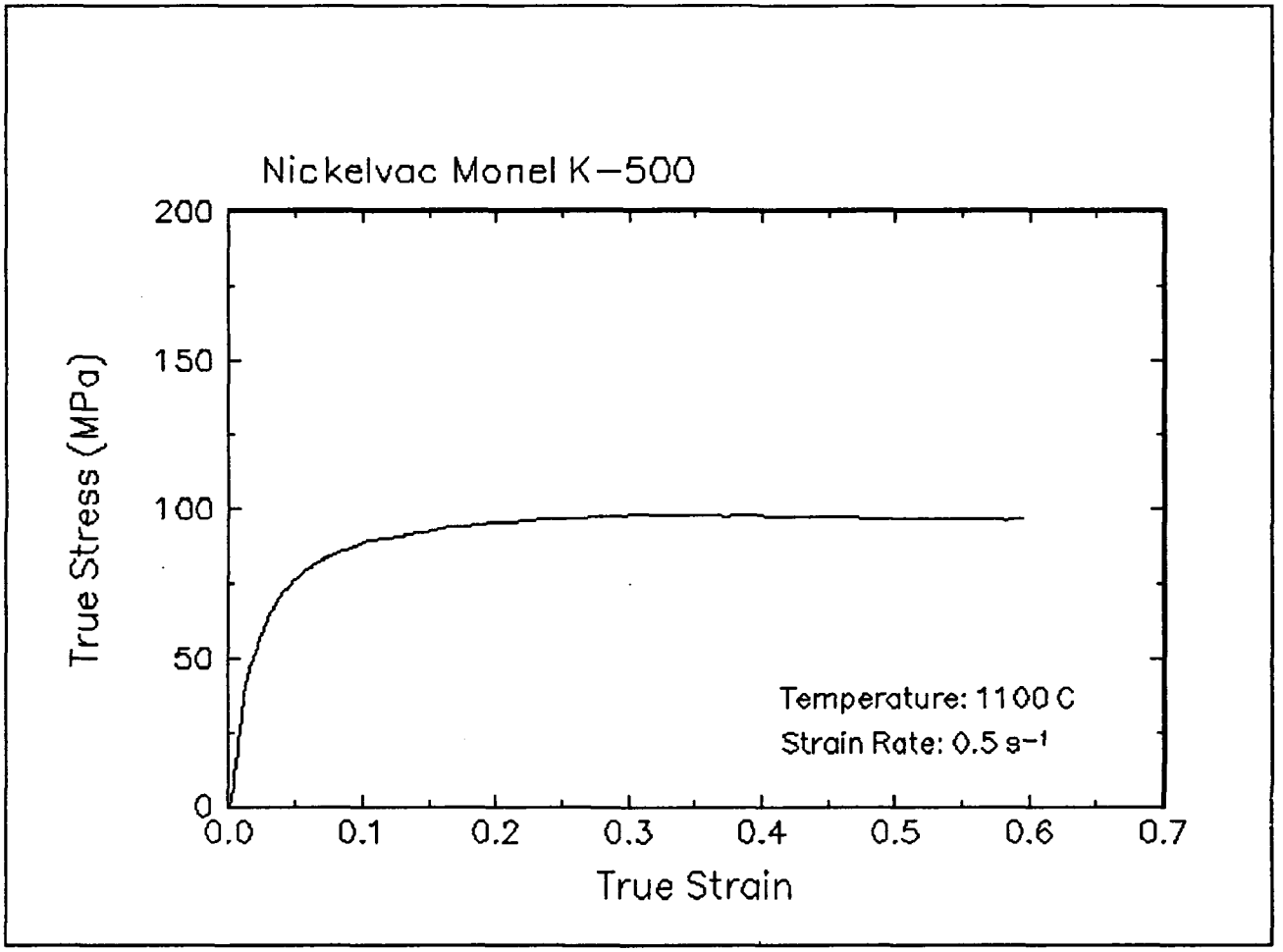

Figure 46. True stress-true strain curve, 1100 C and 0.5 s^{-1}.

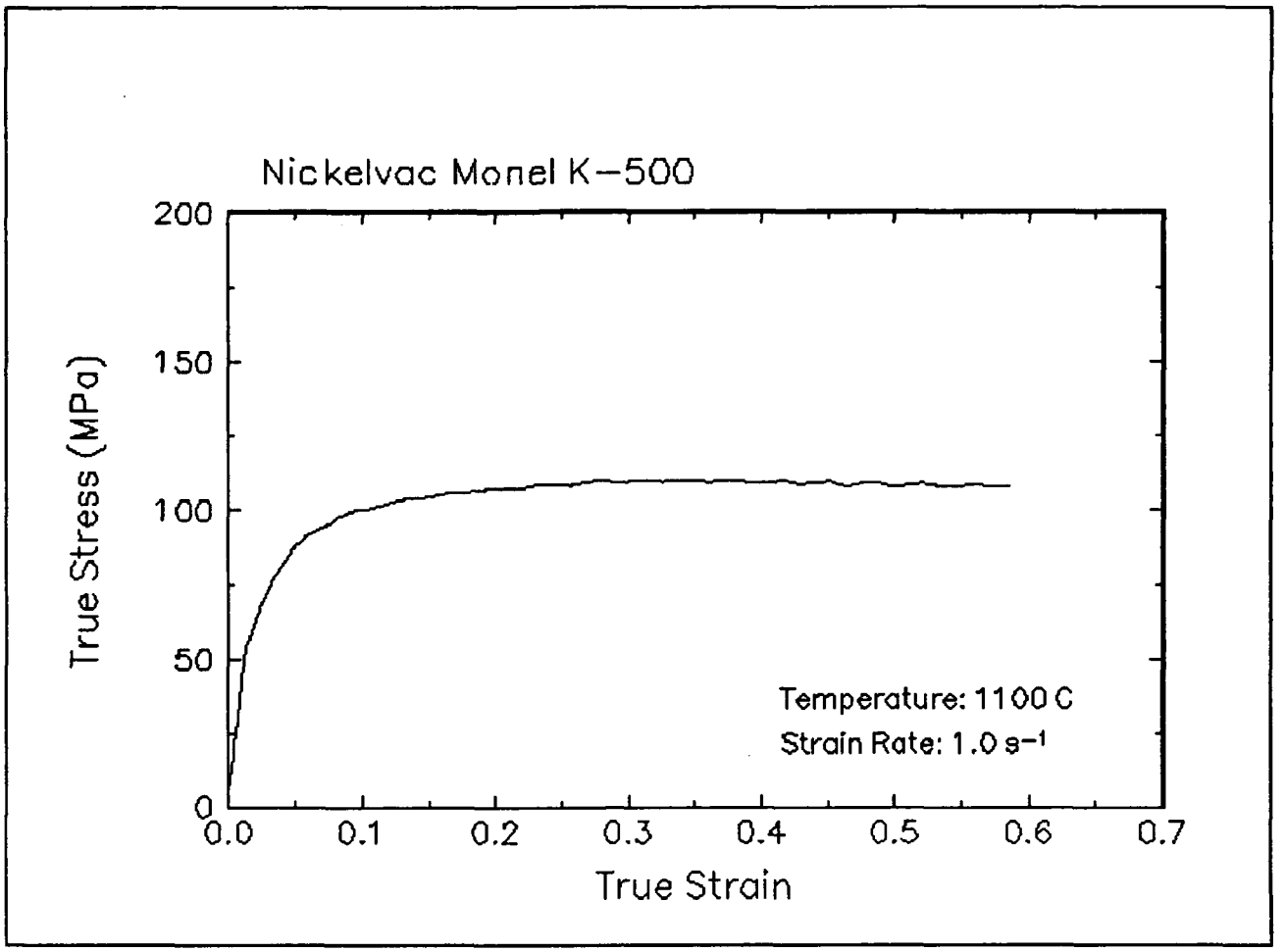

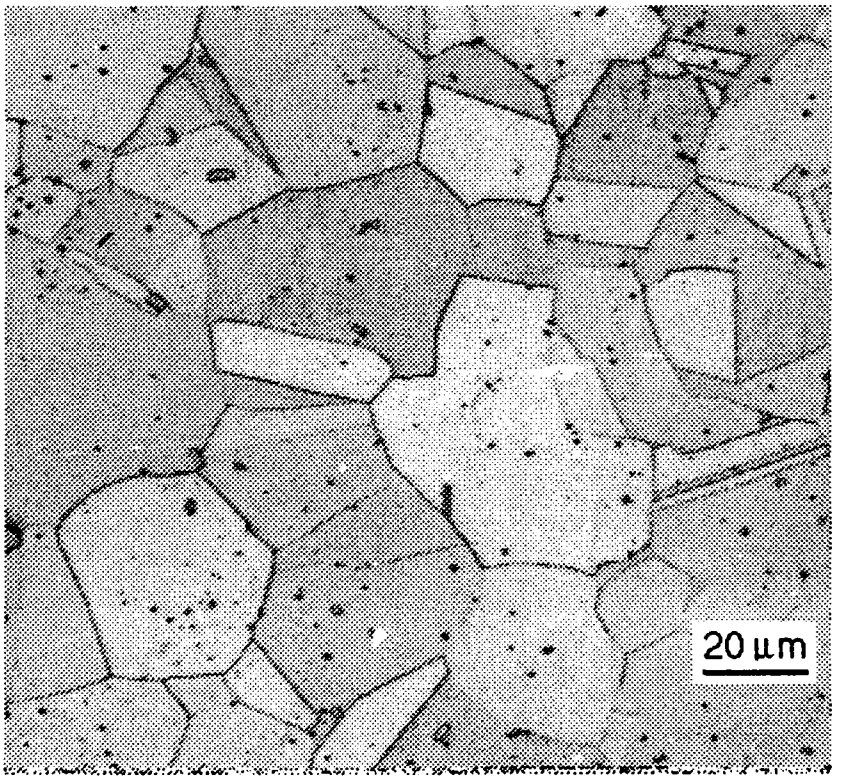

Figure 47. True stress-true strain curve and an optical micrograph from the center of the compressed sample cut through the compression axis, 1100 C and 1 s^{-1}.

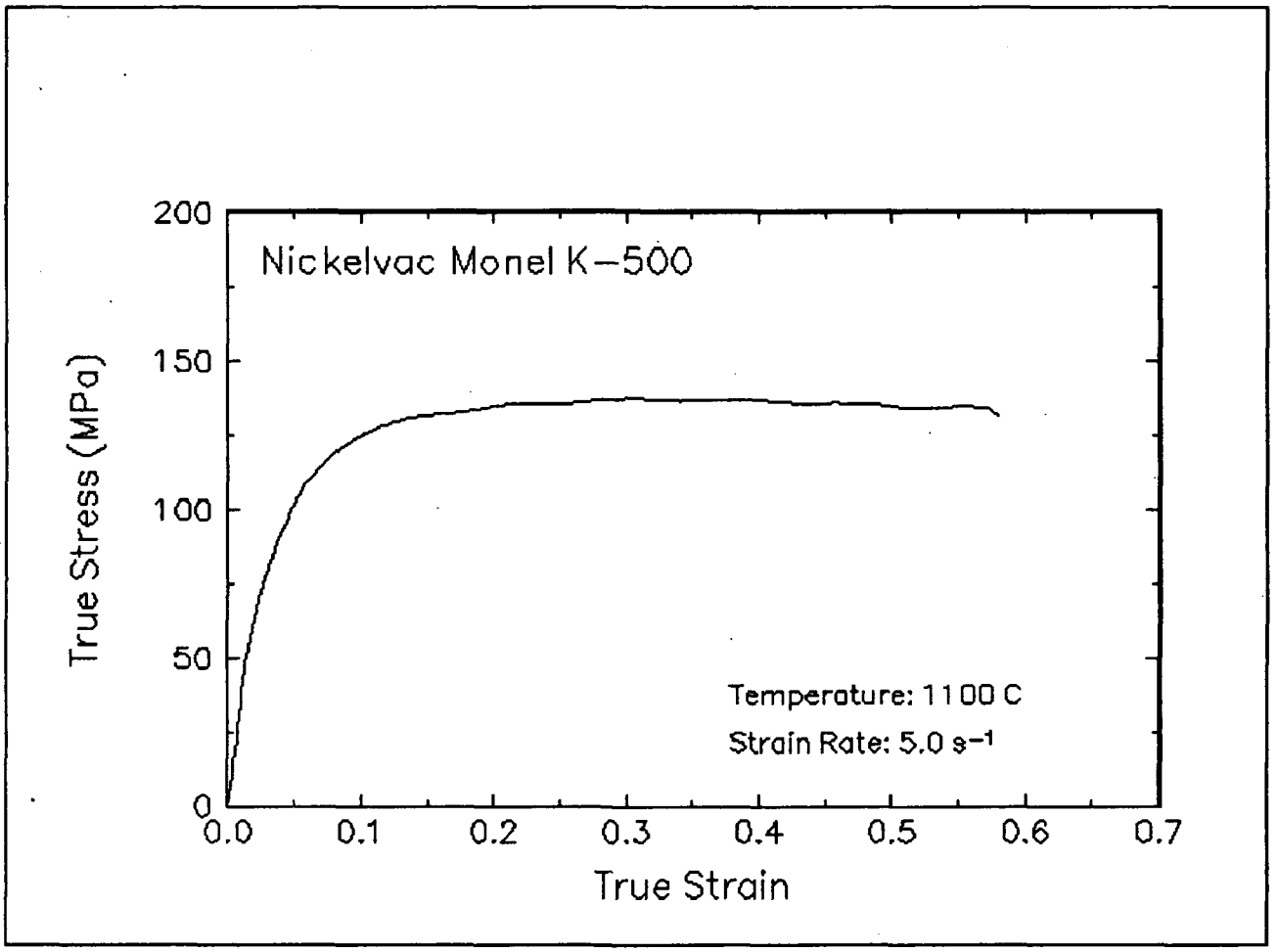

Figure 48. True stress-true strain curve, 1100 C and 5 s^{-1}.

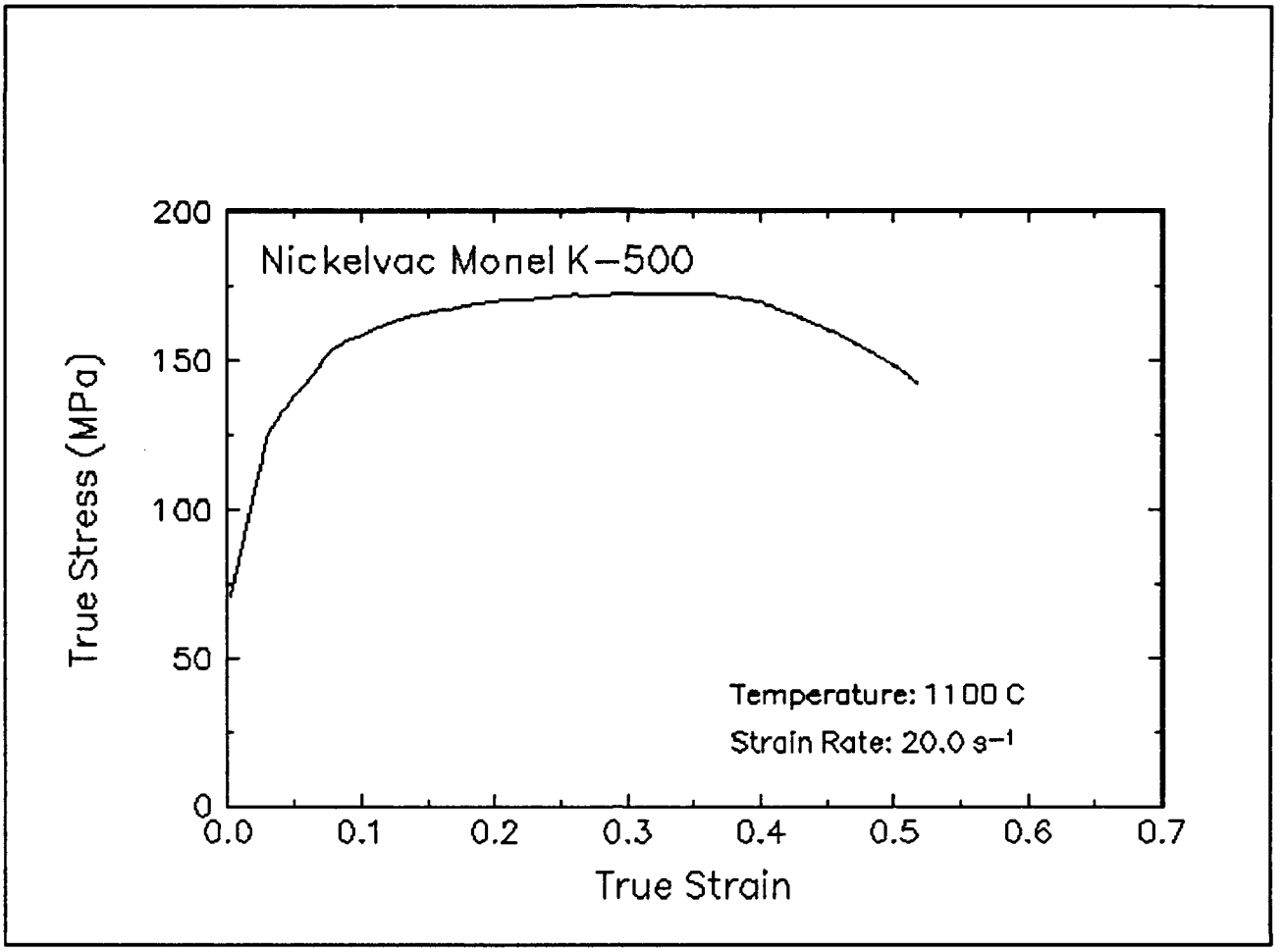

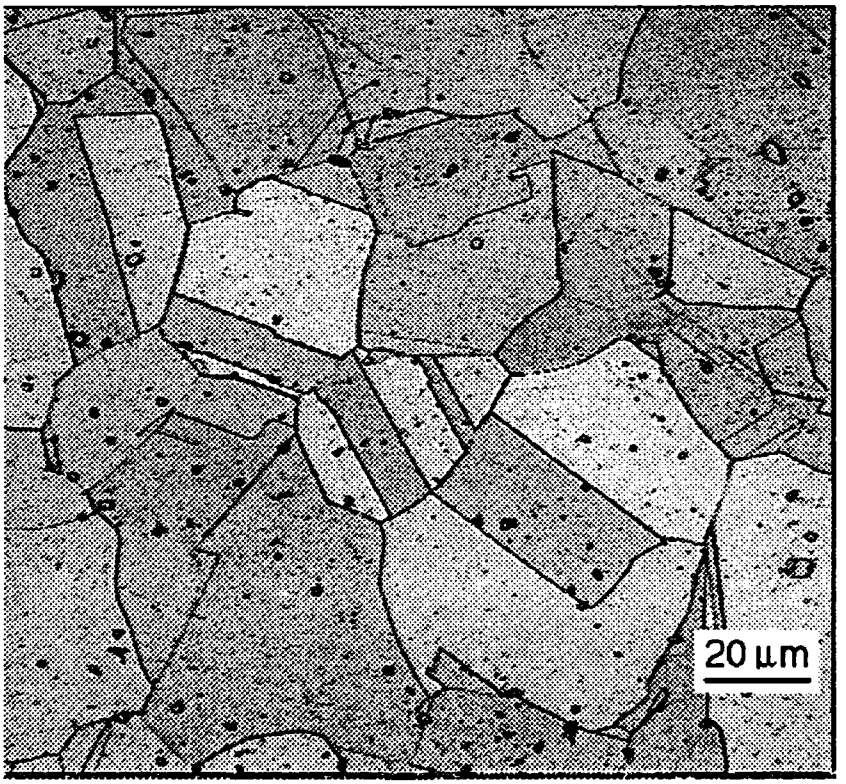

Figure 49. True stress-true strain curve and an optical micrograph from the center of the compressed sample cut through the compression axis, *1100 C* and 20 s^{-1}.

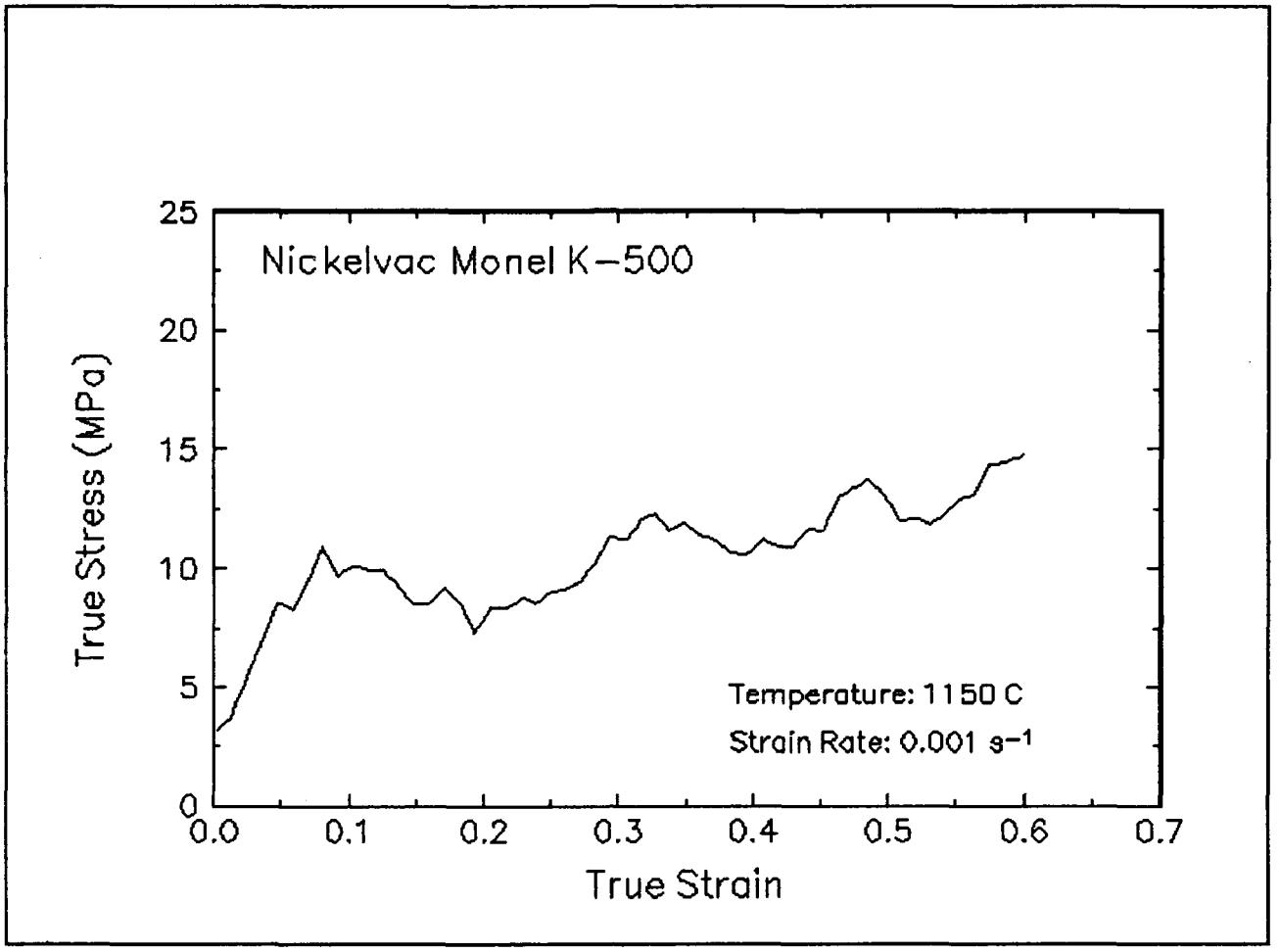

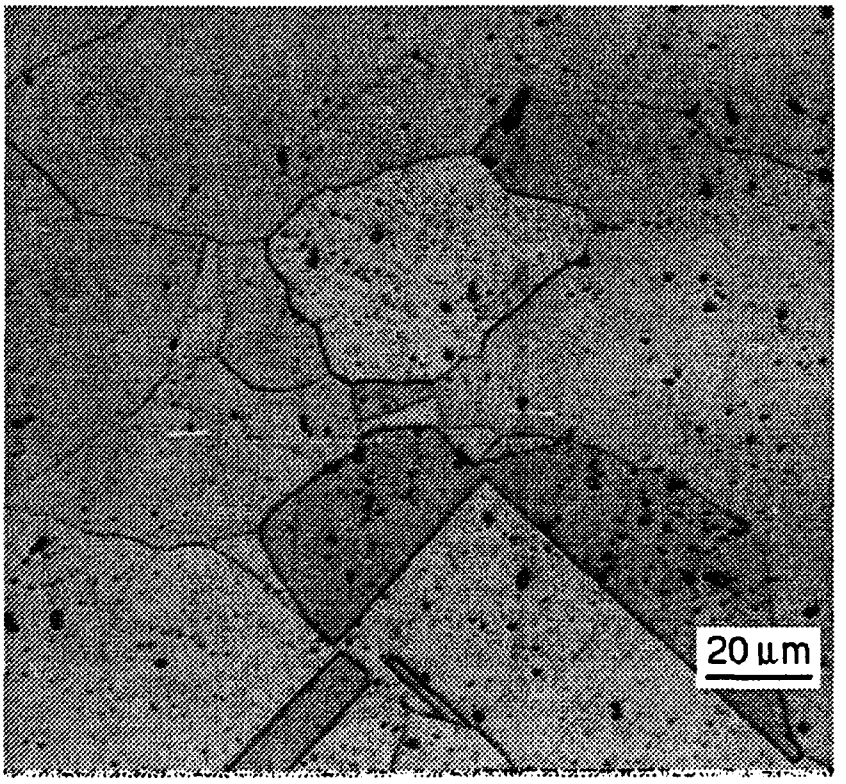

Figure 50. True stress-true strain curve and an optical micrograph from the center of the compressed sample cut through the compression axis, 1150 C and 0.001 s^{-1}.

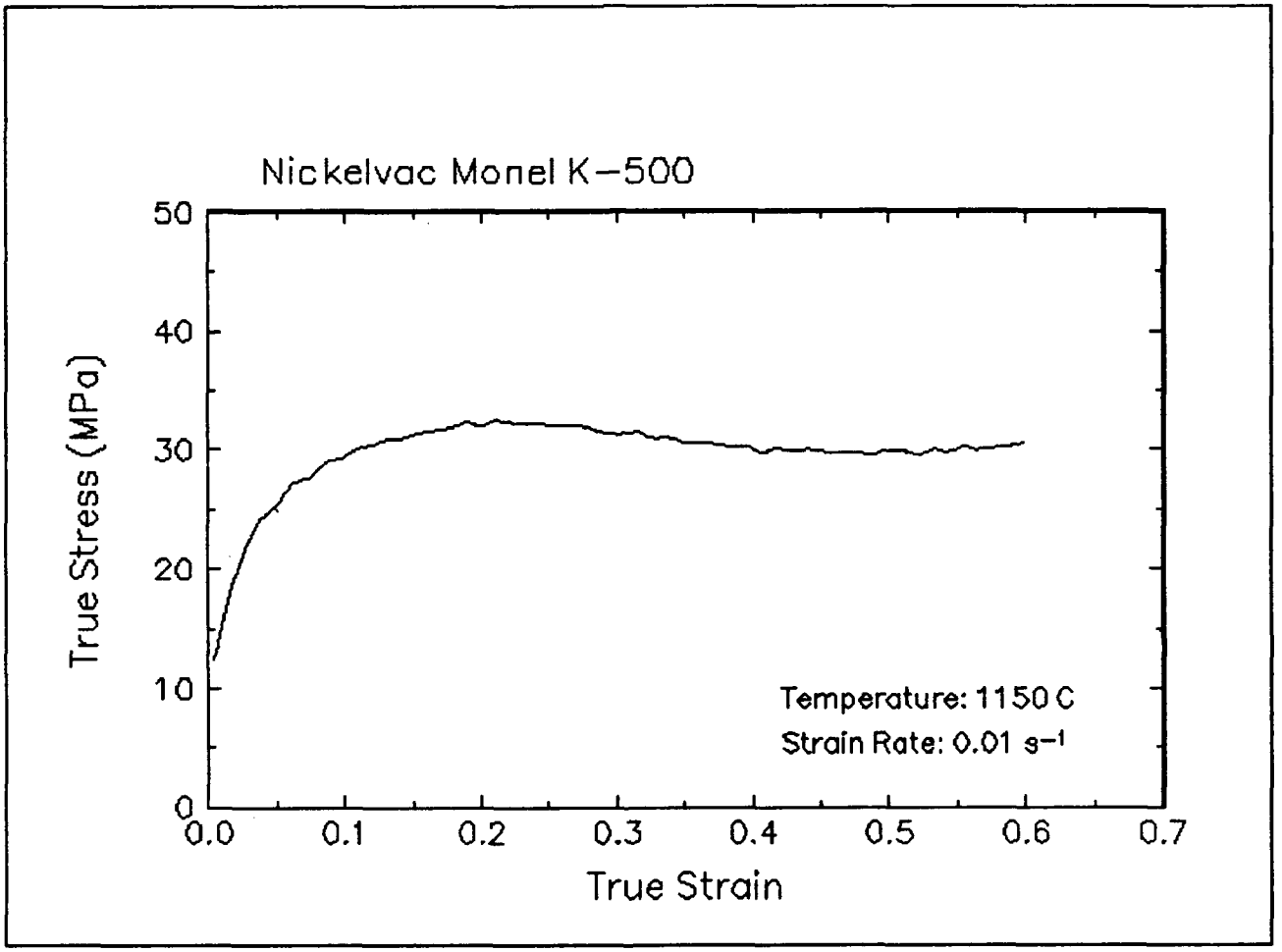

Figure 51. True stress-true strain curve, 1150 C and 0.01 s^{-1}.

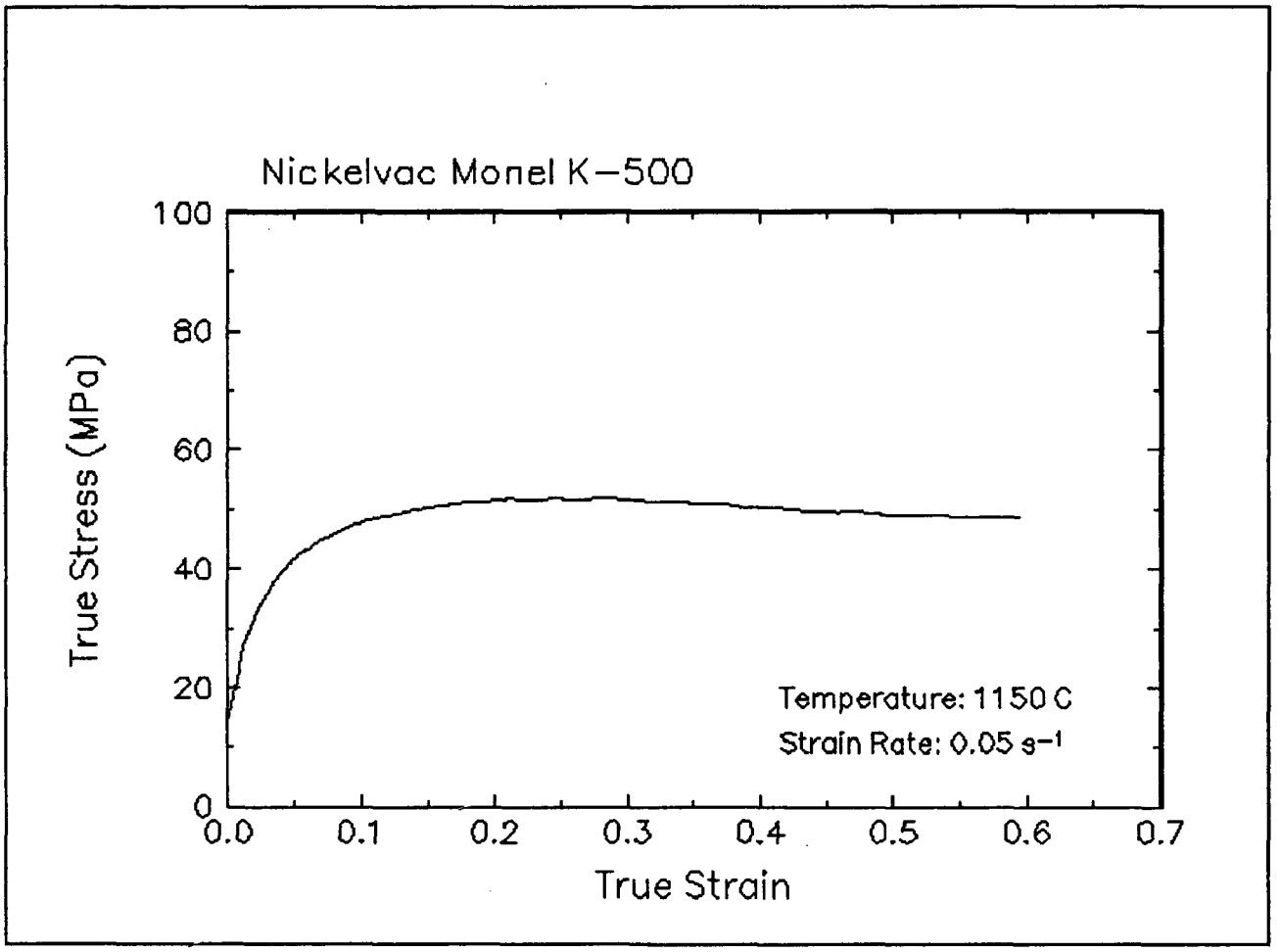

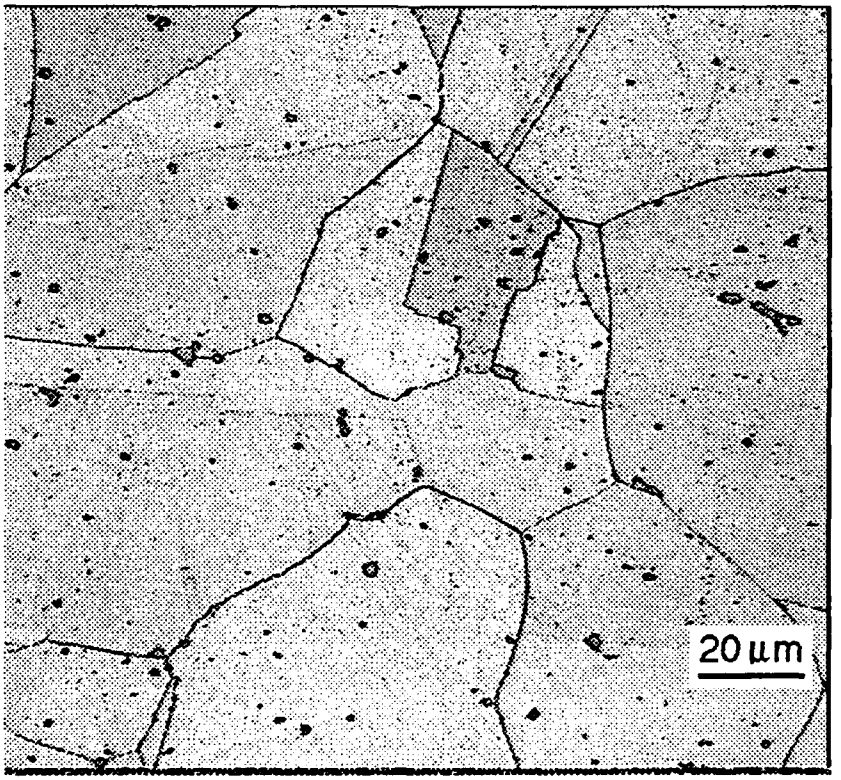

Figure 52. True stress-true strain curve and an optical micrograph from the center of the compressed sample cut through the compression axis, 1150 C and 0.05 s^{-1}.

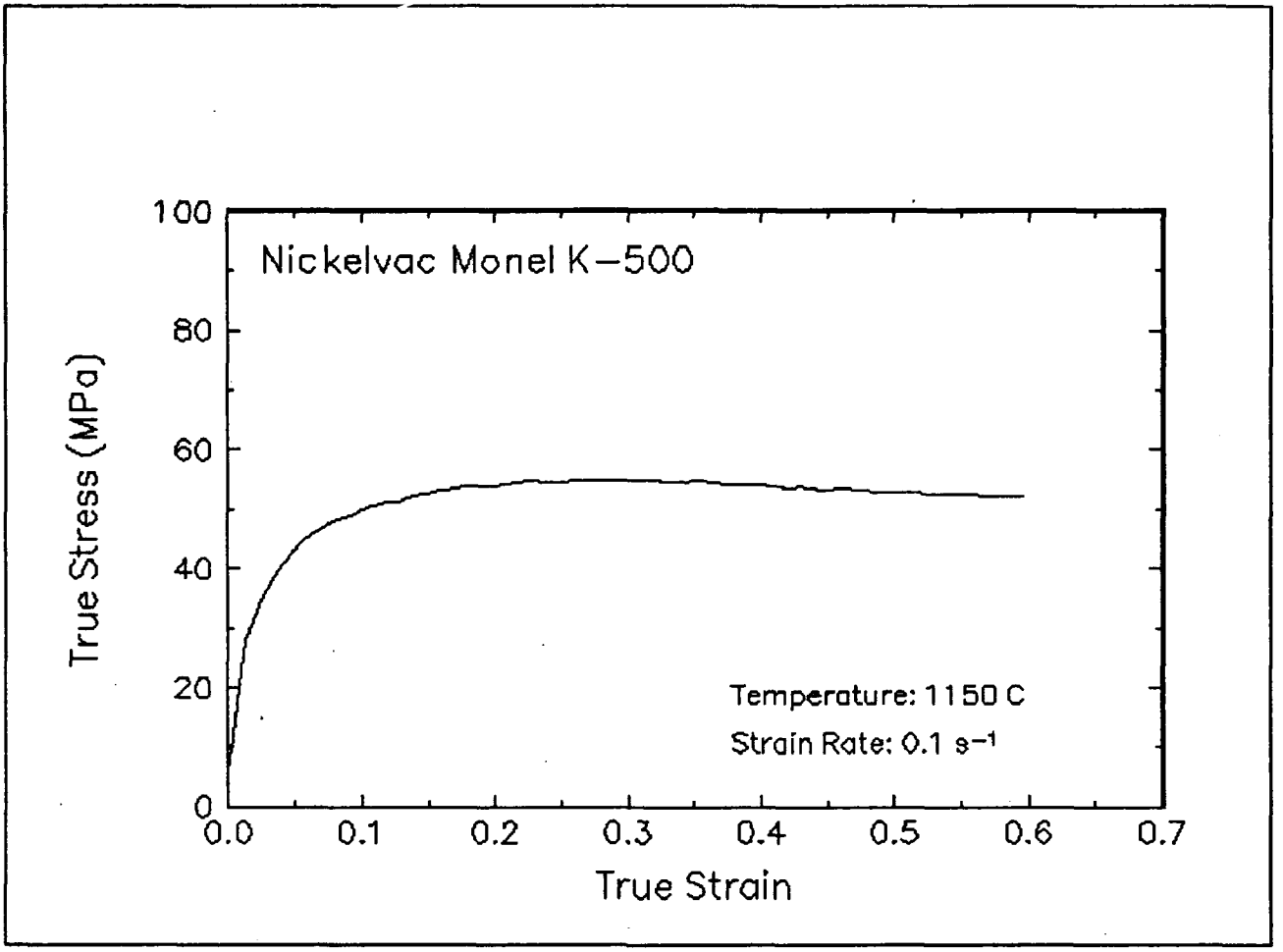

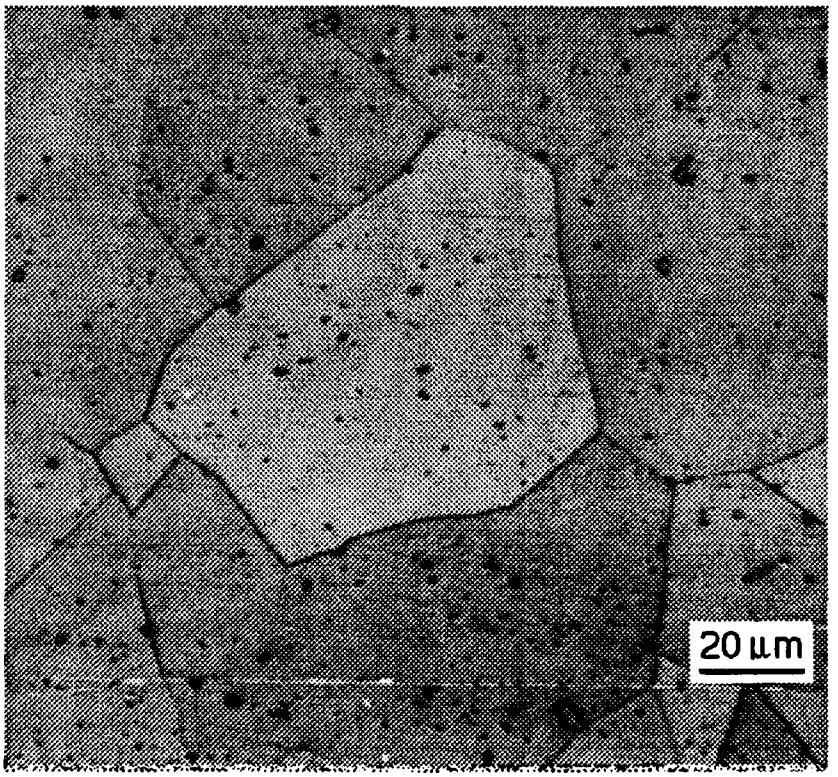

Figure 53. True stress-true strain curve and an optical micrograph from the center of the compressed sample cut through the compression axis, 1150 C and 0.1 s^{-1}.

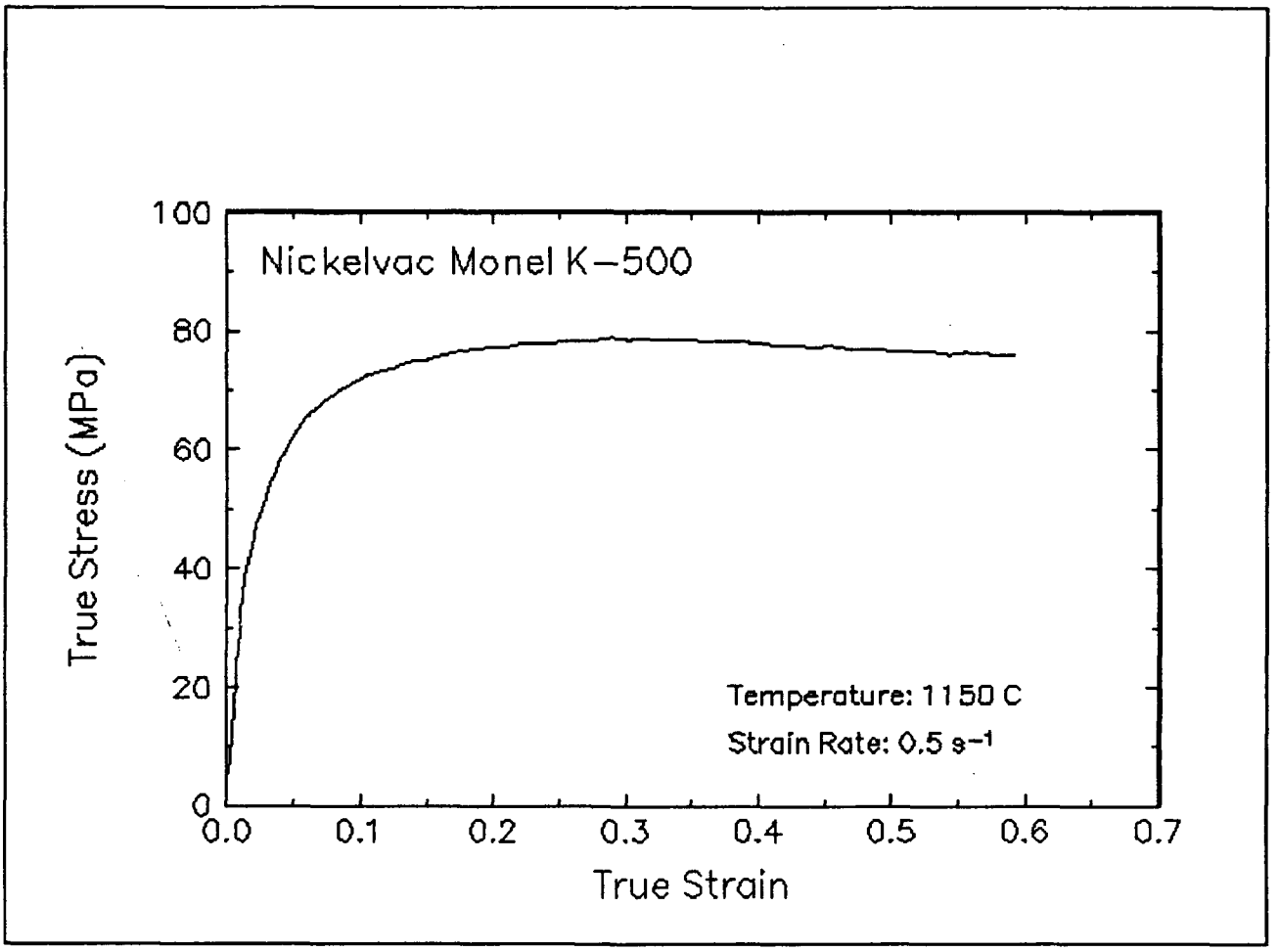

Figure 54. True stress-true strain curve and an optical micrograph from the center of the compressed sample cut through the compression axis, 1150 C and 0.5 s^{-1}.

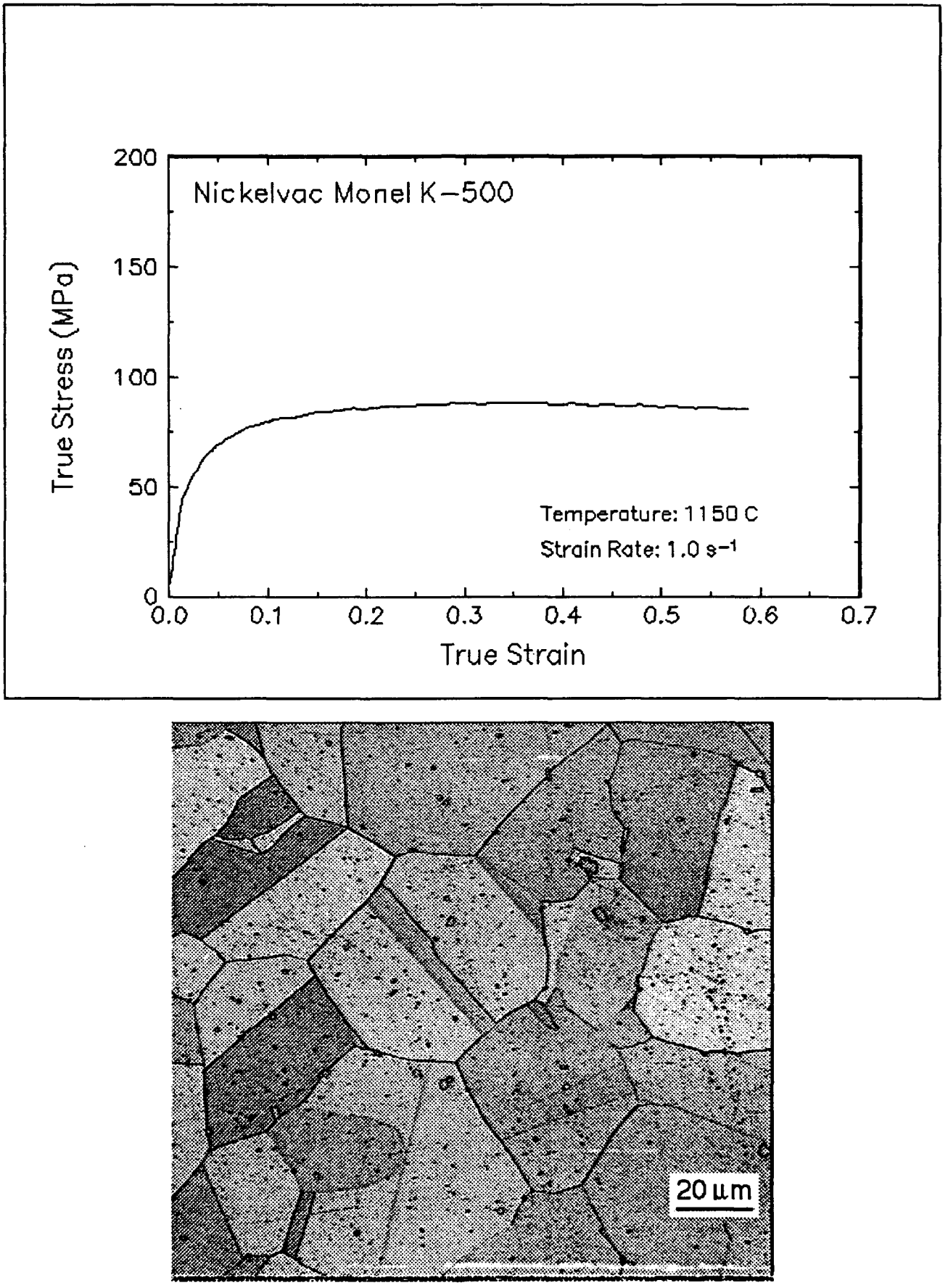

Figure 55. True stress-true strain curve and an optical micrograph from the center of the compressed sample cut through the compression axis, 1150 C and 1 s^{-1}.

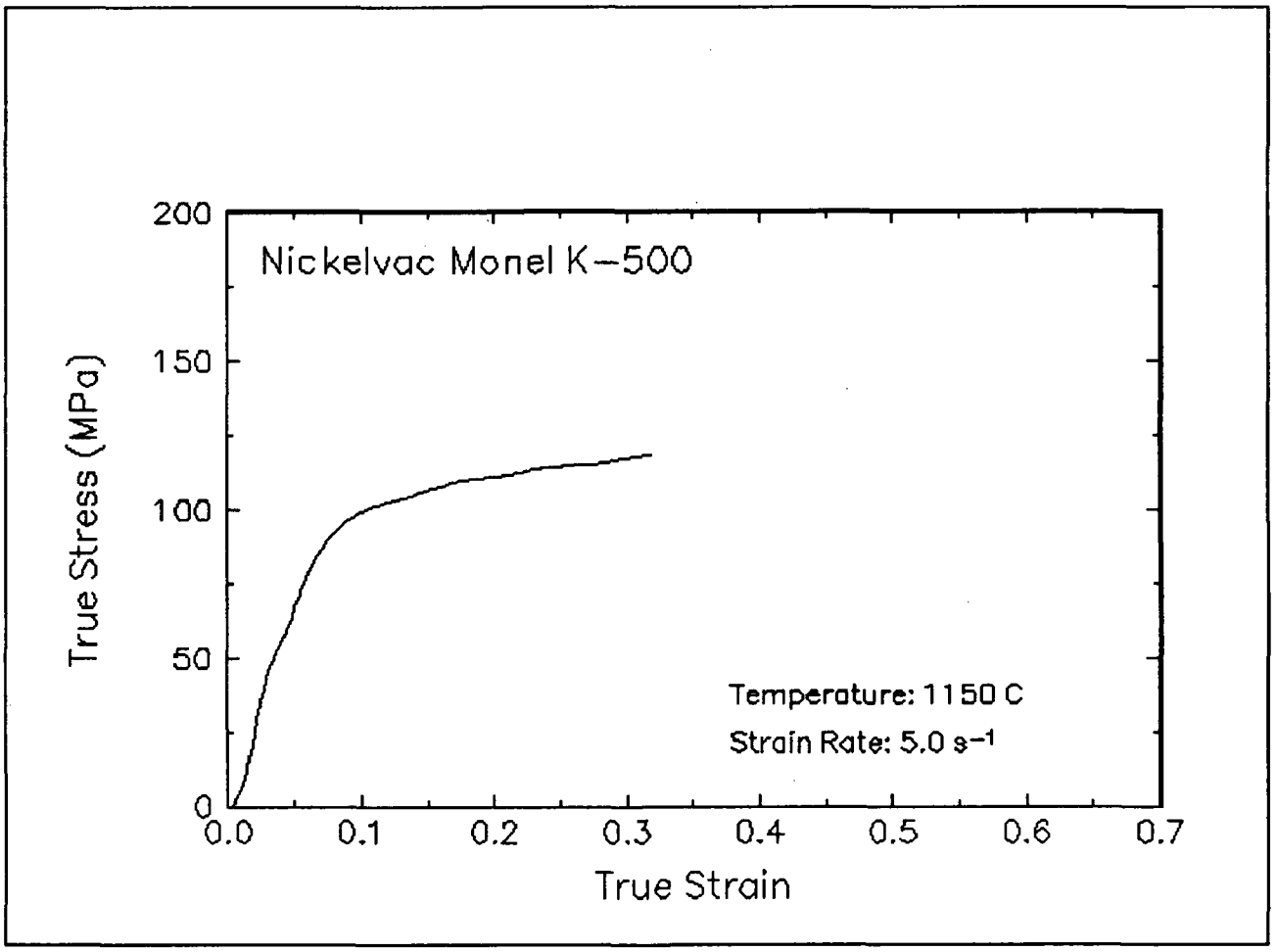

Figure 56. True stress-true strain curve, 1150 C and 5 s^{-1}.

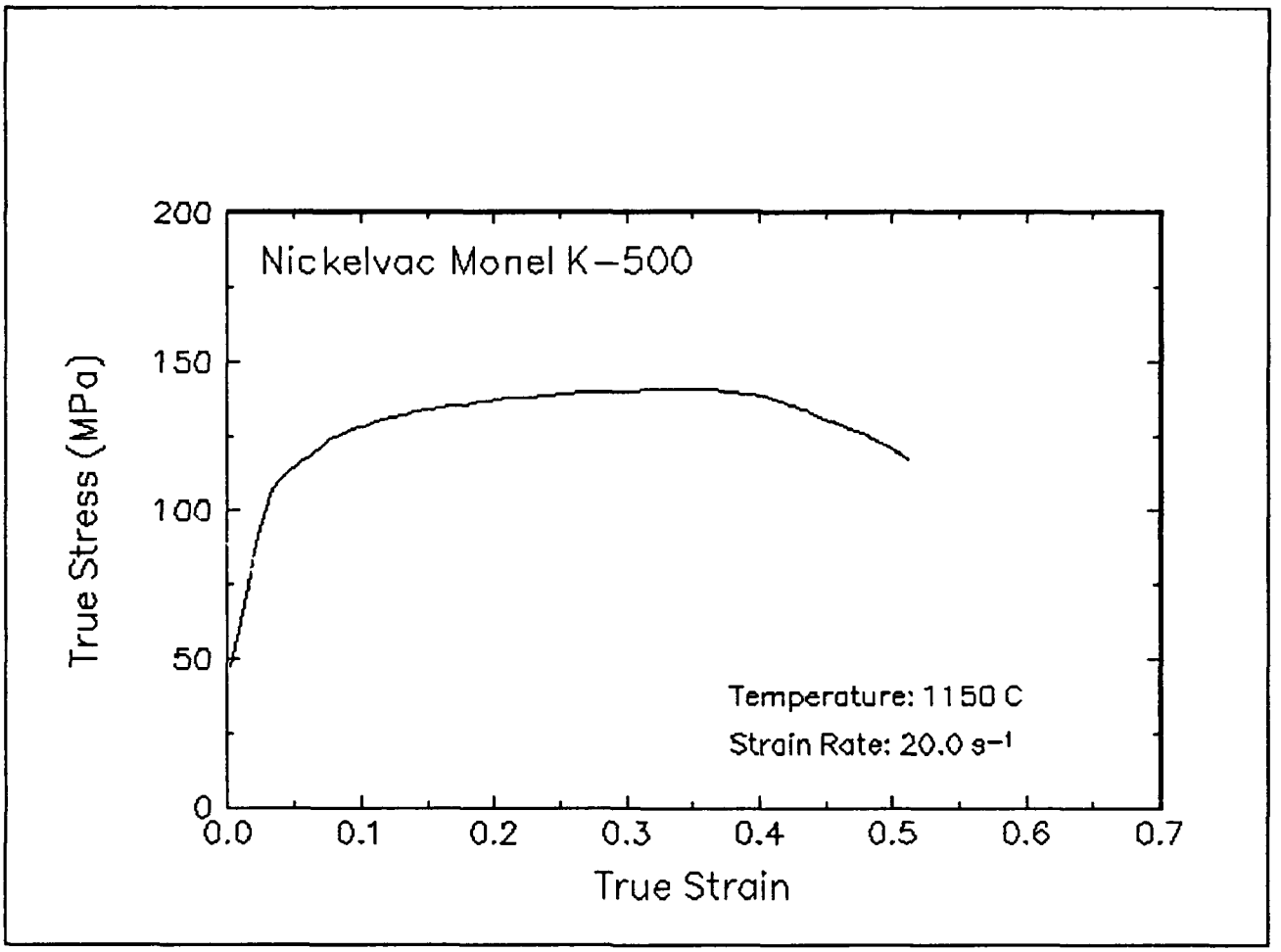

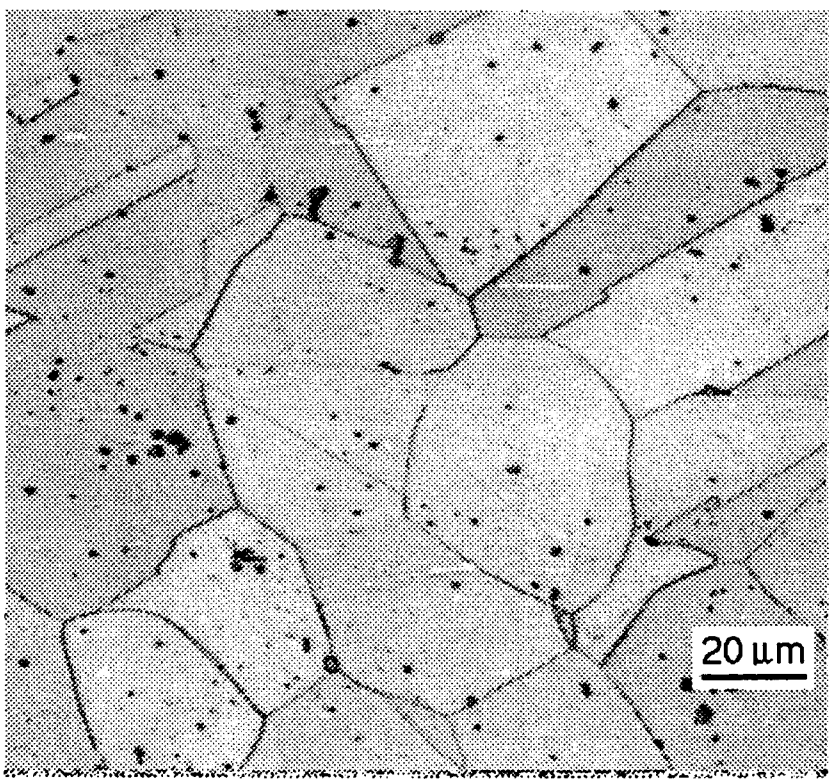

Figure 57. True stress-true strain curve and an optical micrograph from the center of the compressed sample cut through the compression axis, 1150 C and 20 s^{-1}.

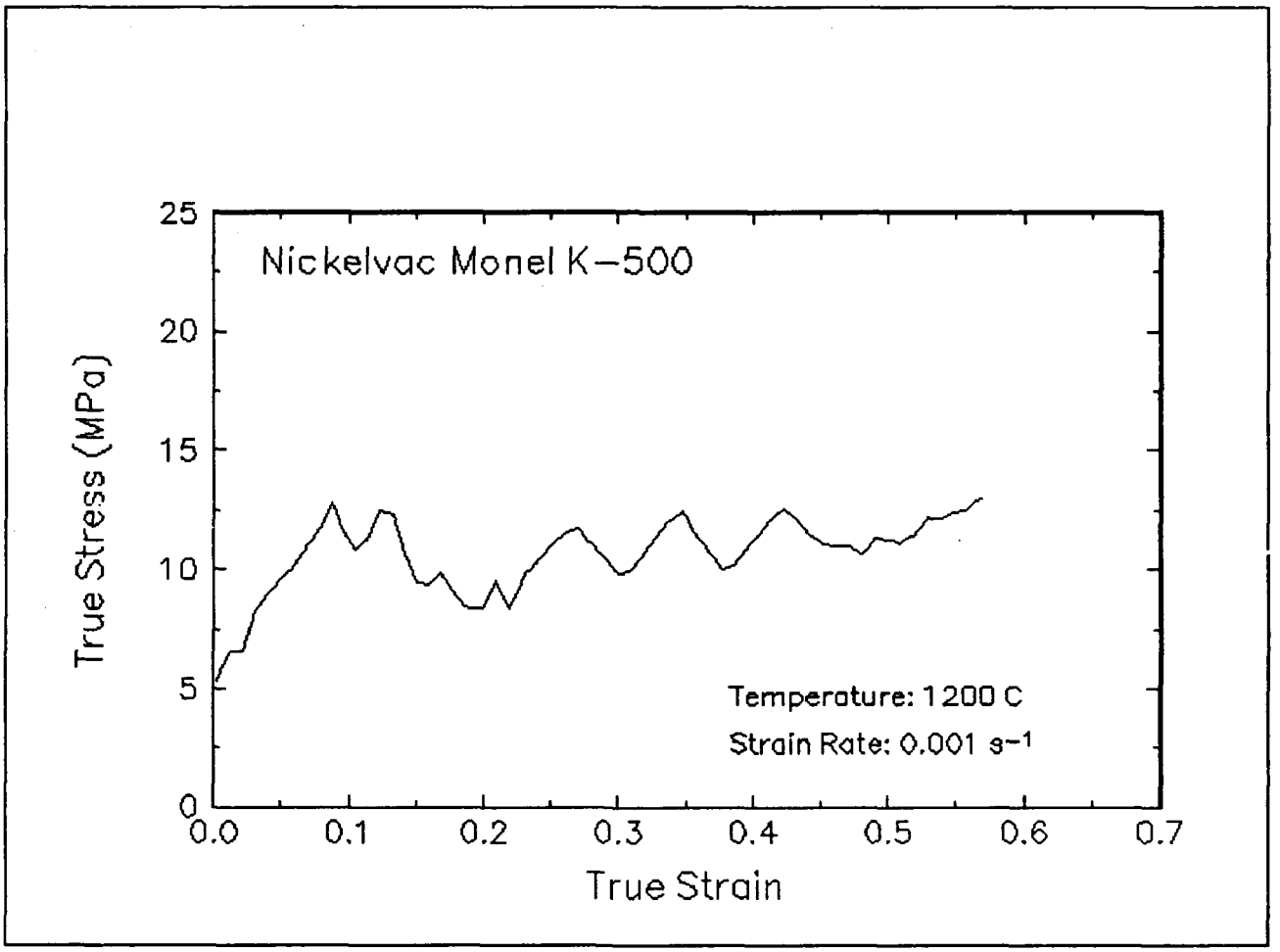

Figure 58. True stress-true strain curve, 1200 C and 0.001 s^{-1}.

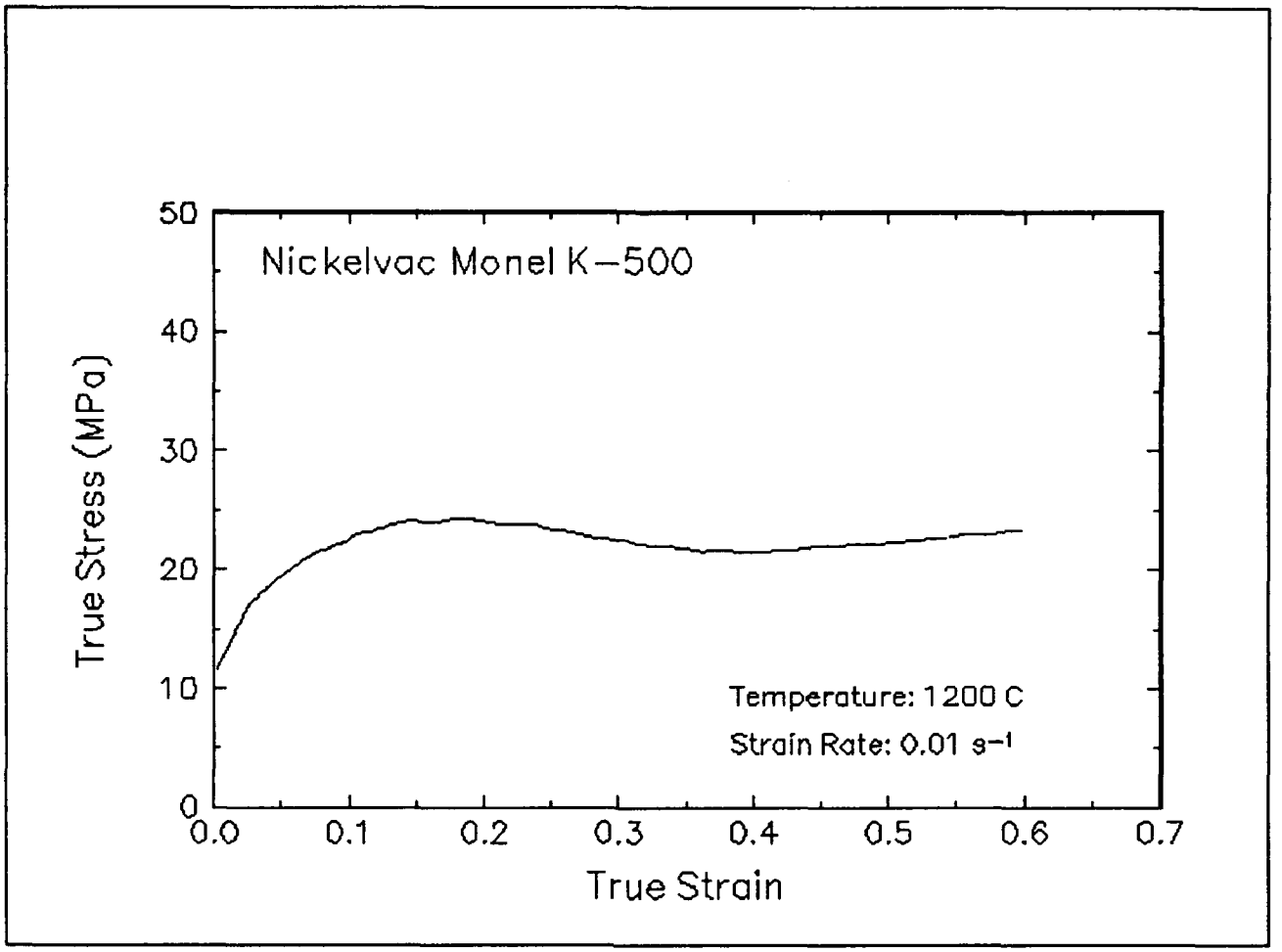

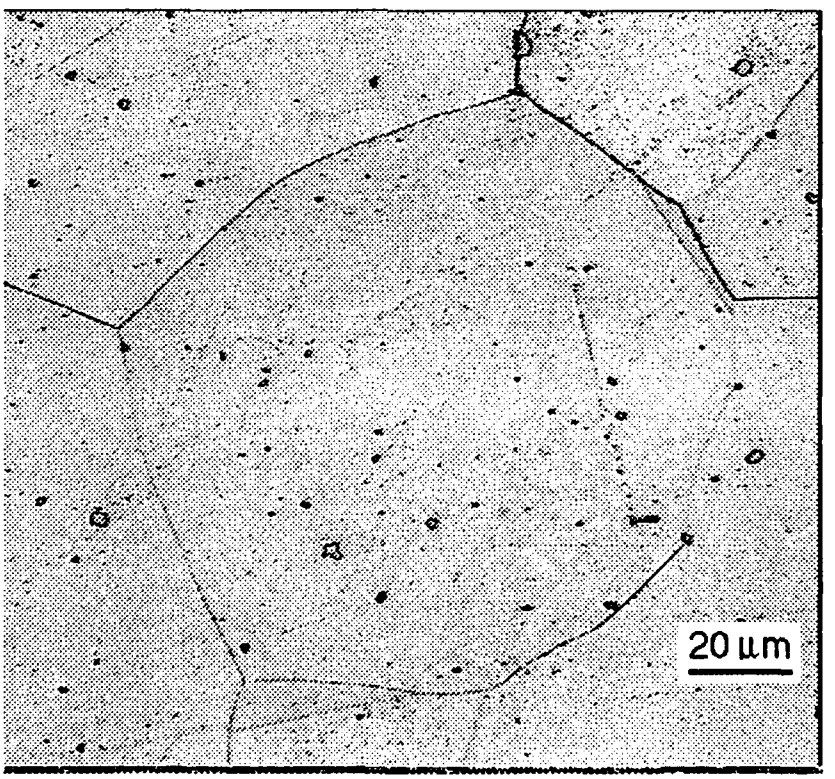

Figure 59 True stress-true strain curve and an optical micrograph from the center of the compressed sample cut through the compression axis, 1200 C and 0.01 s^{-1}.

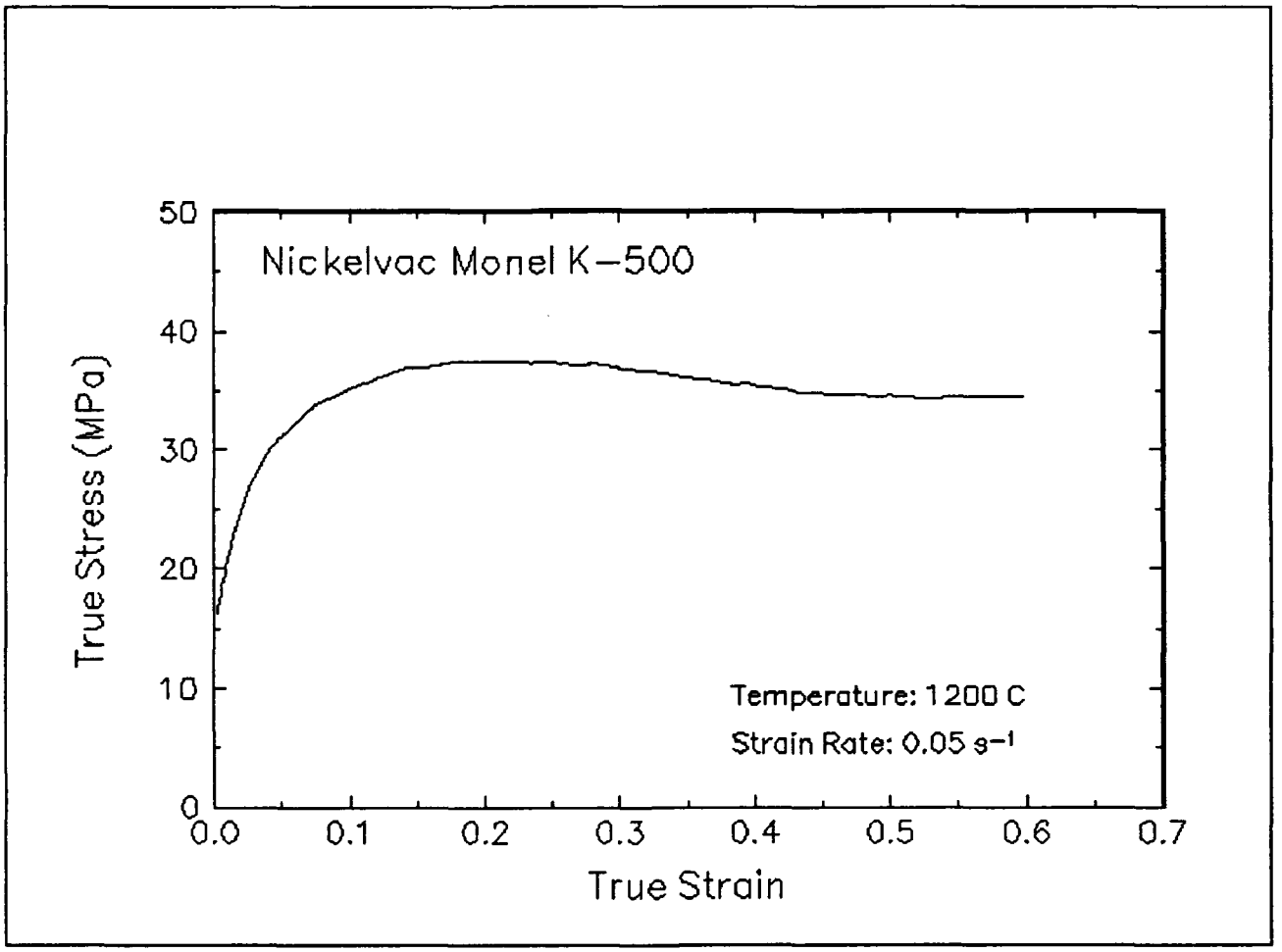

Figure 60. True stress-true strain curve, 1200 C and 0.05 s^{-1}.

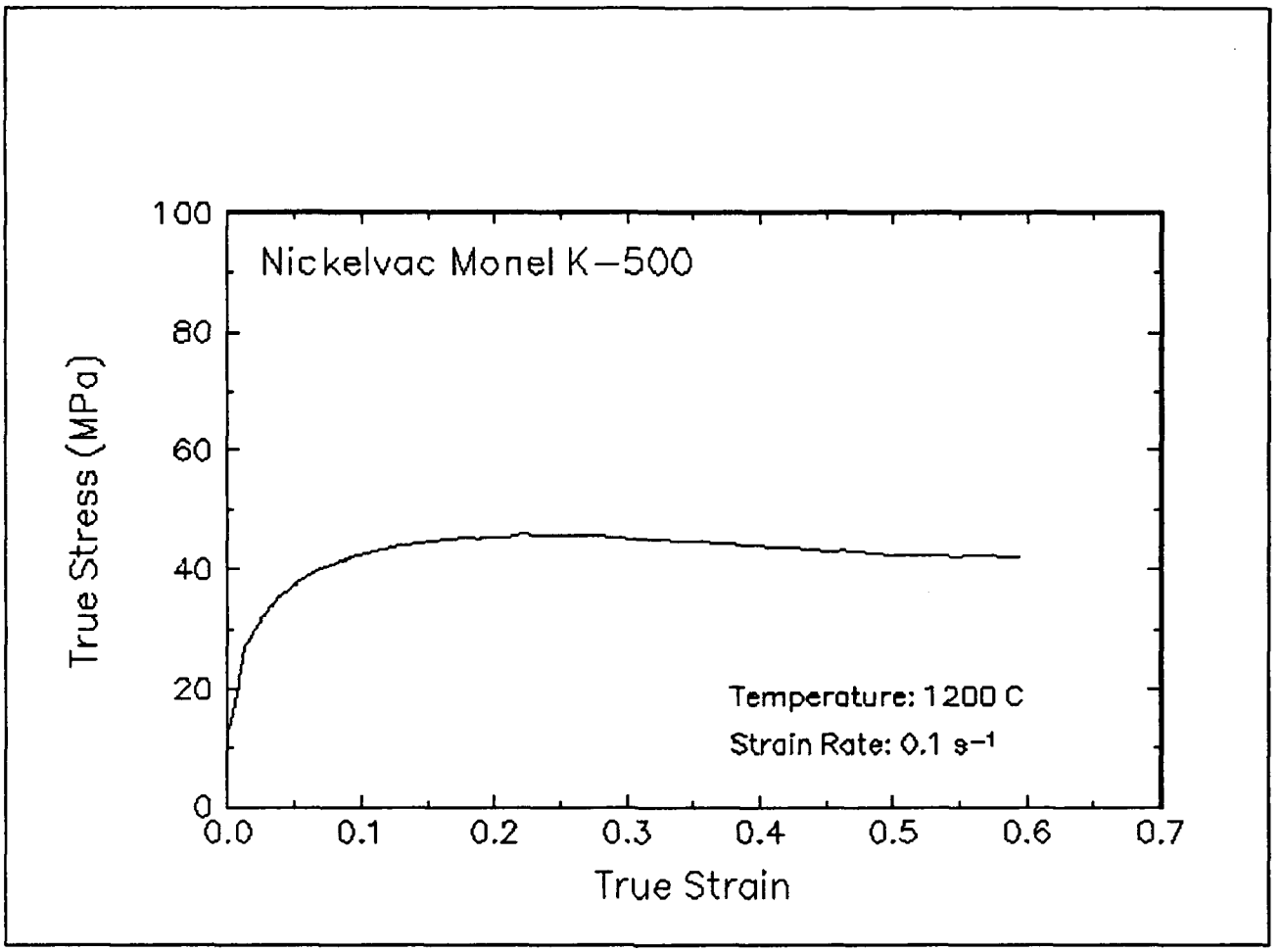

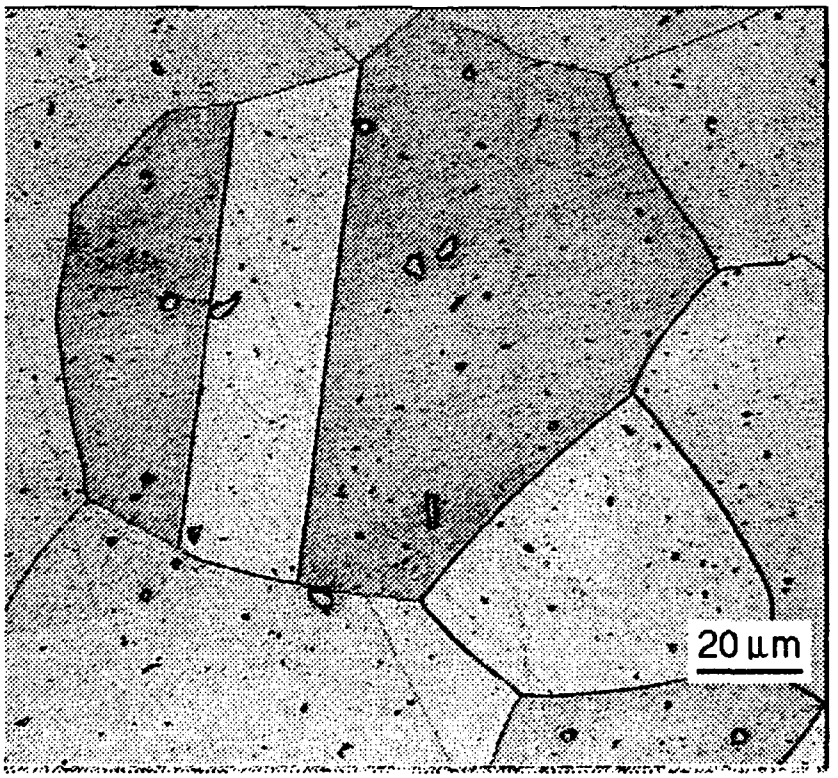

Figure 61. True stress-true strain curve and an optical micrograph from the center of the compressed sample cut through the compression axis, 1200 C and 0.1 s^{-1}.

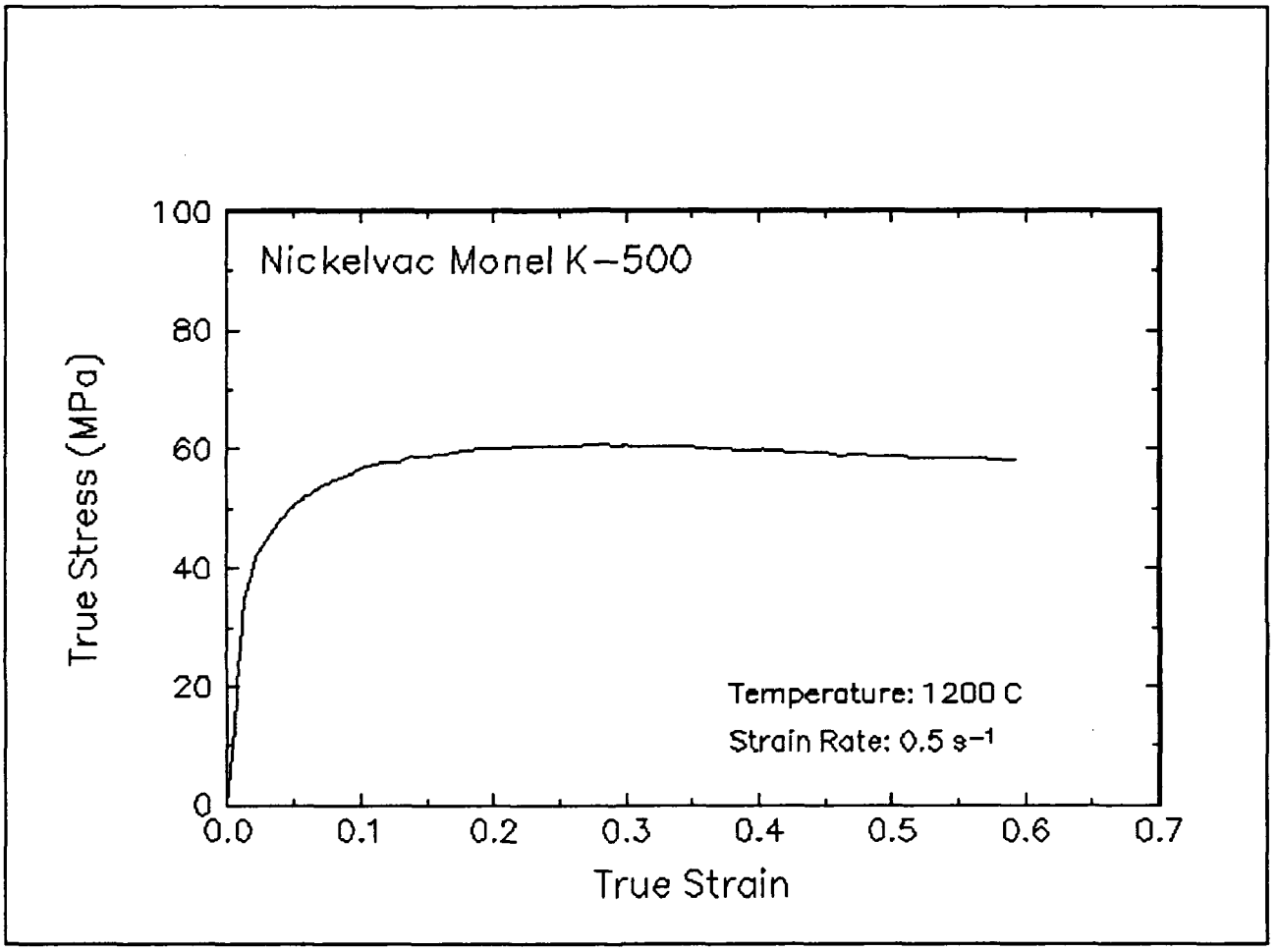

Figure 62. True stress-true strain curve, 1200 C and 0.5 s^{-1}.

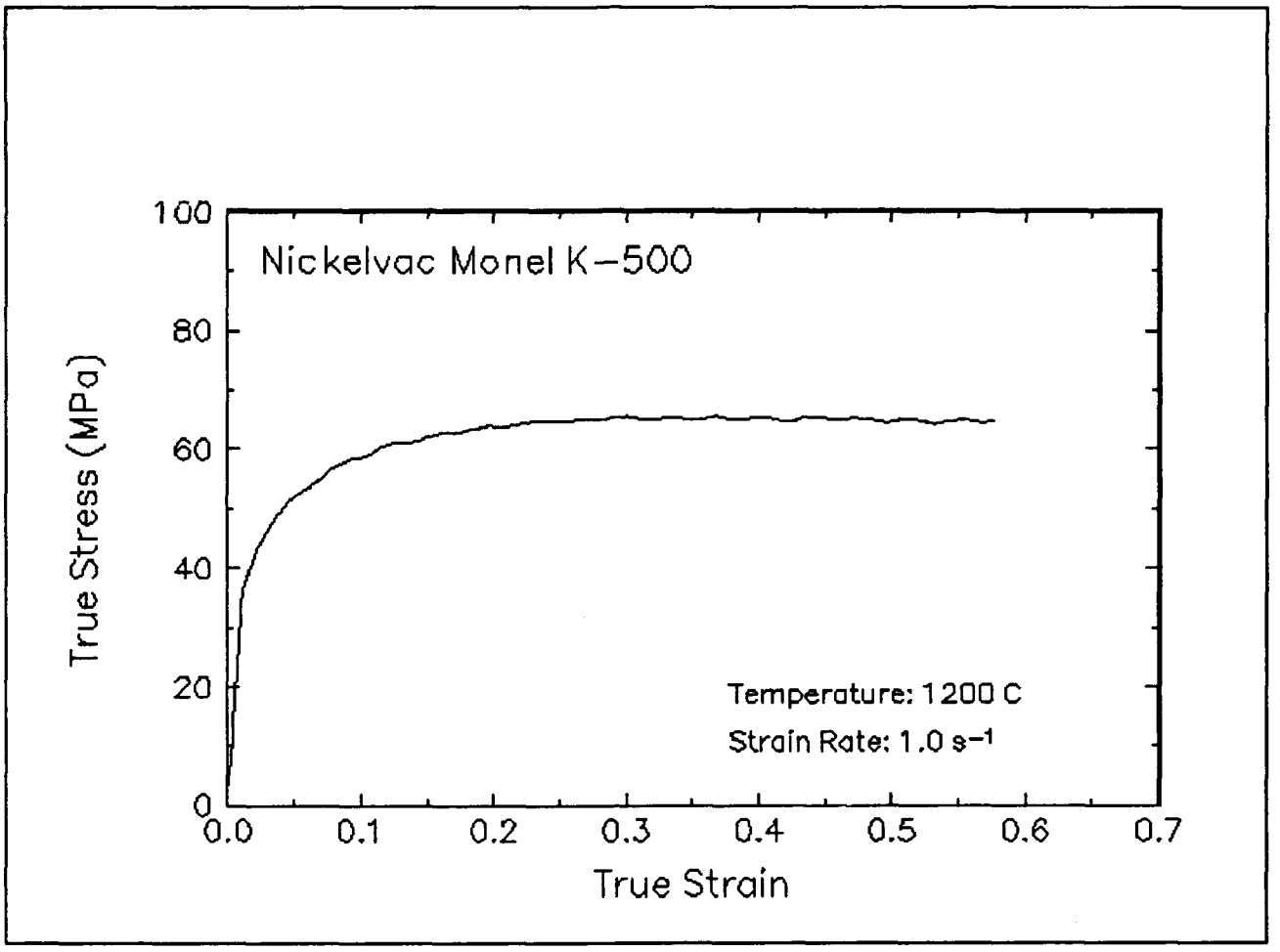

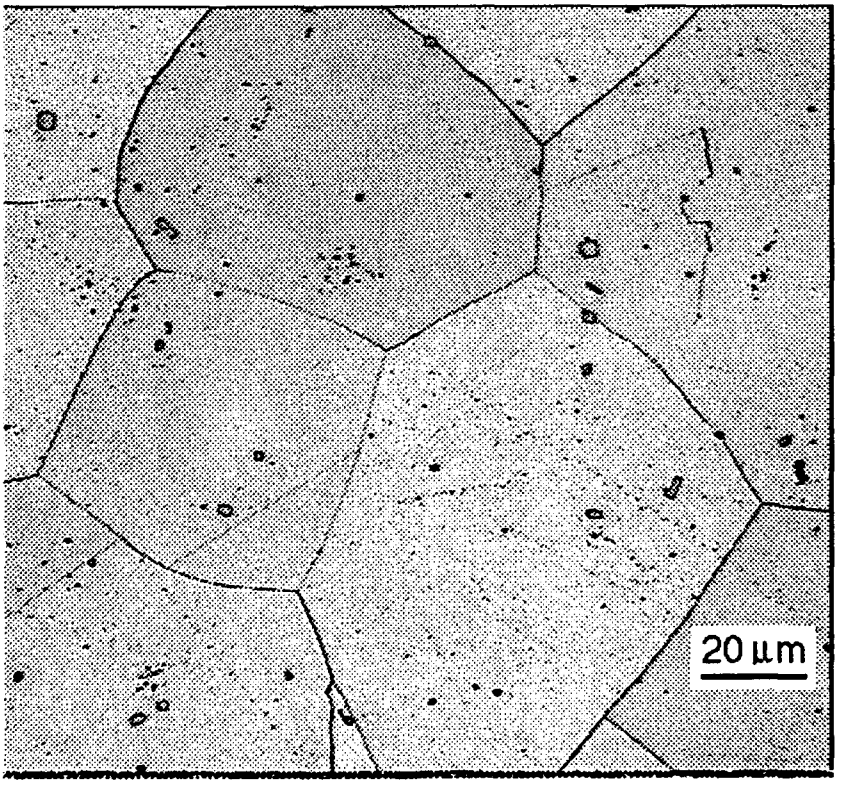

Figure 63. True stress-true strain curve and an optical micrograph from the center of the compressed sample cut through the compression axis, 1200 C and 1 s^{-1}.

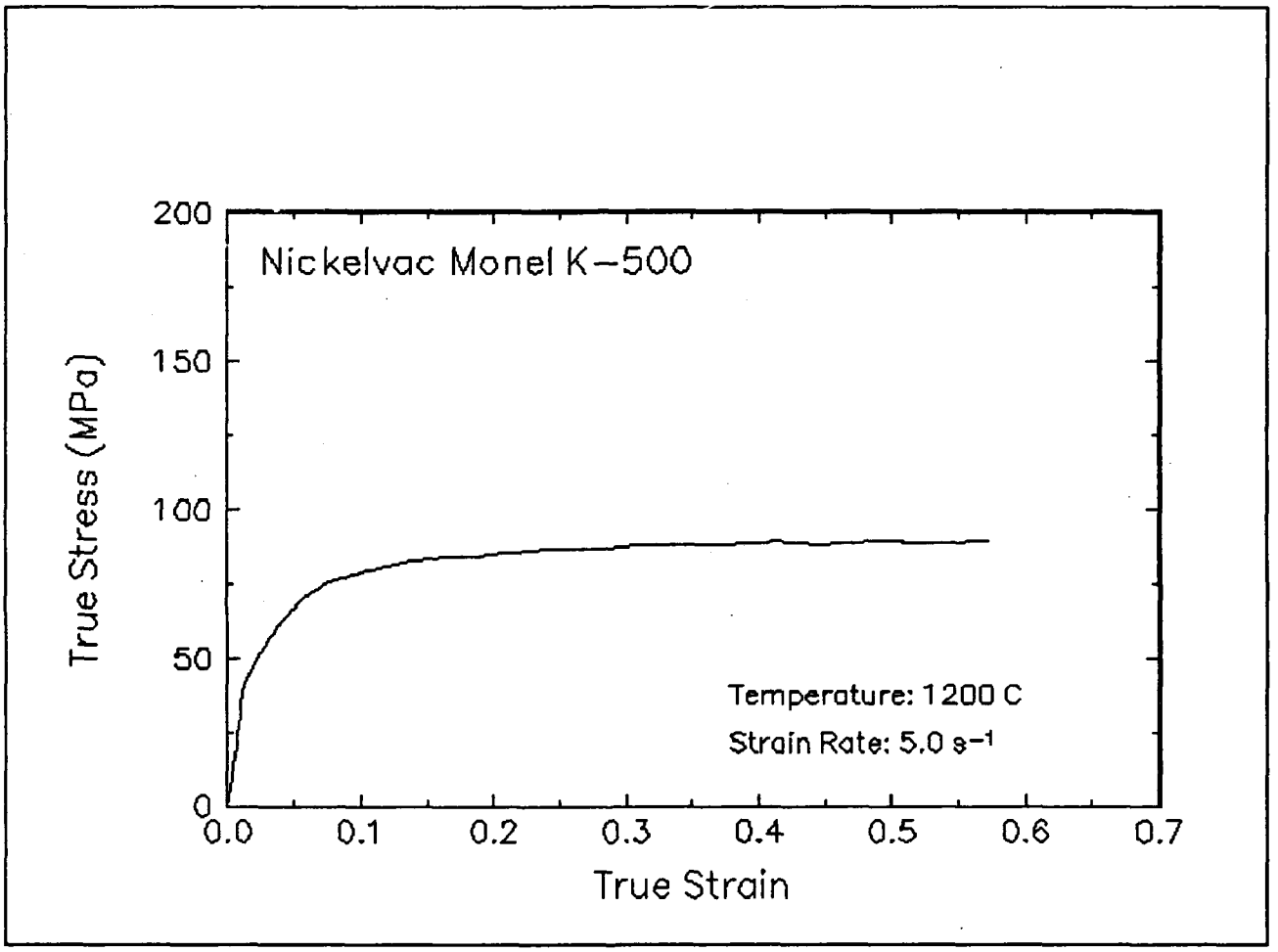

Figure 64. True stress-true strain curve, 1200 C and 5 s^{-1}.

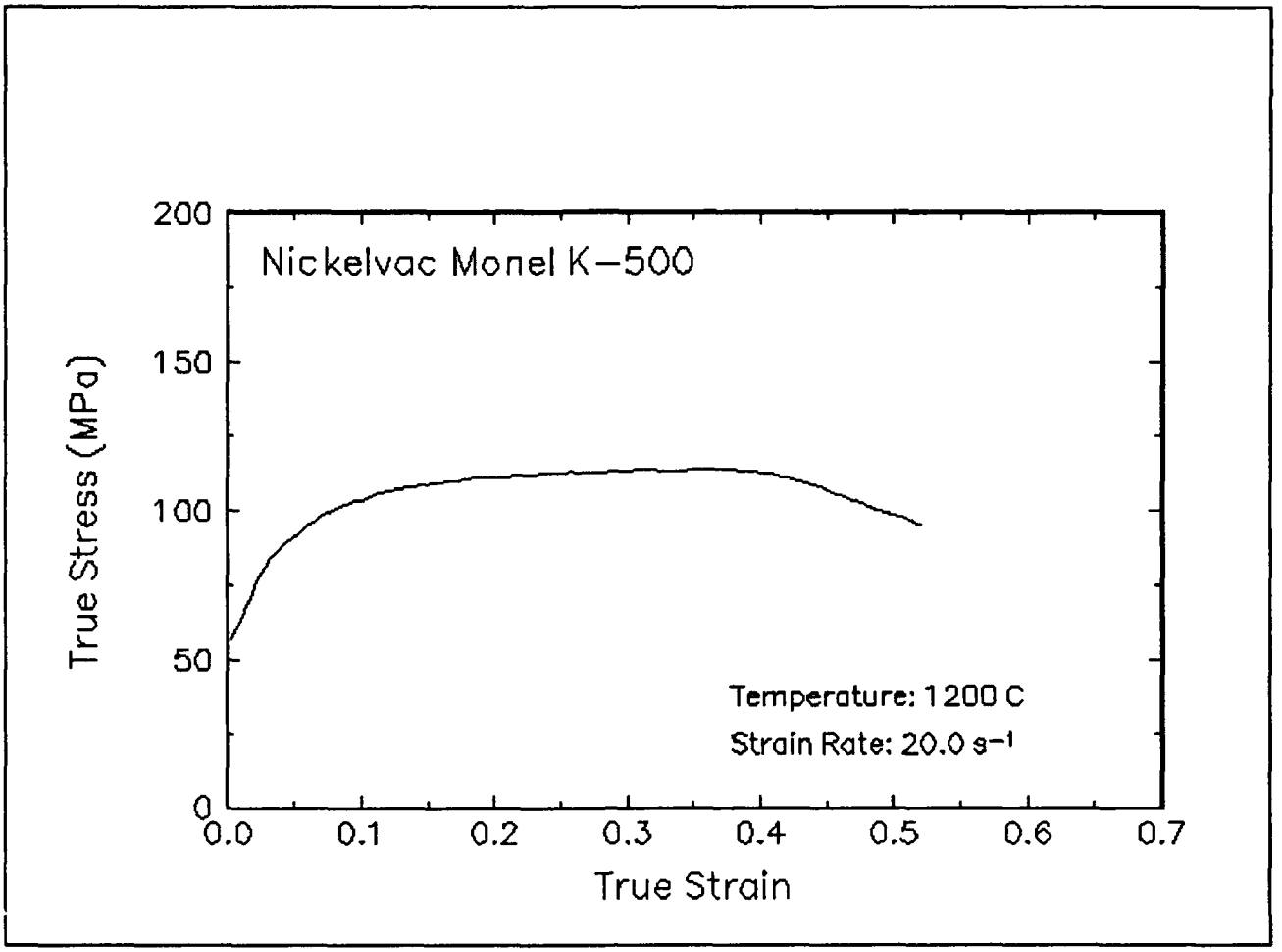

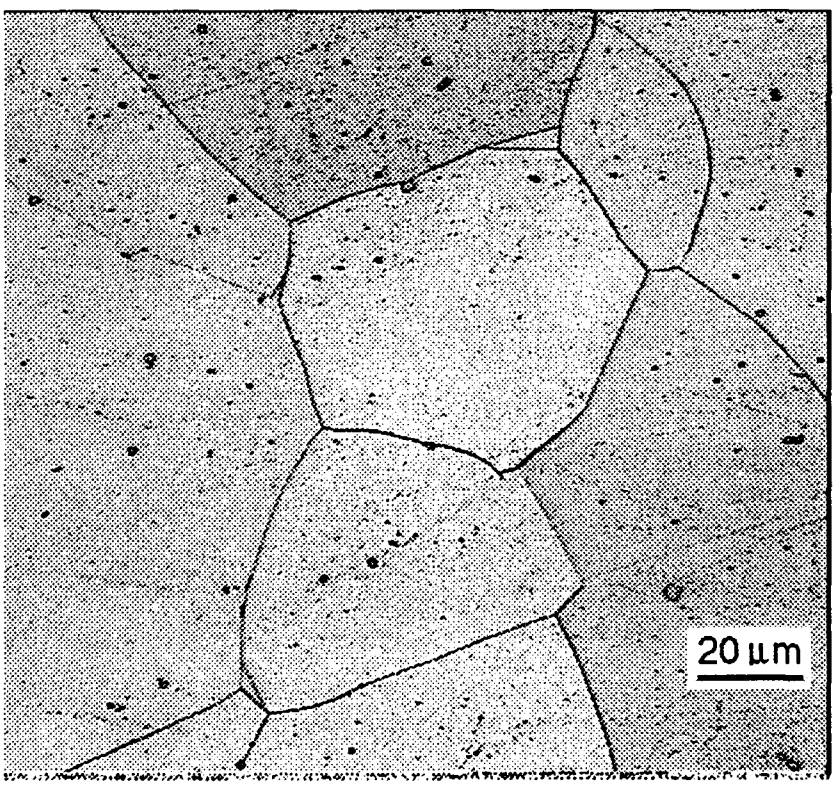

Figure 65. True stress-true strain curve and an optical micrograph from the center of the compressed sample cut through the compression axis, 1200 C and 20 s^{-1}.

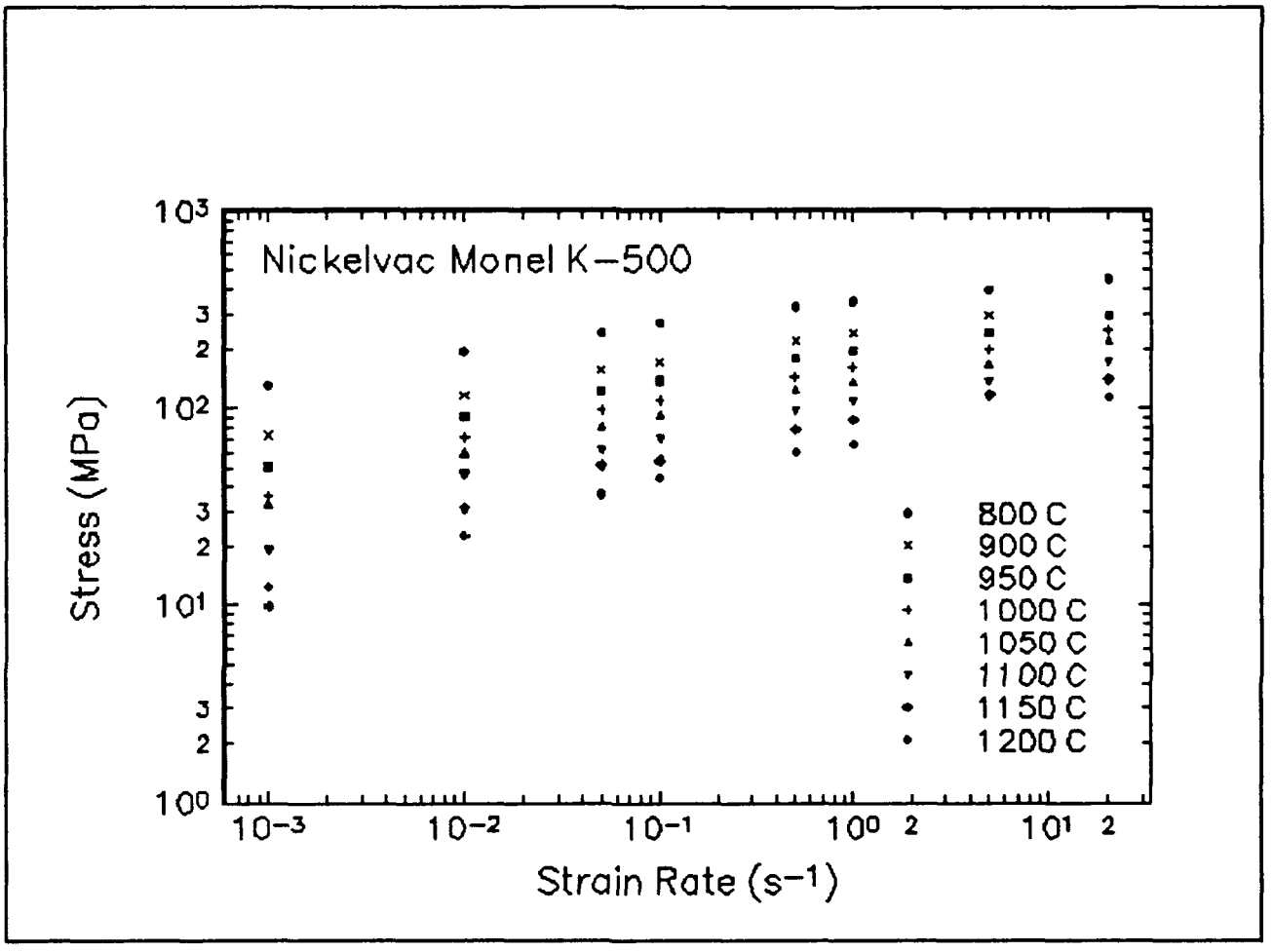

Figure 66. Effect of strain rate on stress in log-log scale at a true strain of 0.3 for Nickelvac K-500.

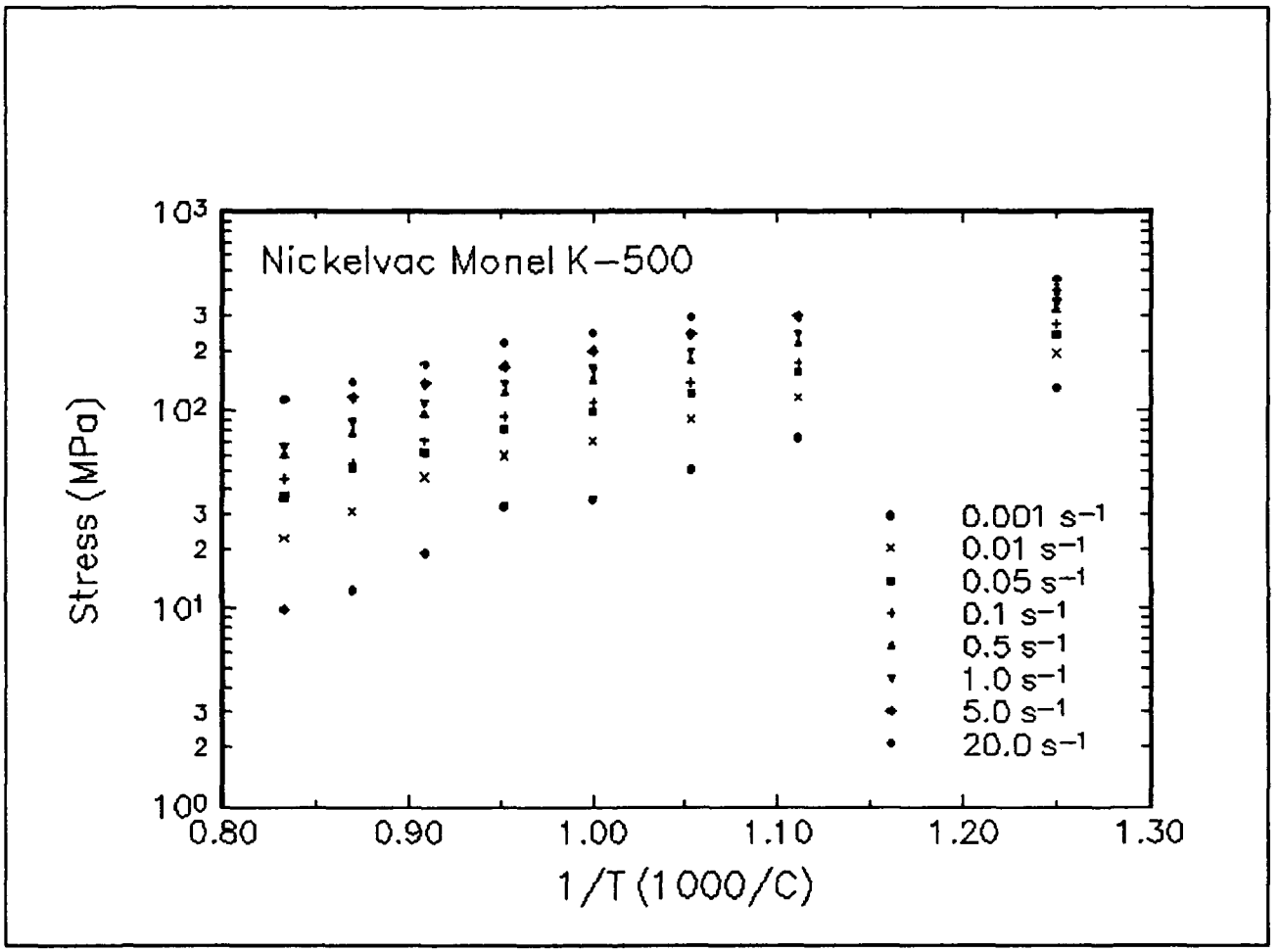

Figure 67. Effect of temperature on stress at a true strain of 0.3 for Nickelvac K-500.

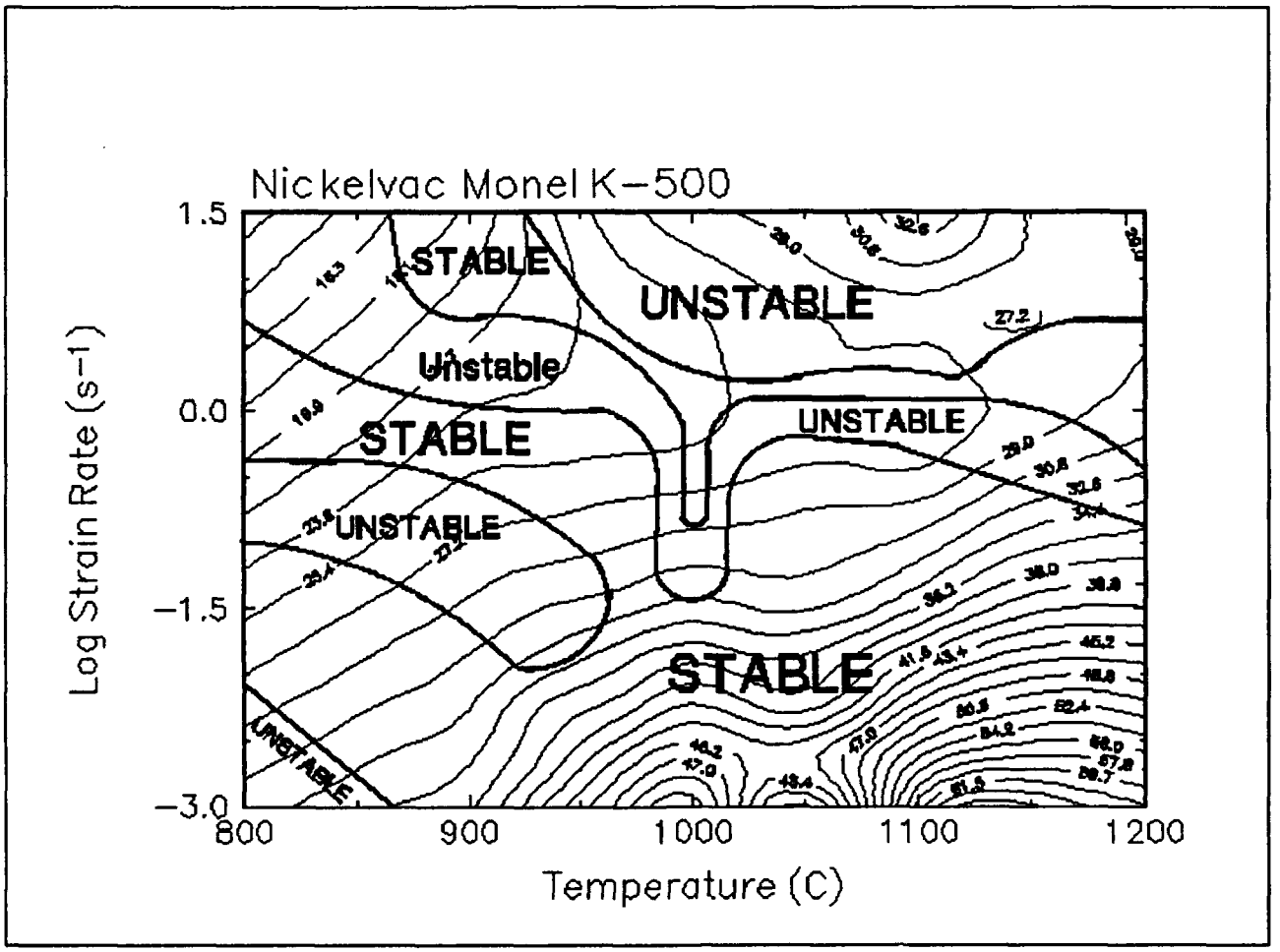

Figure 68. Processing map of Nickelvac K-500 at a true strain of 0.3.

Summary

Compression tests have been performed on Nickelvac K-500 over a wide range of temperatures and strain rates. The experimental conditions used in this work are representative of those used in metalforming practices. From the stress-strain curves, the flow behavior was characterized and a processing map indicating the optimum processing condition was generated. This condition is approximately 1125 C and 10^{-3} s^{-1}.

The deformed microstructures were characterized from the quenched specimens by optical microscopy and are presented for selective testing conditions together with the stress-strain curves.

Implementation of Data Provided by the Atlas of Formability

The Atlas of Formability program provides ample data on flow behavior of various important engineering materials in the temperature and strain rate regime commonly used in metalworking processes. The data are valuable in design and problem solving in metalworking processes of advanced materials. Microstructural changes with temperature and strain rates are also provided in the Bulletin, which helps the design engineer to select processing parameters leading to the desired microstructure.

The data can also be used to construct processing map using dynamic material modeling approach to determine stable and unstable regions in terms of temperature and strain rate. The temperature and strain rate combination at the highest efficiency in the stable region provides the optimum processing condition. This has been demonstrated in this Bulletin. In some metalworking processes such as forging, strain rate varies within the workpiece. An analysis of the process with finite element method (FEM) can ensure that the strain rates at the processing temperature in the whole workpiece fall into the stable regions in the processing map. Furthermore, FEM analysis with the data from the Atlas of Formability can be coupled with fracture criteria to predict defect formation in metalworking processes.

Using the data provided by the Atlas of Formability, design of metalworking processes, dynamic material modeling, FEM analysis of metalworking processes, and defect prediction are common practice in *Concurrent Technologies Corporation*. Needs in solving problems related to metalworking processes can be directed to Dr. Prabir K. Chaudhury, Manager of Forming Department, by calling (814) 269-2594.